

The *Gaia*-ESO Survey[★]: double, triple and quadruple-line spectroscopic binary candidates

T. Merle¹, S. Van Eck¹, A. Jorissen¹, M. Van der Swaelmen¹, T. Masseron², T. Zwitter³, D. Hatzidimitriou^{4,5}, A. Klutsch⁶, D. Pourbaix¹, R. Blomme⁷, C. C. Worley², G. Sacco⁸, J. Lewis², C. Abia⁹, G. Travençolo³, R. Sordo¹⁰, A. Bragaglia¹¹, R. Smiljanic¹², E. Pancino^{8,21}, F. Damiani¹³, A. Hourihane², G. Gilmore², S. Randich⁸, S. Koposov², A. Casey², L. Morbidelli⁸, E. Franciosini⁸, L. Magrini⁸, P. Jofre^{2,22}, M. T. Costado¹⁴, R. D. Jeffries¹⁵, M. Bergemann¹⁶, A. C. Lanzafame^{6,17}, A. Bayo¹⁸, G. Carraro¹⁹, E. Flaccomio¹³, L. Monaco²⁰, and S. Zaggia¹⁰

¹ Institut d'Astronomie et d'Astrophysique, Université Libre de Bruxelles, CP. 226, Boulevard du Triomphe, 1050 Brussels, Belgium
e-mail: tmerle@ulb.ac.be

² Institute of Astronomy, University of Cambridge, Madingley Road, Cambridge CB3 0HA, UK

³ Faculty of Mathematics and Physics, University of Ljubljana, Jadranska 19, 1000, Ljubljana, Slovenia

⁴ Department of Astrophysics, Faculty of Physics, National and Kapodistrian University of Athens, Panepistimiopolis, GR15784 Zografos, Athens, Greece

⁵ IAASARS, National Observatory of Athens, 15236 Penteli, Greece

⁶ INAF – Osservatorio Astrofisico di Catania, via S. Sofia 78, 95123 Catania, Italy

⁷ Royal Observatory of Belgium, Ringlaan 3, 1180, Brussels, Belgium

⁸ INAF – Osservatorio Astrofisico di Arcetri, Largo E. Fermi 5, 50125 Firenze, Italy

⁹ Dpto. Física Teórica y del Cosmos, Universidad de Granada, 18071, Granada, Spain

¹⁰ INAF – Osservatorio Astronomico di Padova, vicolo dell'Osservatorio 5, 35122 Padova, Italy

¹¹ INAF – Osservatorio Astronomico di Bologna, via Ranzani 1, 40127, Bologna, Italy

¹² Nicolaus Copernicus Astronomical Center, Polish Academy of Sciences, ul. Bartycka 18, 00-716, Warsaw, Poland

¹³ INAF – Osservatorio Astronomico di Palermo, Piazza del Parlamento 1, 90134, Palermo, Italy

¹⁴ Instituto de Astrofísica de Andalucía-CSIC, Apdo. 3004, 18080 Granada, Spain

¹⁵ Astrophysics Group, Keele University, Keele, Staffordshire ST5 5BG, United Kingdom

¹⁶ Max-Planck Institute for Astronomy, Königstuhl 17, Heidelberg, D-69117, Germany

¹⁷ Università di Catania, Dipartimento di Fisica e Astronomia, Sezione Astrofisica, Via S. Sofia 78, I-95123 Catania, Italy

¹⁸ Instituto de Física y Astronomía, Universidad de Valparaíso, Chile

¹⁹ European Southern Observatory, Alonso de Cordova 3107 Vitacura, Santiago de Chile, Chile

²⁰ Departamento de Ciencias Físicas, Universidad Andres Bello, Republica 220, Santiago, Chile

²¹ ASI Science Data Center, Via del Politecnico SNC, 00133 Roma, Italy ²² Núcleo de Astronomía, Facultad de Ingeniería, Universidad Diego Portales, Av. Ejército 441, Santiago, Chile

Received ...; accepted ...

ABSTRACT

Context. The *Gaia*-ESO Survey (GES) is a large spectroscopic survey that provides a unique opportunity to study the distribution of spectroscopic multiple systems among different populations of the Galaxy.

Aims. We aim at detecting binarity/multiplicity for stars targeted by the GES from the analysis of the cross-correlation functions (CCFs) of the GES spectra with spectral templates.

Methods. We develop a method based on the computation of the CCF successive derivatives to detect multiple peaks and determine their radial velocities, even when the peaks are strongly blended. The parameters of the detection of extrema (DOE) code have been optimized for each GES GIRAFFE and UVES setup to maximize detection. The DOE code therefore allows to automatically detect multiple line spectroscopic binaries (SB n , $n \geq 2$).

Results. We apply this method on the fourth GES internal data release and detect 354 SB n candidates (342 SB2, 11 SB3 and even one SB4), including only nine SBs known in the literature. This implies that about 98% of these SB n candidates are new (because of their faint visual magnitude that can reach $V = 19$). Visual inspection of the SB n candidate spectra reveals that the most probable candidates have indeed a composite spectrum. Among SB2 candidates, an orbital solution could be computed for two previously unknown binaries: CNAME 06404608+0949173 (known as V642 Mon) in NGC 2264 and CNAME 19013257-0027338 in Berkeley 81 (Be 81). A detailed analysis of the unique SB4 (four peaks in the CCF) reveals that CNAME 08414659-5303449 (HD 74438) in the open cluster IC 2391 is a physically bound stellar quadruple system. The SB candidates belonging to stellar clusters are reviewed in detail to discard false detections. We warn against the use of atmospheric parameters for these system components rather than by SB-specific pipelines.

Conclusions. Our implementation of an automatic detection of spectroscopic binaries within the GES has allowed an efficient discovery of many new multiple systems. With the detection of the SB1 candidates that will be the subject of a forthcoming paper, the study of the statistical and physical properties of the spectroscopic multiple systems will soon be possible for the entire GES sample.

Key words. binaries: spectroscopic - techniques: radial velocities - methods: data analysis - open clusters and associations: general - globular clusters: general

1. Introduction

Binary stars play a fundamental role in astrophysics since they allow direct measurements of masses, radii, and luminosities that put constraints on stellar physics, Galactic archaeology, high-energy physics, etc. Binary systems are found at all evolutionary stages, and after strong interaction, some may end up as double degenerate systems or merged compact objects.

Spectroscopic binaries (SBs) exist in different flavours. On the one hand, SB1 (SB with one observable spectrum) can only be detected from the Doppler shift of the stellar spectral lines. On the other hand, SB n ($n \geq 2$) are characterized by a composite spectrum made out of n stellar components, and are detected either from the composite nature of the spectrum or from the Doppler shift of the spectral lines. SBs are certainly the binaries that cover the widest range of masses (from brown dwarfs to massive twins) and all ranges of periods (from hours to hundreds of years as observed so far, *e.g.* Pourbaix 2000). To date, more than 3500 SBs with orbital elements have been catalogued and, among them, about 1126 are SB2 (Pourbaix et al. 2004, and the latest online version of the SB9 catalogue). The Geneva-Copenhagen Survey catalogue (Nordström et al. 2004; Holmberg et al. 2009) contains approximately 4000 SB1, 2100 SB2, and 60 SB3 out of 16700 F and G dwarf stars in the solar neighborhood, most without orbits. In the vast majority of cases, these binaries are not yet confirmed but correspond to an overall binary fraction in the Milky Way of almost 40 %. A census of binary fraction is also available from the Hipparcos catalogue (Frankowski et al. 2007) though the binary fraction per spectral type is probably biased due to selection biases in the Hipparcos entry catalogue. New recent Galactic surveys like APOGEE (Majewski et al. 2015) or LAMOST (Luo et al. 2015) allow new investigations of binarity over large sample of stars (see, *e.g.*, Gao et al. 2014; Troup et al. 2016; Fernandez et al. 2017). For instance, the RAVE survey has led to the detection of 123 SB2 candidates out of 26 000 objects (Matijević et al. 2010, 2011). We refer the reader to Duchêne & Kraus (2013) for a recent review of the physical properties of multiplicity among stars and more specifically to Raghavan et al. (2010) for a complete volume-limited sample of solar-type stars in the solar neighborhood (distances closer than 25 pc).

The *Gaia*-ESO Survey (GES) is an on-going ground-based high-resolution spectroscopic survey of 10^5 stellar sources (Gilmore et al. 2012; Randich et al. 2013) covering the main stellar populations (bulge, halo, thin and thick disks) of the Galaxy as well as a large number of open clusters spanning large metallicity and age ranges. All evolutionary stages are encountered within the GES, from pre-main sequence objects to red giants. It aims at complementing the spectroscopy of the *Gaia* ESA space mission (Wilkinson et al. 2005). The GES uses the FLAMES multi-fibre back end at the high resolution UVES ($R \sim 50\,000$) and moderate resolution GIRAFFE ($R \sim 20\,000$) spectrographs. The visual magnitude of the faintest targets reaches $V \sim 20$. The spectral coverage spans the optical wavelengths (from 4030 to

6950 Å) and the near infrared around the Ca II triplet and the Paschen lines (from 8490 to 8900 Å including the wavelength range of the Radial Velocity Spectrometer of the *Gaia* mission). The median signal-to-noise (S/N) ratio per pixel is similar for UVES and GIRAFFE single exposures (~ 30) whereas the most frequent values are around 20 and 5 respectively.

The motivation of the present work is to take the advantage of a very large sample to detect automatically SBs with more than one visible component¹ that are not always detected by the GES single-star main analysis pipelines. SBs may be a potential source of error when deriving atmospheric parameters and detailed abundances. This project presents (i) a new method to identify automatically the number of velocity components in each cross-correlation functions (CCFs) using their successive derivatives and (ii) the analysis of about 51 000 stars available within the GES internal data release 4 (iDR4).

In Sect. 2, we describe the iDR4 stellar observations, their associated CCFs and the selection criteria applied to them. The method on which the detection of the velocity components in a CCF relies, its parameters and the formal uncertainty are presented in Sect. 3. In Sect. 4, the set of SB n ($n \geq 2$) detected in iDR4 using this method is discussed, organized according to the stellar populations they belong to.

2. Data selection

2.1. Observations and CCF computation

Our analysis was performed on the iDR4 consisting of $\sim 260\,000$ single exposures (corresponding to $\sim 100\,000$ stacked spectra) of about 51 000 distinct stars observed with the FLAMES instrument feeding the optical spectrographs GIRAFFE (with setups HR3, HR5A, HR6, HR9B, HR10, HR14A, HR15N, HR15, HR21) and UVES (with setups U520 and U580) covering the optical and near-IR wavelength ranges given in Table 1.

The classical definition of a CCF function applied to the stellar spectra is:

$$\text{CCF}(h) = \int_{-\infty}^{+\infty} f(x)g(x+h) dx \quad (1)$$

where f is a normalised spectrum, g a normalised template spectrum and h is the lag expressed in km s^{-1} . The computation of the CCFs is performed by pipelines at CASU (Cambridge Astronomy Survey Unit²) for GIRAFFE spectra (Lewis et al., in prep.) and at INAF-Arcetri for UVES spectra (Sacco et al. 2014). For UVES CCFs, spectral templates from the library produced by de Laverny et al. (2012), and based on MARCS models (Gustafsson et al. 2008), are used. For GIRAFFE CCFs, spectral templates from the library produced by Munari et al. (2005), and based on Kurucz’s models (Kurucz 1993; Castelli & Kurucz 2003), are used. We stress that for a given spectrum, CCFs are calculated for all the templates and the CCF with the highest peak is selected. For UVES spectra, H α and H β are masked in the observations. As illustrated *e.g.* in Fig. 1, CCFs are characterized by a maximum value (CCF “peak”), a minimum value (lowest point of the CCF “tail”) and a full amplitude (maximum - minimum). The constant velocity steps of GIRAFFE and UVES CCFs are 2.75 (mainly) and 0.50 km s^{-1} (for a sampling of 401 and 4000 velocity points), respectively.

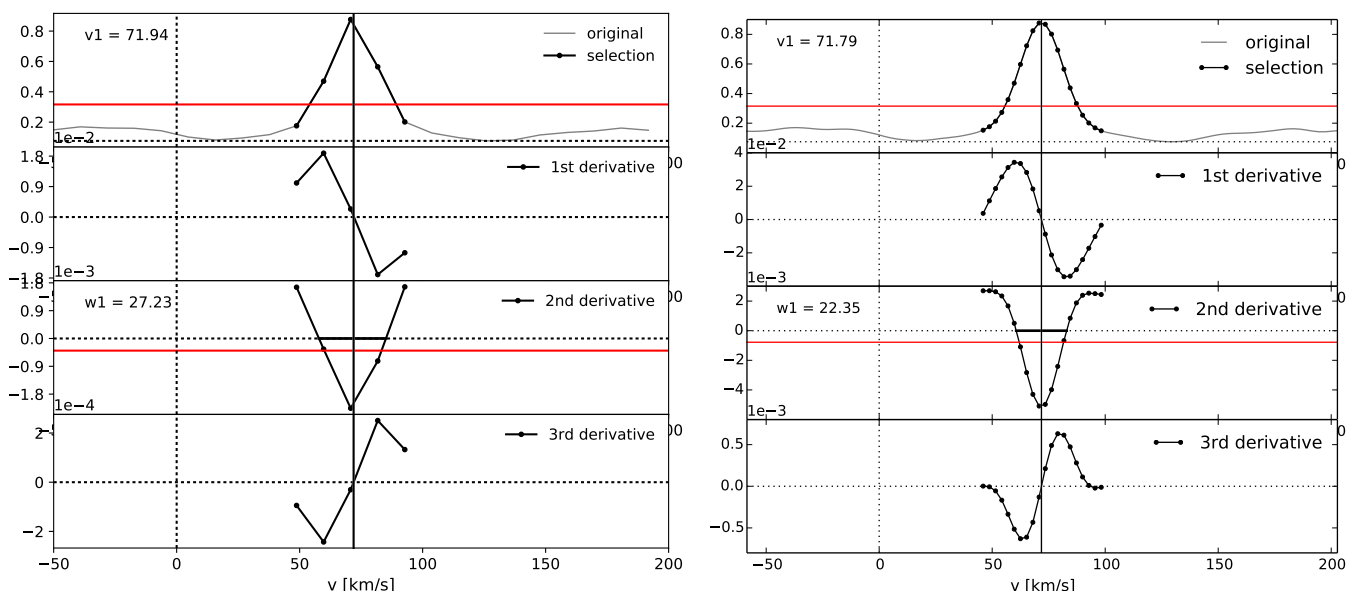
¹ Since SB1 systems require a special treatment by analyzing temporal series, their analysis should await the completion of the observations.

² <http://casu.ast.cam.ac.uk/gaiaeso>

* Based on data products from observations made with ESO Telescopes at the La Silla Paranal Observatory under programme ID 188.B-3002. These data products have been processed by the Cambridge Astronomy Survey Unit (CASU) at the Institute of Astronomy, University of Cambridge, and by the FLAMES/UVES reduction team at INAF/Osservatorio Astrofisico di Arcetri. These data have been obtained from the *Gaia*-ESO Survey Data Archive, prepared and hosted by the Wide Field Astronomy Unit, Institute for Astronomy, University of Edinburgh, which is funded by the UK Science and Technology Facilities Council.

Table 1. Setups used in GES and the associated estimated best parameters of the DOE code.

Instrumental setup	Spectral resolution	λ range [nm]	Main spectral features	THRES0 [%]	THRES2 [%]	SIGMA [km s ⁻¹]
UVES						
U520 low	47 000	420 – 520	G band, H γ , H β	35	8	5.0
U520 up	47 000	525 – 620	Fe I E, Na I D	35	8	5.0
U580 low	47 000	480 – 575	H β , Mg I b	35	5	5.0
U580 up	47 000	585 – 680	Na I D, H α	35	5	5.0
GIRAFFE						
HR3	24 800	403 – 420	H δ	55	8	3.0
HR5A	18 470	434 – 457	H γ	55	8	3.0
HR6	20 350	454 – 475	He I & II, Si III & IV, C III, N II, O II	55	8	3.0
HR9B	25 900	514 – 535	Mg I b, Fe I E	55	8	3.0
HR10	19 800	534 – 561	many weak lines	55	8	2.1
HR14A	17 740	631 – 670	H α	55	8	3.0
HR15N	17 000	645 – 681	H α , Li I	55	8	3.0
HR15	19 300	660 – 695	O ₂ A, Li I	55	8	3.0
HR21	16 200	849 – 900	Ca II triplet, Paschen lines	55	8	5.0


Fig. 1. Simulated CCF at limiting numerical resolution to test the computation of successive derivatives and the detection of the peak (left), and with a more realistic sampling (right). The spectrum used to simulate these CCFs has a radial velocity of 72.0 km s⁻¹ and $S/N = 5$.

Examples of spectra and CCFs in the setups mentioned above are displayed in Figs. 2 and 3. These figures are built from the solar and Aldebaran spectra. The CCFs are represented over the same velocity range to allow an easy comparison between the various setups. When a lot of weak absorption lines are present (as in setups HR6 and HR10), the CCF peak is narrow and well defined with a width smaller than for setups with strong features like H δ (HR3), H γ (HR5A), the Mg b triplet (HR9B), H α (HR14A and HR15N) and the Ca II triplet (HR21). For HR15, the presence of telluric lines from 685 nm onwards reduces the maximum amplitude of the CCF to a value as low as 0.25, even with a S/N larger than 1000.

For the UVES setups, Aldebaran (α Tau, spectral type K5III) spectra and corresponding CCFs are presented in Fig. 3. Each setup is composed of two spectral chunks. In the present case, the lower chunk comes with $S/N \approx 70$ and the upper one with

$S/N > 100$. For the setup U520 low, the leftward CCF tail is negative, probably as a result of poor spectrum normalisation due to the co-existence of lots of weak and strong lines. Since the wavelength range of the UVES setups is 2 or 3 times wider than those of GIRAFFE, the UVES setups are well suited to the detection of SB n candidates.

The final GES spectrum of a given object is a stack of all individual exposures, wavelength calibrated, sky subtracted and heliocentric radial velocity corrected. This could be a source of confusion in the case of composite spectra where the radial velocity of the different components changes between exposures. Moreover, a double-lined CCF coming from stacked spectra (and mimicking an SB2) can be the result of the SB1 combination taken at different epochs and stacked. To avoid this problem, we performed the binarity detection on the individual exposures (rather than on the stacked ones). This choice avoids spurious

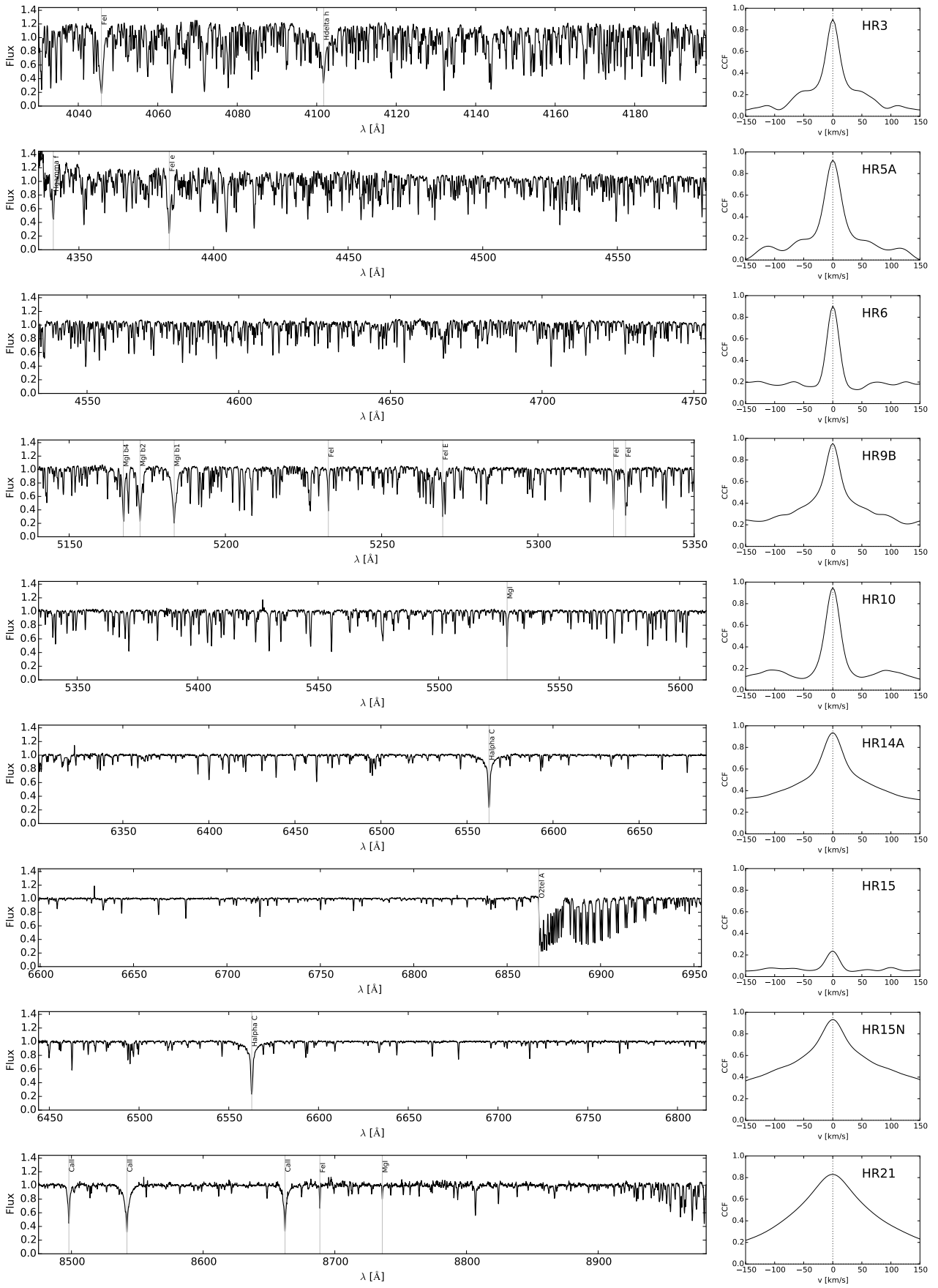


Fig. 2. Solar spectra acquired by GES in GIRAFFE setups with high S/N (> 1000) except for setup HR9B where $S/N \approx 700$. The normalised spectra are shown together with the identification of the main spectral features (left); the associated CCFs are shown on the right panels.

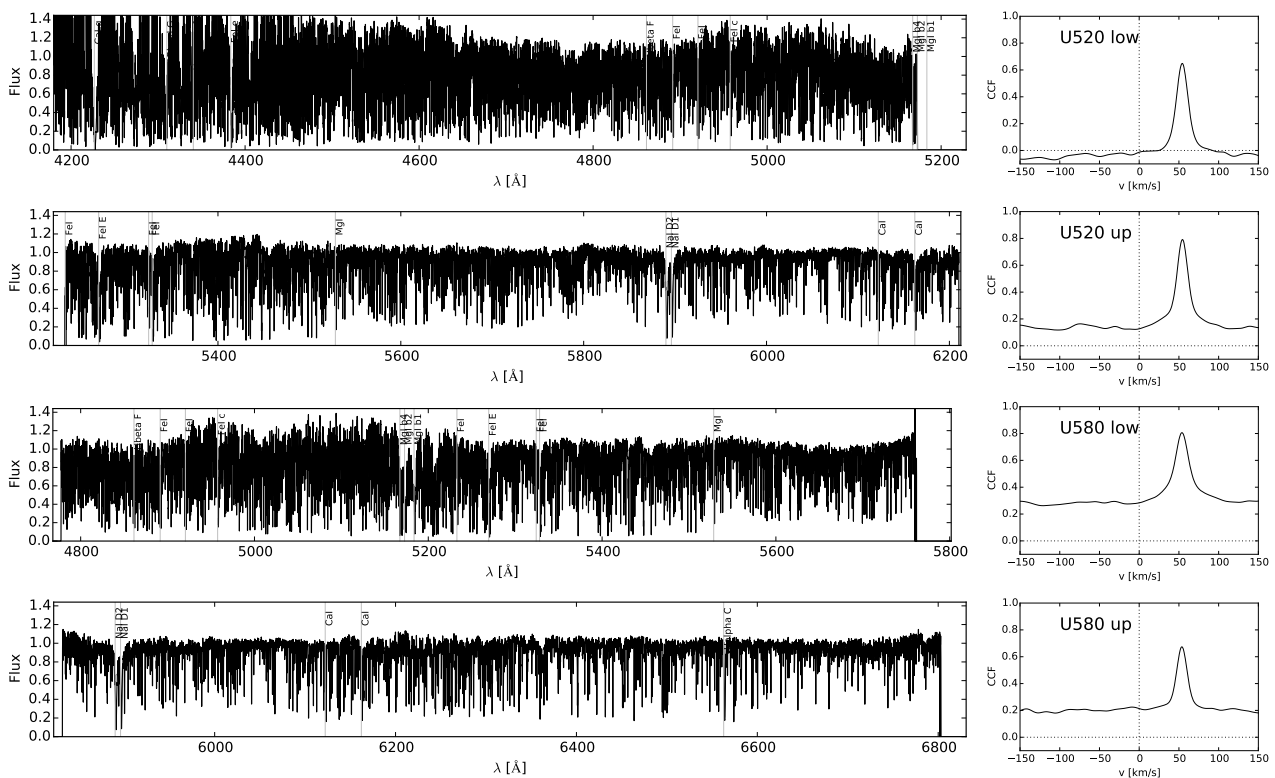


Fig. 3. Spectra of Aldebaran (α Tau) by GES in UVES setups with $S/N \approx 70$ for the low spectral chunks and $S/N > 100$ for the upper chunks.

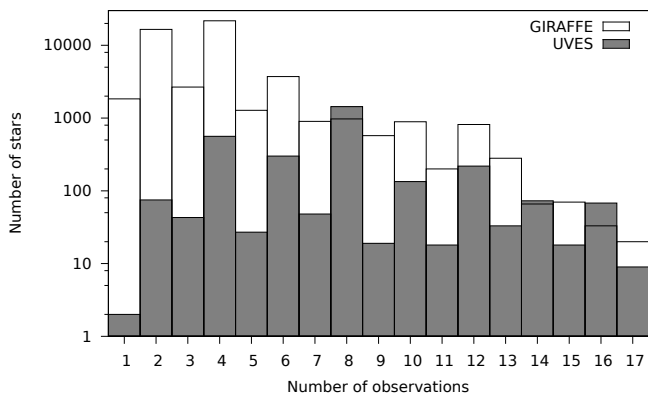


Fig. 4. Number of stars observed as a function of the number of observations per star. A tiny fraction, including benchmark stars, have a number of observations that can reach ~ 100 .

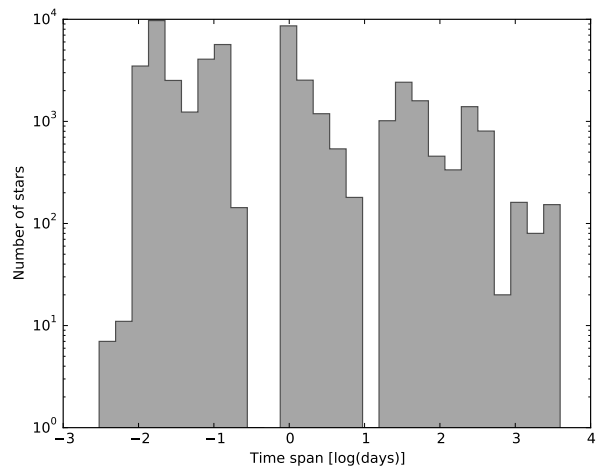


Fig. 5. Histogram of the full time span between observations if more than one is available for a given target.

spectroscopic binary detection, at the expense of using spectra with lower S/N ratios which will be shown not to be detrimental as long as $S/N > 5$ (see Sect. 3.4).

The number of individual observations per target is plotted in Fig. 4. The majority of stars observed with GIRAFFE has 2 or 4 observations because generally observed with HR10 and HR21 setups, whereas there are 4 or 8 observations in the case of UVES due to the presence of two spectral chunks per setup. Moreover, the time span between consecutive observations is very often less than three days, as shown on Fig. 5. Benchmark stars (*i.e.*, a sample of stars with well-determined parameters, to be used as reference; see Heiter et al. 2015a) are the most observed objects, some having more than 100 observations.

2.2. Data selection in iDR4

Our sample has been drawn from the individual spectra database of the GES iDR4³, covering observations until June 2014, to which the following selection criteria were applied:

- S/N larger than 5;
- CCF maximum larger than 0.15;
- CCF minimum larger than -1 ;
- CCF full amplitude larger than 0.10;
- left CCF continuum – right CCF continuum lower than 0.15.

³ GES public data releases may be found at <https://www.Gaia-eso.eu/data-products/public-data-releases>

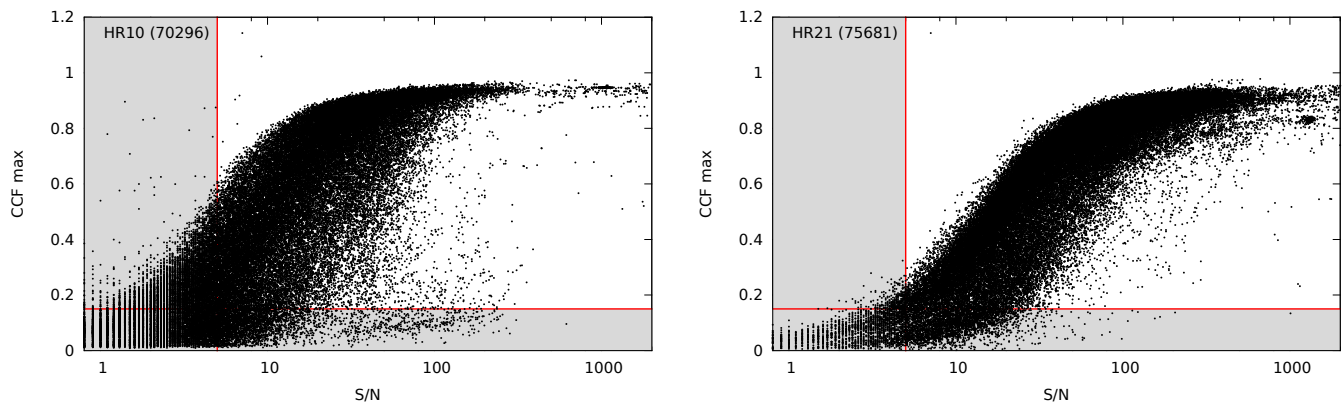


Fig. 6. CCF maximum amplitude versus S/N for HR10 (left panel) and for HR21 (right panel). Solid red lines are the criteria on the S/N (vertical, $S/N = 5$) and on the lowest value of the CCF maximum (horizontal, 0.15). The shadow area shows the observations excluded from the analysis. In parenthesis is the number of single exposures in each setup.

These criteria were empirically determined thanks to a visual inspection of a representative sample of CCFs. We allow negative values for the CCF minimum to keep CCFs computed on imperfectly normalised spectra (without allowing spectra with a completely wrong normalisation). Criteria on the S/N and on the CCF maximum are presented in Fig. 6 for setups HR10 and HR21 which contain the most numerous observations. This figure clearly shows the impact of the S/N of a spectrum on its associated CCF: the higher the S/N , the higher the CCF maximum. For a given S/N , the interval spanned by the CCF maximum is mainly due to spectrum – template mismatch. For HR10, the over-density located at $30 < S/N < 200$ and $CCF \max < 0.15$ is mainly due to NGC 6705 members. In HR21, the clump located at $1000 < S/N < 2000$ and $0.80 < CCF \max < 0.85$ is due to repeated observations of the solar spectrum.

These criteria allow us to avoid detecting spurious (noise-induced) CCF peaks. Over the 260 000 individual science spectra (corresponding to the 100 000 stacked spectra) within the iDR4, 9.3 % have a S/N lower than 5, 1.0 % have a null CCF (data processing issues), 7.8 % have a CCF maximum lower than 0.15, 0.2 % have a CCF minimum lower than -1.0 , and 0.02 % have a CCF full amplitude lower than 0.10. We ended up with about 205 000 CCFs (77.7 %), corresponding to ~ 51 000 different stars.

3. Methods

3.1. Detection of extrema (DOE) code

The Detection of extrema (DOE) code has been designed to identify the (local and global) extrema in a given signal even in case these extrema are strongly blended. By using successive derivatives of a function, it is possible to characterize it in a powerful way. Applied on spectral-line profiles for instance, the method makes it possible to identify all contributing blends (Sousa et al. 2007). Here we apply it to the CCFs. The method is inspired from signal-processing techniques (Foster 2013) which convolve the signal (here the CCF) with the derivatives of a Gaussian kernel to smooth and calculate the derivative of the CCF in a single operation. In other words, the first, second and third derivatives of the Gaussian kernel are used to obtain the smoothed derivatives of the CCFs. Indeed, one of the interesting properties of the convolution of two generalized functions is defined as follows:

$$(f' * g)(x) = (f * g')(x) \quad (2)$$

where f' and g' are the first derivatives of the generalized functions f and g . Convolution of the CCF with the derivative of a Gaussian kernel is equivalent to compute the derivative of the CCF and to convolve (*i.e.*, smooth) it by a Gaussian kernel. We use the routine `gaussian_filter1d` of the sub-module `ndimage` of the `scipy` module (Jones et al. 2001) in Python. The routine calculates first the derivative of the Gaussian kernel before correlating it with the CCF function. The width of the Gaussian kernel controls the amount of smoothing.

A zero in the descending part of the first derivative obviously provides the position of the maximum of the CCF. However, in the case of a CCF composed of two or more peaks, the zeros of the first derivative will only provide the positions of well-separated peaks, *i.e.*, peaks with a local minimum in between them. Blended peaks might thus be missed. However, this difficulty may be circumvented by using the third derivative, whose zeros occurring in an *ascending* part provide the positions of all the peaks including the blended ones. Fig. 7 shows that the use of the first derivative only does not allow a satisfactory detection of the CCF components. Indeed, although the CCF in the middle panel clearly exhibits two peaks, the first derivative has only one descending zero-crossing, thus resulting in the detection of one component only. However, the second derivative shows two local minima corresponding to the two CCF velocity components. The position of these two minima can be found by detecting the ascending zero-crossing of the third derivative. By using the third derivative, the different CCF components may thus be identified as regions where the CCF curvature is sufficiently negative (minima of the second derivative, or ascending zeros of the third derivative), separated by a region of larger curvature. To get the velocities of the various components, the CCF third derivative is simply interpolated to find its intersection with the x -axis. Some detection thresholds had to be set to automate the process in order to match the results obtained from an eye inspection of multiple-component CCFs.

The procedure is illustrated on simulated CCFs with or without two peaks (Figs. 1 and 7 respectively). We first test the operation of the DOE code on single peaks at the lowest numerical resolution, *i.e.*, peaks defined with only six velocity points (left panel of Fig. 1). The DOE code applied on a more realistic (more noisy) simulated single-peaked CCF (as shown on the right panel of Fig. 1) also provides satisfactory results, with an accuracy on the radial velocity of the order of 0.20 km s^{-1} . We will show in Sect. 3.4 that the DOE code has a small internal error of 0.25 km s^{-1} .

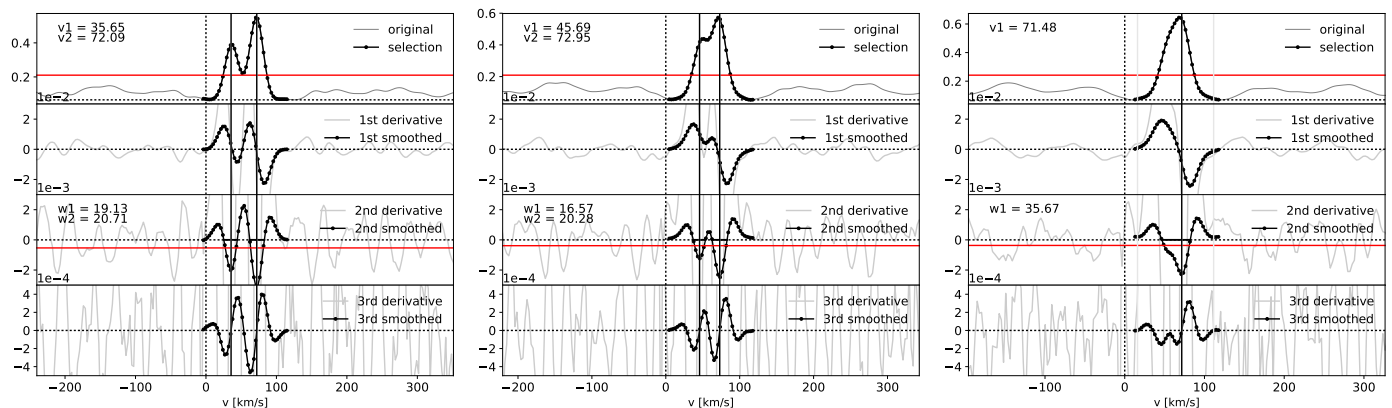


Fig. 7. Simulated noisy double-peak CCF with peaks located at 36.0 km s^{-1} and 72.0 km s^{-1} (left), 48.0 km s^{-1} and 72.0 km s^{-1} (centre), and 54.0 km s^{-1} and 72.0 km s^{-1} (right). Grey lines show derivatives from a simple finite differences method which have the drawback to be very noisy. Instead, black line with dots (in panels below the top one) show the smoothed derivatives computed with Eq. 2. Red lines in top panels show the threshold parameter on the CCF (THRES0) and in the middle-low panels the threshold parameter on the second derivative (THRES2).

The first threshold (THRES0), expressed as a fraction of the full CCF amplitude, defines the considered velocity range: the DOE code is applied only in the region where the CCF is larger than THRES0. The THRES0 threshold is represented by the horizontal red line in the top panels of Fig. 1 and subsequent figures. However, if several well-defined peaks are identified in the CCF, the THRES0 criterion is overridden, and all data points between the CCF peaks are included in the analysis of the derivatives, even though the CCF may be lower than THRES0.

A second threshold, THRES2, is set on the second CCF derivative. The THRES2 parameter is expressed as a fraction of the full amplitude of the CCF second derivative. This negative threshold is represented by the horizontal red line in the “2nd derivative” panel in Fig. 1 (and subsequent figures) such that only minima lower than this threshold are selected for the final peak detection (vertical black lines) whereas second-derivative minima larger than this threshold are not considered to be related to real components (vertical light grey lines in *e.g.* Fig. 9).

The width of the Gaussian kernel for the convolution of the CCF, SIGMA, is the third parameter. It is a smoothing parameter and aims at making the successive derivatives of the CCF less sensitive to the data noise.

The three parameters of DOE (THRES0, THRES2 and SIGMA) have to be set by the user. Their value may have an impact on the number of detected peaks and the radial velocities associated to them. These three parameters need to be adjusted in order to give meaningful results (*i.e.*, matching the efficiency of an eye-detection) on all CCFs, but once fixed for each instrumental setup (see Table 1 and Sect. 3.3), they are kept constant to ensure homogeneous detection efficiency over the whole GES sample.

The parameter values result from a compromise between antagonistic requirements:

- the THRES0 parameter must not be too low to avoid an unrealistically large velocity range, neither too high in order to be able to detect real albeit low secondary peaks;
- the THRES2 parameter must be calibrated on extreme cases (two very close or very separated peaks). The choice of this parameter is important: it ensures that the second derivative (*i.e.* the curvature) of the CCF is negative enough, therefore corresponding to real components;
- the SIGMA parameter must not be too large, resulting in a too strong smoothing which would endanger the detection of

close peaks, and not too small to reduce the impact of the numerical noise induced by the successive derivatives.

The empirical method used to set these parameters is described in Sect. 3.3.

3.2. Detection of peaks on simulated CCFs

We tested the efficiency of the DOE code on simulated double-peak CCFs. Using the radiative transfer code *turbospectrum* (Plez 2012; de Laverny et al. 2012), the MARCS library of model atmospheres with spherical geometry (Gustafsson et al. 2008) and the GES atomic linelist (Heiter et al. 2015b), we computed the synthetic spectrum of a star with the following stellar parameters: $T_{\text{eff}} = 5000 \text{ K}$, $\log g = 1.5$, $[\text{Fe}/\text{H}] = 0$. and $\xi_t = 1.5 \text{ km s}^{-1}$, between 5330 \AA and 5610 \AA for a resolution of $R \sim 20000$, *i.e.* to reproduce an HR10 spectrum (see Sect. 2.1). Then, we shifted this spectrum so that the radial velocity of this simulated star is $v_{\text{rad},0} = 72 \text{ km s}^{-1}$.

We also add a Gaussian noise to reproduce spectra with $S/N = 20$. Then we combine the spectra shifted at different radial velocities to simulate a composite spectrum. Assuming a flux ratio between the two components of $2/3$, we set the main peak at a fixed velocity of 72.0 km s^{-1} whereas the position of the second peak is set at either 36.0 , 48.0 or 54.0 km s^{-1} . The cross-correlation function between the composite and the initial spectrum is calculated and the CCF is normalised by the maximum value of the mask auto-correlation (auto-correlation of the initial spectrum).

The three simulated CCFs and their derivatives are shown on Fig. 7, the value of SIGMA being 2.1 km s^{-1} . From the first derivative, only one crossing of the x -axis leads to the detection of one single peak. From the second derivative, we see clearly two minima in the left and middle panel whereas we see only one minimum in the right panel. This leads to the conclusion that the detection limit between two components is 18 km s^{-1} . This detection limit depends on the typical width of absorption lines in the tested spectrum but also on the SIGMA parameter. However reducing the SIGMA parameter too much could increase false peak detections for bumpy CCFs. A compromise had to be adopted, as described in Sect. 3.3.

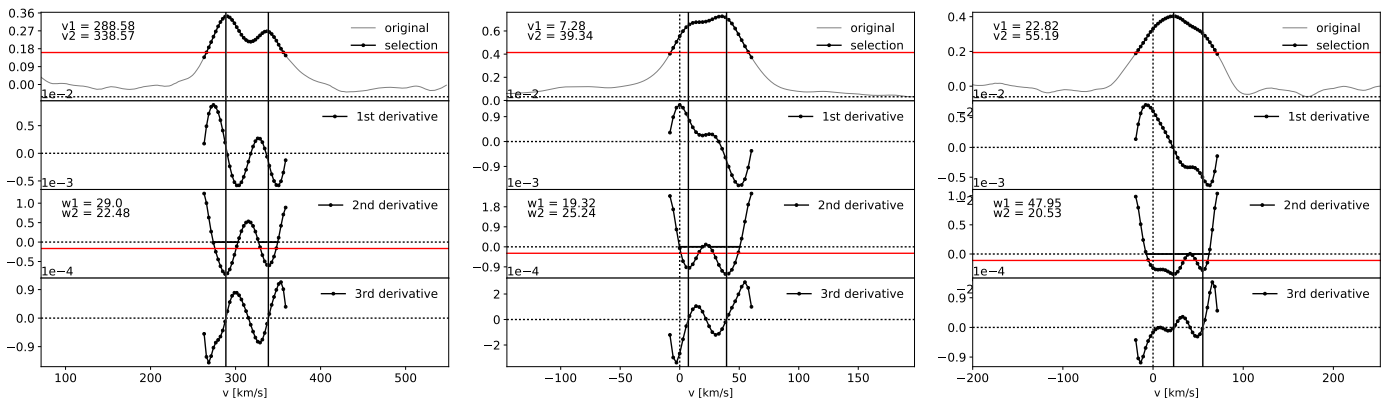


Fig. 8. Examples of iDR4 HR10 double-peak CCFs used to calibrate the parameters of the DOE code. These parameters (THRES0, THRES2 and SIGMA) have been fine-tuned in order to detect multiple components even when they are severely blended as in the case of the rightmost panel.

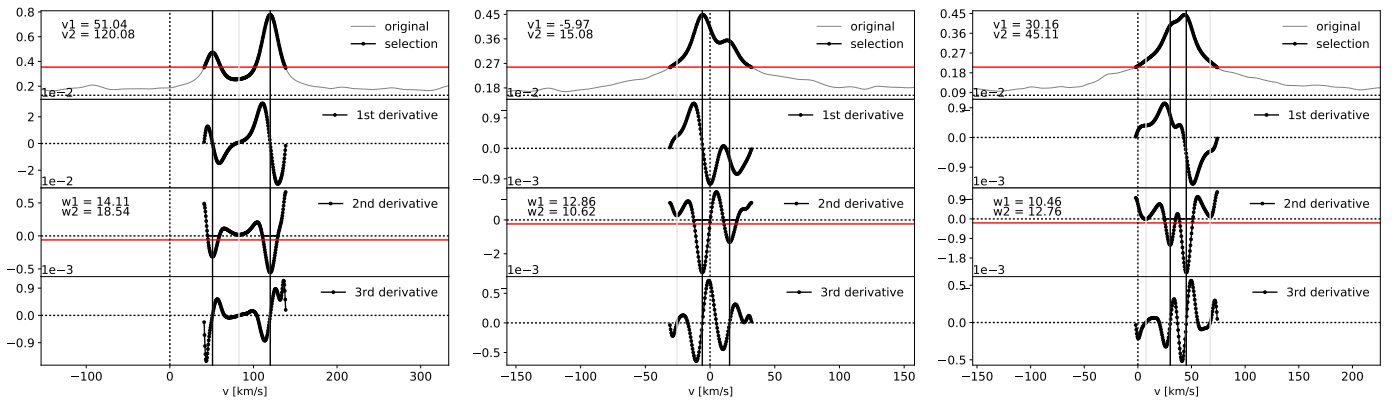


Fig. 9. As Fig. 8 but for the U580 setup.

3.3. Choice of the DOE parameters for the different setups

The three parameters of the DOE code described in Sect. 3.1 have to be adjusted to optimize the CCF components detection. These parameters were adjusted by performing individual calibrations for the different setups (GIRAFFE HR10, HR15N, HR21, and UVES U520 and U580) using examples of single-, double-, and triple-peak CCFs with different separations between the components, and different component widths (*i.e.* different degree of blending). For the remaining GIRAFFE setups, a standard value of the SIGMA parameter (3 km s^{-1}) was adopted. The adopted values are listed in Table 1. The parameter adjustment aims at obtaining the same detection efficiency on the test CCFs as through eye inspection, especially in the extreme cases (blended CCFs). Figures 8 and 9 illustrate favourable and extreme cases. The value of THRES0 is larger for the GIRAFFE CCFs than for the UVES ones because the correlation noise (*i.e.*, the signal level in the CCF continuum) was observed to be larger in GIRAFFE CCFs.

Depending on the setup resolution along with the number and strength of lines, the minimum separation for peak detection was empirically found to be in the range $[20\text{--}60] \text{ km s}^{-1}$ for GIRAFFE setups (15 km s^{-1} for UVES ones). As an example in Sect. 3.2 and Fig. 7, we showed with simulated CCFs that the detection limit is reached for a minimum separation of 18 km s^{-1} at $R \sim 20\,000$ for slowly rotating stars. The spectrograph resolution and the CCF sampling are not the only relevant parameters here, since the intrinsic line broadening (macroturbulence and stellar rotation) also impacts the CCF width.

DOE includes a procedure to compare the number of valleys in the second derivative with the number of detected peaks. When these numbers are not identical, iteration on the detection occurs after increasing the SIGMA parameter. This procedure prevents false detections since in these situations, the wide CCF often exhibits inflexion points which cause zeros in the third derivative (see left panels of Fig. 10). The number of valleys, defined as regions where the second derivative is continuously negative, is assessed first. For example, in the left “2nd derivative” panel of Fig. 10, one valley is detected. For low values of the SIGMA parameter, the number of detected velocity components is systematically larger than the number of valleys (left panels of Fig. 10). As long as the number of valleys is lower than the number of velocity components detected from the 3rd derivative, the SIGMA parameter is increased by 2 km s^{-1} , until the number of detected velocity components equals the number of valleys. The iterative process is then stopped and the radial velocities of the detected velocity components are identified.

Figure 10 shows an example of this procedure applied on the K1 pre-main sequence object 2MASS J06411542+0946396 (CNAME⁴ 06411542+0946396) member of the cluster NGC 2264 (Fűrész et al. 2006). The DOE run starts with the standard SIGMA value of 5 km s^{-1} . Initially, the DOE code detects three valleys in the second derivative and six velocity

⁴ By convention within the GES, the sources are referred to by a ‘CNAME’ identifier formed from the ICRS (J2000) equatorial coordinates of the sources. For instance, the J2000 coordinates of the source CNAME 08414659-5303449 are $\alpha = 8 \text{ h } 41 \text{ min } 46.59 \text{ s}$ and $\delta = -53^\circ 3' 44.9''$.

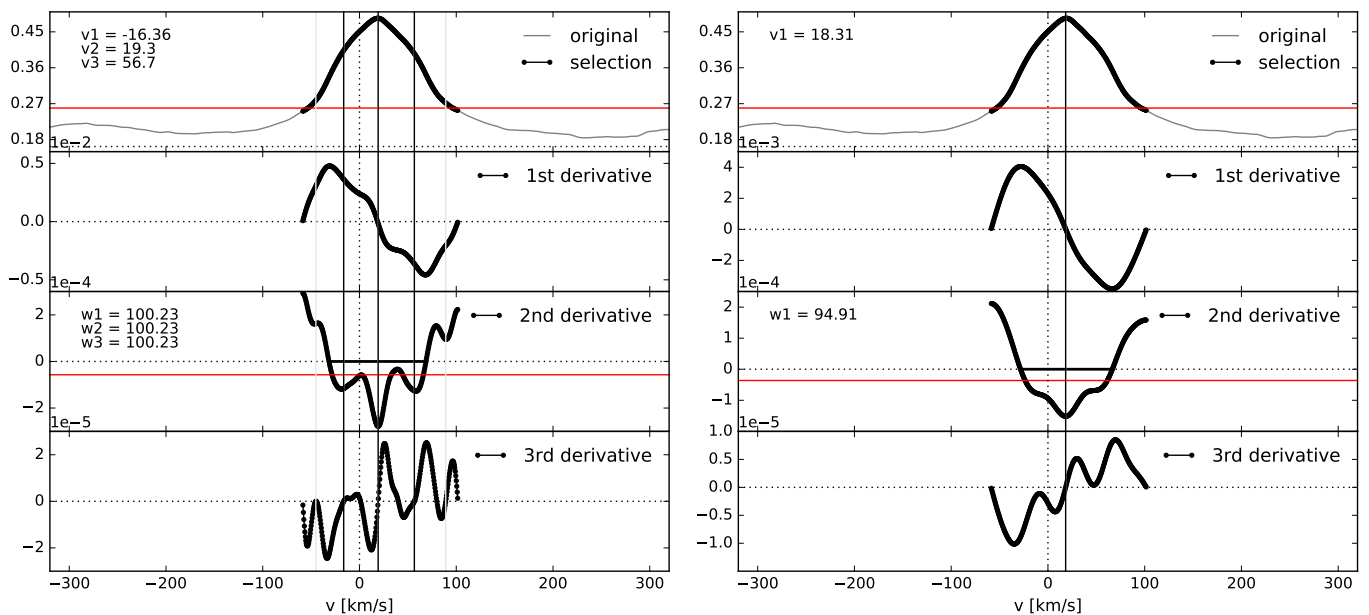


Fig. 10. Special procedure for fast rotators. Left panel: after few iterations three velocity components and one valley are detected. Right panel: after 11 iterations, one velocity component associated to one valley is identified. The associated spectrum has $S/N = 65$.

components from the third derivative, which are clearly spurious detections. After three iterations, one valley and three velocity components are identified (left panel of Fig. 10). After 11 iterations, SIGMA increases from 5 to 27 km s^{-1} and the process ends up with one velocity component located at 18.31 km s^{-1} (right panel of Fig. 10, to be compared with the velocity of 19.86 km s^{-1} found by Fűrész et al. 2006). The case of CCF multiplicity that can be due to physical processes different from binarity (like pulsating stars, nebular lines in spectra, etc.) is discussed in Sect. 4.7.

3.4. Estimation of the formal uncertainty of the method

In this section, we assess the choice of the SIGMA parameter and its effect on the derived radial velocities and their uncertainty. The uncertainty on the derived radial velocity for single-peak CCF depends mainly on the S/N of the spectrum used to compute the CCF, the normalisation of this spectrum and the mismatch between the spectrum and the mask (spectral type, atomic and molecular profiles, rotational velocity, etc.).

We performed Monte-Carlo simulations to compute single-peak CCFs from spectra of different S/N ratios but using the same atmospheric parameters defined in Sect. 3.2. We sliced this synthetic spectrum and degraded its resolution in order to match the following settings: GIRAFFE HR10 and HR21, UVES U520 and U580 (up and low). For each S/N level, we computed 251 realisations of our simulated GIRAFFE and UVES spectra by adding a Gaussian noise and computed the corresponding CCFs using a mask made of a noise-free spectrum with a null radial velocity. We finally ran DOE, with different values of SIGMA (from 1 to 15 by step of 1 km s^{-1}). Figures 11 and 12 show the difference $\Delta v_{\text{rad}} = v_{\text{rad,doe}} - v_{\text{rad,0}}$, where $v_{\text{rad,0}} = 72.0 \text{ km s}^{-1}$, as a function of the DOE parameter SIGMA (right panel) and the 251 CCFs (left panel) along with the noise-free CCF (labeled “ $+\infty$ ”). We show the results for the lowest S/N (*i.e.*, the most unfavorable cases) for the setups GIRAFFE HR10 and HR21 and UVES U580 (low and up). The mean and standard deviation of Δv_{rad}

are also superimposed with dark dots and error bars in the right panels.

Comparing the noise-free CCF (blue curve) in the left panels of Figs. 11 and 12 shows striking differences from one setup to the other. This is directly related to the spectral information contained by the spectrum used in the CCF computation. For our simulated star, the HR10 and U580 (low) spectra are more crowded than the HR21 and the U580 (up) spectra. This results in a higher level of the CCF continuum. In addition, in HR21, the large wings of the CCFs are due to the strong Ca II IR triplet that completely dominates this spectral range (see Fig. 2). Figures 11 and 12 also show that the spectral noise tends to shift downward the CCF in comparison to the noise-free CCF because the noisy spectra are less similar to the mask than the noise-free ones. In U580 (Fig. 12), we see that the distance between the noisy CCFs and the reference one is not similar in upper and lower left panels, despite the same S/N . This larger distance in U580 low compared to U580 up could be due to the fact that, for our simulated star, there are more weak lines in the low setup, and therefore, they quickly vanish in the noise when the S/N drops.

The right panels of Figs. 11 and 12 show the effect of SIGMA on the derived radial velocity (uncertainty and/or bias). Our simulations clearly demonstrate that SIGMA has to be chosen in a specific range to ensure reliable results. While our simulated UVES CCFs show that the DOE performance is very stable for any value of SIGMA, our simulated GIRAFFE CCFs show that only a limited range of SIGMA values can ensure reliable velocity measurements. Figure 11 suggests to keep SIGMA between ~ 2 and $\sim 8 \text{ km s}^{-1}$ for HR10 and ~ 2 and $\sim 7 \text{ km s}^{-1}$ for HR21, in agreement with our empirical calibration on a sub-sample of real GES CCFs (see Table 1). The behavior of DOE, while varying SIGMA, is different for GIRAFFE and UVES CCFs (Figs. 11 and 12). This is not due to the S/N ratio but rather to the sampling of the velocity grid onto which the GIRAFFE and UVES CCFs are computed, *i.e.* SIGMA is related to the velocity step of the CCFs. Indeed, in Sect. 2.1, we recalled that the sampling frequency of the CCF is lower for GIRAFFE CCFs than for UVES CCFs: as SIGMA increases, a pronounced asymmetry on the

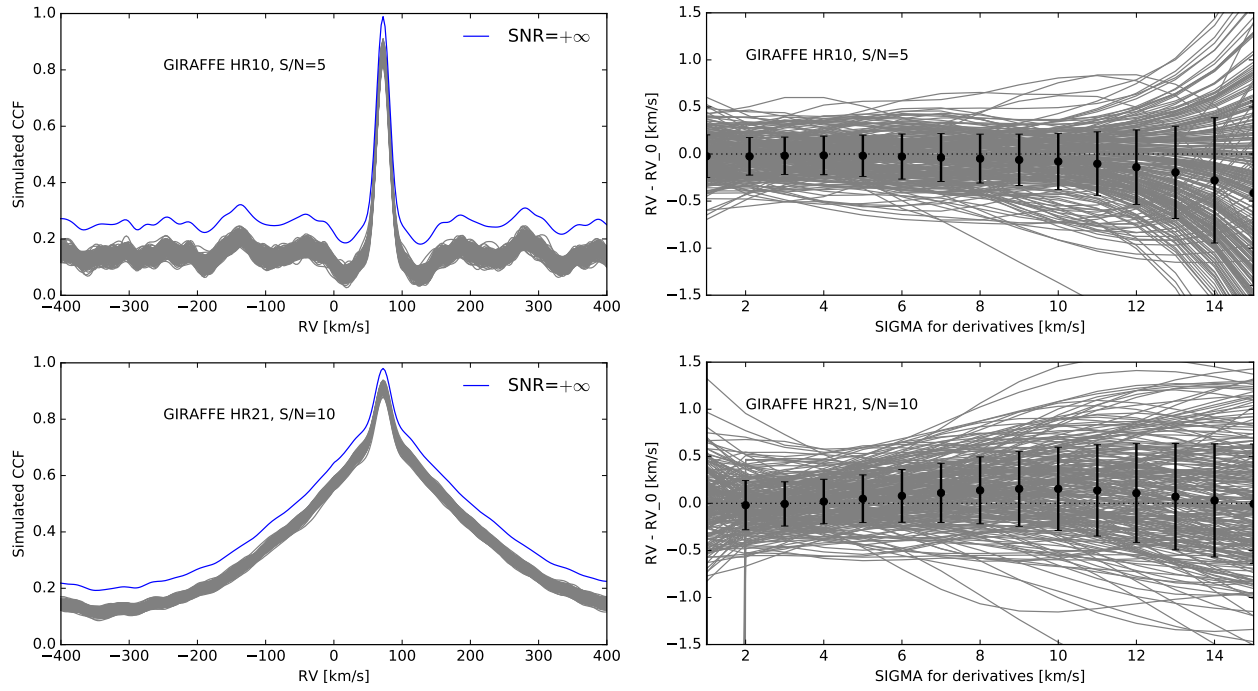


Fig. 11. Estimation of the accuracy of the radial velocities determined by the DOE code on GIRAFFE setups HR10 and HR21 (Ca II triplet region). In each case, 251 simulated CCFs with a S/N ratio as labelled and the blue line representing a noise-free CCF (left panels) were analyzed with DOE varying the value of SIGMA for the calculation of the smoothed successive derivatives and of the radial velocity (right panels).

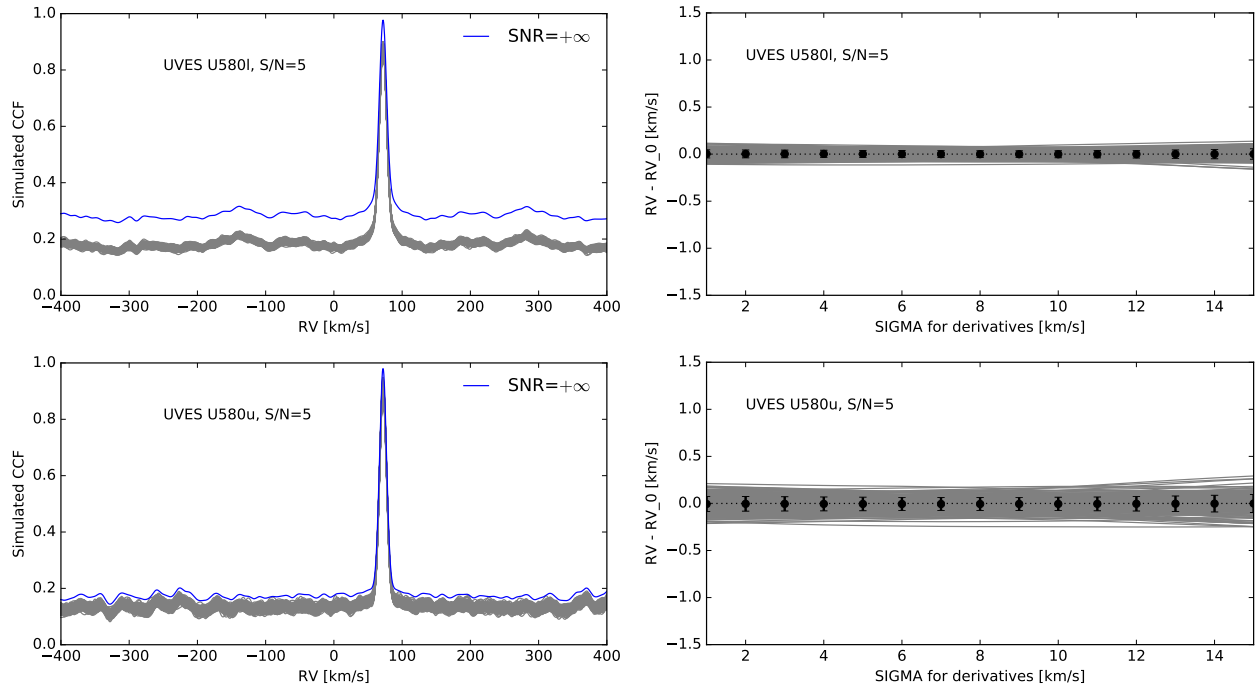


Fig. 12. Same as Fig. 11 for the UVES setups U580 low ($H\beta + \text{Mg I b}$ triplet region) and U580 up ($H\alpha + \text{Na I D}$ doublet region).

second derivative appears for GIRAFFE CCFs, resulting in the high scatter displayed by Fig. 11.

Our simulations allow us to quantify the effect of the S/N of the spectra on the method. For U520 and U580, the standard deviation on the radial velocity at the recommended SIGMA goes from 0.05 km s^{-1} at $S/N = 5$ to lower than 0.01 km s^{-1} at $S/N = 50$. For GIRAFFE HR10, it goes from 0.20 km s^{-1} at $S/N = 5$ to 0.02 km s^{-1} at $S/N = 50$. For GIRAFFE HR21, the

situation is the worst of all the setups with a standard deviation going from 0.25 km s^{-1} at $S/N = 10$ to 0.06 km s^{-1} at $S/N = 50$. The obvious conclusion is that the UVES setups tend to give more precise results for a given S/N compared to GIRAFFE setups. This is understandable since a single UVES spectrum has a higher resolution and a wavelength coverage larger than any GIRAFFE spectrum. For our simulated star, the precision on the radial velocity derived by DOE is up to five times higher for UVES

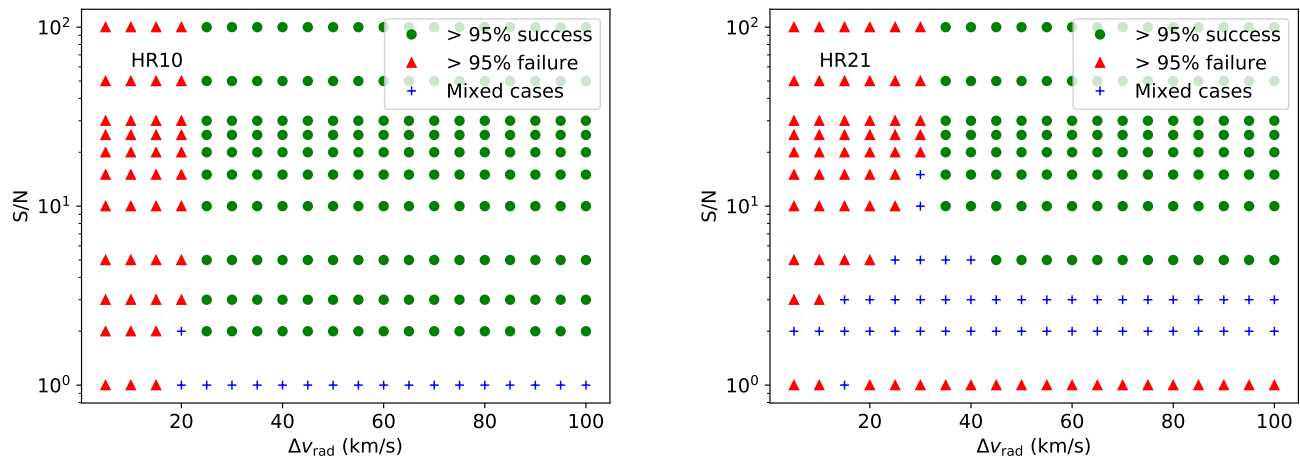


Fig. 13. Assessment of the DOE detection efficiency of the two radial velocity components of simulated SB2 CCFs as a function of the S/N ratio and the radial velocity differences for GIRAFFE HR10 (left panel) and HR21 (right panel) setups.

setups than for GIRAFFE HR10 (this is even worse when compared with HR21).

This first approach of simulated CCFs shows that the method is quite robust with respect to the noise level in the GES spectra. Obviously, the presence of multiple components in the CCF may shift the detected radial velocities especially when the peaks blend one another. In such a case, the inaccuracy on the radial velocity can reach several km s^{-1} (increasing as the blending degree increases). No quantitative calculations have been performed so far but the middle panel of Fig. 7 shows a good illustration: the main peak is detected at 0.95 km s^{-1} of its expected position and the second peak at 2.3 km s^{-1} , with a simulated distance of 24 km s^{-1} between the two peaks. We conclude that the (conservative) random uncertainty on the radial velocity derived by DOE is of the order of $\pm 0.25 \text{ km s}^{-1}$ while the systematic uncertainty is lower than 0.05 km s^{-1} for single-peak CCF and may reach a few km s^{-1} for multi-peak CCF. Other effects, like template mismatch or imperfect normalisation, may have an effect on the uncertainty on the derived radial velocity. We also refer the reader to Jackson et al. (2015) where a discussion on the radial velocity uncertainties may be found, along with their empirical calibrations as a function of S/N , $v \sin i$ and the effective temperature of the source for GIRAFFE HR10, HR15N and HR21 setups. As shown by Sacco et al. (2014) and Jackson et al. (2015), the errors on the GES radial velocities for most of the stars are dominated by the zero-point systematic errors of the wavelength calibration that are not discussed here.

3.5. Detection efficiency as a function of the S/N ratio

Using Monte-Carlo simulations, we assessed the impact of the S/N ratio of GIRAFFE HR10 and HR21 spectra on the detection efficiency of the double-peaked CCF of an SB2. For that purpose we simulated synthetic SB2 spectra (pair of twin stars) varying the S/N (from 1 to 100) and varying the difference in radial velocity of the two components Δv_{rad} (from 5 to 100 km s^{-1}). For each pair (Δv_{rad} , S/N), we computed as above 251 realisations of the spectra and their corresponding CCFs. We then applied DOE with the parameters adapted to each setup (see Table 1).

The maps in Fig. 13 show the detection efficiency in HR10 and HR21. The green dots (respectively the red triangles) indicate (Δv_{rad} , S/N) conditions when DOE is able to detect the two

expected peaks in more than 95% of cases (respectively, conditions when DOE failed at detecting the two expected peaks in more than 95% of cases). Blue pluses represent intermediate cases making detection efficiency dependent on the noise: due to the noise, spurious peaks may appear (*i.e.* detection failed) or the two peaks have different height (despite being twin stars) and become discernible to DOE for small Δv_{rad} (*i.e.* detection succeeded; *e.g.*, for HR21, at $S/N = 10$ and $\Delta v_{\text{rad}} = 25 \text{ km s}^{-1}$).

These simulations demonstrate that even spectra with very low S/N carry sufficient information to reveal the binary nature of the targets. Specifically, in the HR10 setup, double peaks are detected in 95% of cases when $S/N \geq 2$ and $\Delta v_{\text{rad}} \geq 25 \text{ km s}^{-1}$ while in HR21 setup, they are detected at the same rate when $S/N \geq 5$ and $\Delta v_{\text{rad}} \geq 45 \text{ km s}^{-1}$. Thus, the S/N threshold that we adopted (*i.e.* analysis of CCFs for all spectra with $S/N \geq 5$) protect us from mixed cases, which tend to happen for the lowest levels of S/N ratios. This shows also that the HR10 setup is more suitable to detect SB2 than HR21 because HR21 is located around the IR Ca II triplet whose lines have strong wings that decrease the detection efficiency. In Sect. 4.2, the histogram of the radial velocity separation of the effectively detected SB2 candidates is presented. Observationally, HR10 spectra (respectively, HR21) allow us to detect SB2 with Δv_{rad} as low as $\sim 25 \text{ km s}^{-1}$ (respectively, $\sim 60 \text{ km s}^{-1}$): thus for both setups we are dealing with cases falling in the green dotted area of the maps. Thus, we expect in all cases an SB2 detection efficiency better than 95%.

4. iDR4 results and discussion

The DOE code is included in a specifically designed workflow to handle all the GES single-exposure spectra for all setups. The automated workflow includes three steps: first, the CCFs are selected using the set of criteria described in Sect. 2.2; second, the DOE code is applied to the CCFs to identify the number of peaks and a confidence flag is assigned; third, the CCFs in a given setup are combined per star and a last criterion is applied: for a given star, if more than 75% of the CCFs in at least one setup show 2 peaks (respectively 3 and 4), then the star is classified as SB2 candidate (SB3 and SB4 respectively). This rather restrictive criterion (see Sect. 4.7) was adopted to prevent false positive SB

Table 2. Number of SB2, SB3 and SB4 candidates per confidence flag.

Peculiarity index	Confidence flag			Total
	A	B	C	
SB2 (2020)	127	107	108	342
SB3 (2030)	7	1	3	11
SB4 (2040)	1	0	0	1

Notes. A: probable, B: possible, C: tentative

detections (due to spectra normalisation, cosmics, nebular lines, etc.).

After this automatic procedure, a visual inspection is performed to ensure that (i) no false positive detection remains (ii) the confidence flag is relevant. We investigate the CCFs and the spectra of all the SB n candidates one by one. When a clear false detection is encountered, the SB candidate is removed from the list. When an SB was flagged by the automatic process as probable (A) or possible (B), but the visual inspection of the CCF series (all setups considered) casts doubts on this classification, the corresponding spectra for that object are inspected. The choice of the final flag for an object can be downgraded in case other CCFs provide discrepant results. Such a procedure ensures that processes other than binarity moderately contaminate SB candidates flagged C, marginally contaminate SB candidates flagged B and exceptionally contaminate those flagged A. Despite these difficulties, adopting clear classification criteria ensures the best possible consistency throughout the survey.

The SB n candidates reported in the present paper are much fainter on average than those already collected in the *Ninth Catalogue of Spectroscopic Binary Orbits* (SB9; Pourbaix et al. 2004) (Fig. 14). The average visual magnitude of SB2 within the SB9 catalogue is around $V \sim 8$. For the GES SB2 candidates, the average is $V \sim 15$. The *Gaia*-ESO program targets both Milky Way field stars and stars in open and globular clusters. We refer the reader to Stonkutė et al. (2016) for the selection function of Milky Way field stars (excluding the bulge stars), to Bragaglia (2012) and Bragaglia et al. (in prep.) for the selection criteria in open clusters, and to Pancino et al. (2017) in globular clusters and calibration open clusters. We emphasize that the targets observed in regions like the bulge, Cha I (Sacco et al. 2017) and γ^2 Vel (Prisinzano et al. 2016) associations, as well as ρ Oph (Rigliaco et al. 2016) molecular cloud are selected on the basis of coordinates and photometry (VISTA and 2MASS), thus providing a rough membership criterion.

The list of the SB2 and SB3 candidates in the Milky Way field is given in Tables A.1 and A.2. The list of SB2 in the bulge, the Cha I, γ^2 Vel and ρ Oph associations and the CoRoT field is given in Table B.1. Finally, the list of SB n in stellar clusters is given in Table C.1. The results (classification and confidence flag) are included in the GES public releases (see footnote 3) using the nomenclature as described in the GES outlier dictionary developed by the GES Working Group 14 (WG 14)⁵.

⁵ The aim of WG 14 is to identify non-standard objects which, if not properly recognised, could lead to erroneous stellar parameters and/or abundances. A dictionary of encountered peculiarities has been created, allowing each node to flag peculiarities in a homogeneous way.

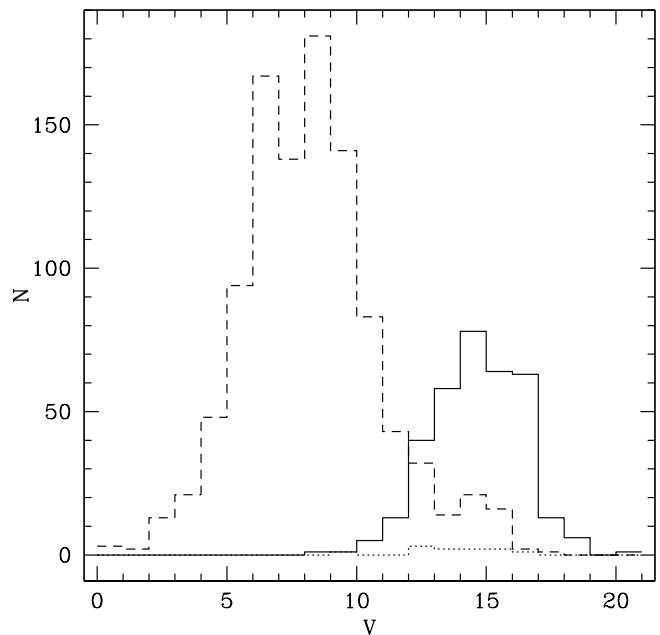


Fig. 14. Magnitude distributions of SB2 systems in the *Ninth Catalogue of Spectroscopic Binary Orbits* (SB9 Orbits; Pourbaix et al. 2004, data downloaded in September 2016 from <http://sb9.astro.u1b.ac.be>, and in the GES (solid line). SB3 systems are shown as the dotted-line histogram.

4.1. The binary classification⁶

The binary classification⁶ has been developed for the GES within WG 14. The following scheme is adopted: the peculiarity flag is built from the juxtaposition of a peculiarity index, and a confidence flag letter. The peculiarity index is defined as $20n0$, with $n \geq 2$, where n is the number of distinct velocity components in the CCF. With this peculiarity index, an SB2 is classified as 2020, an SB3 2030, etc. Of course, even though a star is flagged 2020 (*i.e.* SB2), a third component may be present but not visible during the observation or undetectable with the resolution and S/N of the considered exposure.

Moreover, the WG14 dictionary recommends the use of confidence flags (A: probable, B: possible, and C: tentative). Clearly, the closer the CCF peaks are, the less certain the detection is. The criteria to allocate these flags were defined as follows:

- A: the local minimum between peaks is deeper than 50% of the full amplitude of the largest peak;
- B: the local minimum between peaks is higher than 50% of the full amplitude of the largest peak;
- C: no local minimum is detected between peaks but the CCF slope changes.

With these definitions, the SB2 whose CCF is plotted on the left, middle and right panels of Figs. 8 and 9 would be flagged as A, B and C respectively.

For triple-peak CCFs, the same type of criterion is applied to the second local minimum. If this second local minimum is lower than 70% of the full amplitude of the largest peak, then the confidence flag is set to A, else, B. Examples of these two cases are shown on simulated CCFs in Fig. 15. The CCF on the middle panel is classified as 2030B (due to the fact that the leftmost

⁶ See note 3

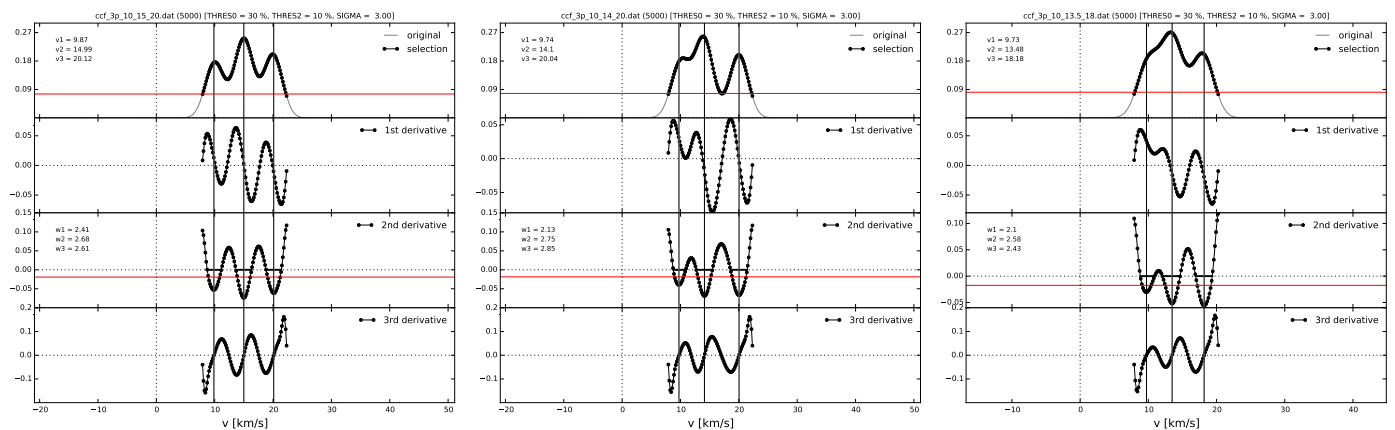


Fig. 15. Triple-peak simulated CCFs with a main peak fixed at 10 km s^{-1} detected with confidence flags A (left; second and third peaks at 15 and 20 km s^{-1}), B (middle; second and third peaks at 14 and 20 km s^{-1}) and C (right; second and third peaks at 13.5 and 18 km s^{-1}).

local minimum is higher than 0.5 times the largest amplitude) but also as 2020A because the middle and leftmost peaks, taken as a whole, are well separated from the rightmost peak.

4.2. *iDR4 SB2 candidates*

Table 2 presents the breakdown of the detected SB_n candidates in terms of confidence flags, whereas Table 3 provides the detailed results of the analysis per field, in terms of automated detection (‘DOE’ column) and after visual checking (‘confirmed’ column). A total of 1092 sources were identified as SB_2 candidates by the automated procedure described in the previous section, out of which 342 are confirmed after visual inspection, giving a success rate of about 30% similar to that of Matijević et al. (2010) for the RAVE survey. Typical rejected cases include distorted CCFs caused by negative fluxes or pulsating stars. Some confidence flags were also changed during the visual inspection phase (see Sect. 4.7). The largest number of stars has been observed with the GIRAFFE setup HR21 because it corresponds to the *Gaia* wavelength range of the radial velocity spectrometer. However, the rate of SB_n detection in this setup is very low because it is dominated by the presence of the Ca II triplet, which is a very strong feature in late-type stars, thus resulting in a broad CCF that can mask possible multiple peaks (Fig. 2, bottom panel). Moreover, emission in the line cores of this triplet induces fake double-peak CCFs because in the templates the lines are always in absorption. Consequently, it is very difficult to identify double peaks due to binarity based on HR21 CCFs (see Sect. 4.7 for more details). This explains why we have only two firm detections among the 31 970 stars observed with this setup only. Hence, this setup is not well-suited to detect stellar multiplicity at least in our situation (see Matijević et al. 2010: though they could discover 123 SB_2 out of 26 000 RAVE targets, they also had to deal with very broadened CCFs and could not detect binaries with $\Delta v_{\text{rad}} \leq 50 \text{ km s}^{-1}$).

The setup with the second largest number of observed objects is HR10. This setup covers the range [535–560] nm with lots of small absorption lines that result in a narrow CCF, suitable for the detection of stellar multiplicity (see Fig. 8). The largest number of probable SB_2 candidates is indeed detected with this setup.

To illustrate the fact that some setups are more adapted than others to detect SB_n , we show spectra and CCFs in these setups for single stars (the Sun and Arcturus in Figs. 2 and 3) and for an SB_2 candidate (NGC 6705 1936 observed in most of the GI-

RAFFE setups where the composite nature of the spectrum is clearly visible in Fig. 16).

Contrary to field stars which are observed in HR10 and HR21 only, cluster stars were observed with many different setups. The number of SB_2 candidates in the field is 185 out of 27786 stars (0.67%) whereas in the clusters, it amounts to 127 out of 16468 (0.77%, see Table 3).

There are about 30 SB_2 candidates detected with a double-peaked CCF in both GIRAFFE HR10 and HR21. For instance, the field star 02394731-0057248 (magnitude $V = 13.8$) is identified as an SB_2 candidate with HR10 and HR21 (see Fig. 17). This new candidate has no entry in the Simbad database.

The histograms of the radial velocity separation of SB_2 candidates for GIRAFFE HR10 and HR21 as well as for UVES U580 are shown on Fig. 18 (U520 is not represented due to the small statistics). The smallest measured radial velocity separations are 23.3, 60.9 and 15.2 km s^{-1} for HR10, HR21 and U580, respectively. This is well in line with the detection capabilities of the DOE code as mentioned in Sect. 3.3 ($\sim 30 \text{ km s}^{-1}$ for GIRAFFE and $\sim 15 \text{ km s}^{-1}$ for UVES setups). In U580, the high bin value around 72 km s^{-1} is mainly due to the repeated observations of a specific object, the SB_4 candidate 08414659-5303449 in IC 2391 (see Sect. 4.5).

Concerning the SB_2 candidates in open clusters, not only did we check the cleanliness of the SB_2 CCF profile, but we also compared the velocities of the two peaks with the cluster velocity. Assuming that most of the SB_2 systems discovered by GES generally have components of about equal masses, then, an SB_2 being member of the cluster should have the cluster velocity about midway between the two component velocities. This simple test allows us to assess the likelihood that the SB_2 system is a cluster member. This method is applied in full details for the SB_2 , SB_3 and SB_4 candidates analyzed in the present section and Sects. 4.4 and 4.5. The results are shown in Table C.1. The numbers of *bona fide* SB_2 candidates retained per cluster after this check are listed in the corresponding column of Table 3. The column labeled ‘Member’ in Table C.1 evaluates the likelihood of cluster membership based on the component velocities: if the cluster velocity falls in the range encompassed by the component velocities, we assume that the centre of mass of the system moves at the cluster velocity, so that membership is likely. In that case, we put ‘y’ in the column ‘Member’. On the contrary, if the CCF exhibits two well-defined peaks not encompassing the cluster velocity, the star is labeled as SB_2 not member of the cluster (‘n’ in column ‘Member’). Another possibility is that one

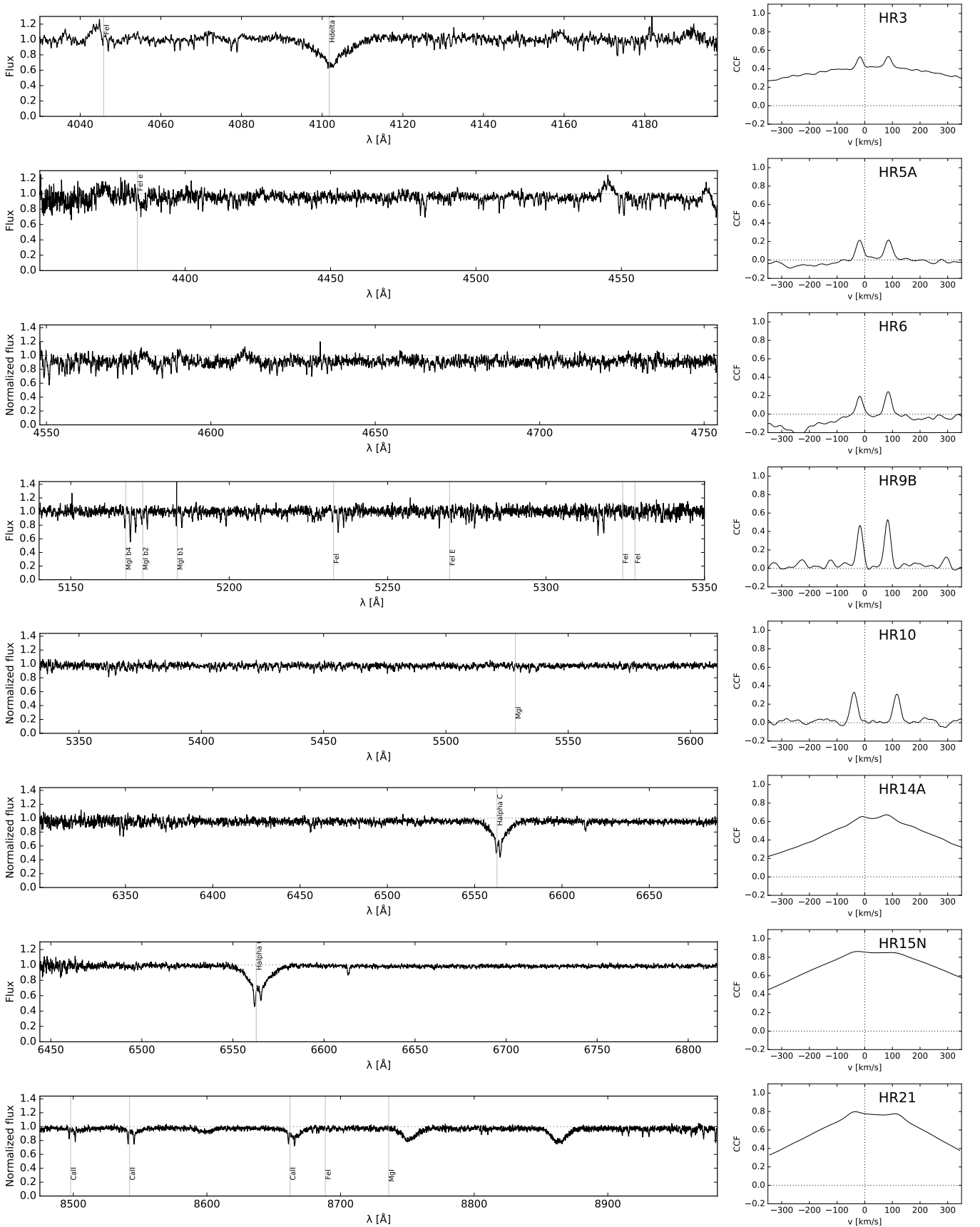


Fig. 16. Examples of composite spectra and CCFs associated with the new SB2 candidate 18503230-0617112 classified 2020A (NGC 6705 1936) with a visual magnitude of $V = 13.4$ ($B - V \sim 0$). Broad emission lines in HR3, HR5A and HR6 are spill-over from strong Ar lines from a Th-Ar calibration lamp observed along with the target.

Table 3. Distribution of SB2 and SB3 candidates among the different observed fields.

Field/cluster	log age [yr]	v_r [km s ⁻¹]	# stars	# SB2					# SB3					SB2/total [%]	SB3/SB2 [%]
				DOE	confirmed	A	B	C	DOE	confirmed	A	B	C		
Field			27786	263	185	82	48	55	24	5	5			0.67	3
Bulge			2633	6	6	1	3	2	0	0				0.23	
Cha I			616	5	2		2		1	0				0.49	
Corot			1966	13	7	5	2		0	0				0.36	
γ^2 Vel			1116	28	16	2	7	7	2	0				1.43	
ρ Oph			278	2	1			1	1	0				0.72	
IC 2391	7.74	14.49 ± 0.14	398	4	3	2	1		4	0				0.75	
IC 2602	7.48	18.12 ± 0.30	1784	6	3	1	1	1	3	0				0.17	
IC 4665	7.60	-15.95 ± 1.13	559	6	5	2	2	1	1	0				0.89	
M 67	9.60	33.8 ± 0.5	25	4	4	4			0	0			16.00		
NGC 2243	9.60	59.5 ± 0.8	715	38	1		1		14	0				0.14	
NGC 2264	6.48	24.69 ± 0.98	1565	78	4	2	2		18	0				0.26	
NGC 2451	7.8 (A) 8.9 (B)	22.70 (A) 14.00 (B)	1599	18	11	3	5	3	7	1	1			0.69	9
NGC 2516	8.20	23.6 ± 1.0	726	19	8	1	4	3	10	1		1		1.10	13
NGC 2547	7.54	15.65 ± 1.26	367	7	1	1			3	0				0.27	
NGC 3293	7.00	-12.00 ± 4.00	517	158	9	1	5	3	55	0				1.74	
NGC 3532	8.48	4.8 ± 1.4	94	1	1		1		0	0				1.06	
NGC 4815	8.75	-29.4 ± 4	174	11	2		1	1	0	0				1.15	
NGC 6005	9.08	-24.1 ± 1.3	531	12	4	2	1	1	8	1	1			0.75	25
NGC 6530	6.30	-4.21 ± 6.35	1252	95	5	2		3	1	0				0.40	
NGC 6633	8.78	-28.8 ± 1.5	1643	17	15	3	7	5	0	0				0.91	
NGC 6705	8.47	34.9 ± 1.6	994	108	19	5	3	11	52	1	1			1.91	5
NGC 6752	10.13	-24.5 ± 1.9	728	8	1		1		0	0				0.14	
NGC 6802	8.95	11.9 ± 0.9	156	7	2	2			7	1		1		1.28	50
Tr 14	6.67	-15.0	858	82	3	2	1		19	0				0.35	
Tr 20	9.20	-40.2 ± 1.3	1316	84	19	3	7	9	24	1		1		1.44	5
Tr 23	8.90	-61.3 ± 0.9	164	5	1	1			5	0				0.61	
Be 25	9.70	+134.3 ± 0.2	38	2	2		2		1	0				5.26	
Be 81	8.93	48.3 ± 0.6	265	5	2	1		1	6	0				0.75	
Total			50863	1092	342	128	107	107	266	11	7	1	3	0.68	3

Notes. The column ‘log age’ lists the logarithm of the cluster age (in years) from Cantat-Gaudin et al. (2014) (NGC6705), Spina et al. (in prep.) (IC 2391, IC 2602, IC4665, NGC 2243, NGC 2264, NGC 2541, NGC 2547, NGC 3293, NGC 3532, NGC 6530), Bellini et al. (2010) (M 67), Bragaglia & Tosi (2006) (NGC 2243), Sung et al. (2002) (NGC 2516), Friel et al. (2014) (NGC 4815), Jacobson et al. (2016) (NGC 6005, NGC 6633), VandenBerg et al. (2013) (NGC 6705), Tang et al. (submitted) (NGC 6802), Donati et al. (2014) (Tr 20 and Berkeley 81, written Be 81), Overbeek et al. (2016) (Tr 23), and Carraro et al. (2007) (Be 25). The column v_r lists the radial velocity; for the clusters with ages larger than 100 Myr see Jacobson et al. (2016, only UVES targets) excepted for M 67 (Casamiquela et al. 2016), NGC 2243 (Smiljanic et al. 2016); Friel et al. (2014) (NGC 4815), Harris (1996) (NGC 6752). For the young clusters, see Dias et al. (2002) (IC 2391, IC 2602, IC 4665, NGC 2264, NGC2451, NGC 2547, NGC 3293, NGC 6530), and Carraro et al. (2007) (Be 25). The column ‘# stars’ lists the number of stars in that particular field/cluster observed by the GES. The columns ‘DOE’ give the number of SB detected automatically, whereas the column ‘confirmed’ represents the number of SB kept after eye inspection of CCFs and associated spectra. The columns labeled ‘A’, ‘B’ and ‘C’ list the number of confirmed systems by confidence flag (probable, possible and tentative respectively). No SB2 or SB3 candidates have been found yet with the DOE code for the following clusters within the GES: Be 44 (93), M 15 (109), M 2 (110), NGC 104 (1138), NGC 1851 (127), NGC 1904 (113), NGC 2808 (112), NGC 362 (304), NGC 4372 (120), NGC 4833 (102) and NGC 5927 (124), where the numbers in parenthesis give the number of stars observed in each cluster.

component has a velocity close to that of the cluster, and the second velocity is offset. In that case, the SB2 nature is questionable and the star is more probably a pulsating star (responsible for the secondary peak or bump) belonging to the cluster (‘y’ in column ‘Member’). The list of individual radial velocities will be given in a forthcoming paper, based on iDR5 data. More extended remarks for each cluster are provided in Appendix C.

4.3. Orbital elements of two confirmed SB2 in clusters

With the data collected so far, we were able to confirm the binary nature of two SB2 candidates in clusters by deriving reliable orbital solutions for the systems 06404608+0949173 (NGC 2264 92) and 19013257-0027338 (Berkeley 81, written Be 81).

The first system 06404608+0949173 (magnitude $V \sim 12$) is a *bona fide* SB2 for which 24 spectra are available (20 GIRAFFE HR15N and 4 UVES U580), and an orbit can be computed, as shown on Fig. 19. Observations where only one velocity component is detected are not used to calculate the orbital solution

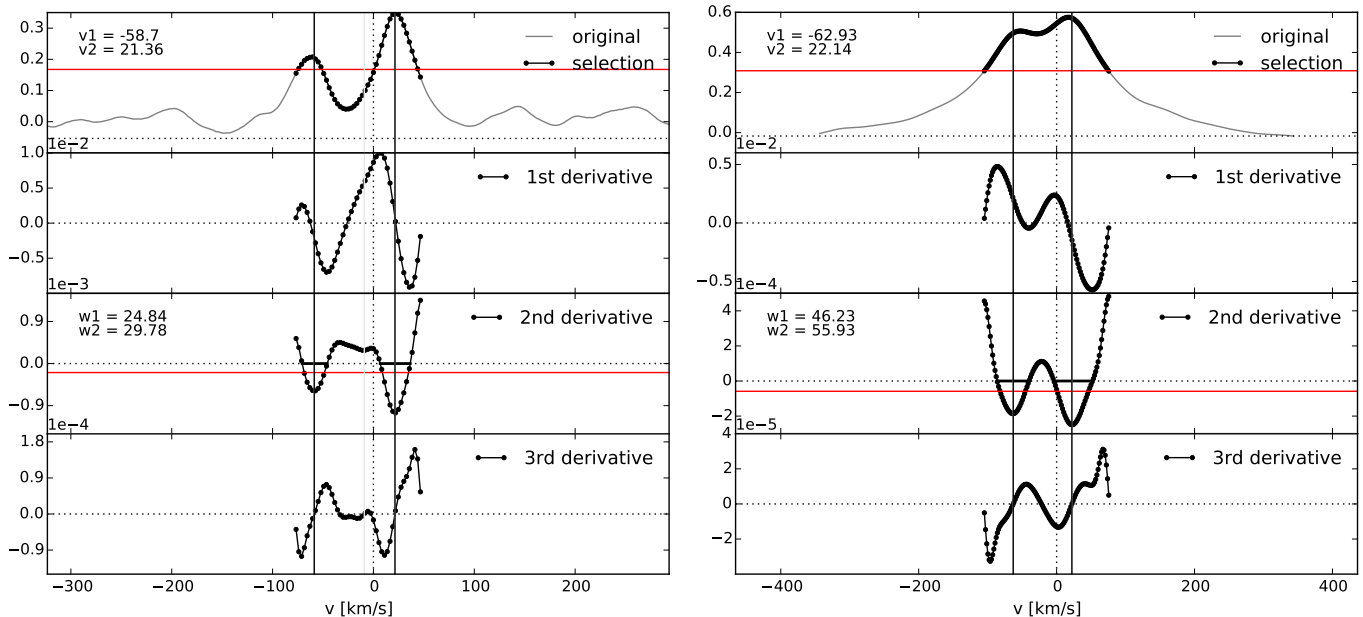


Fig. 17. Example of identification of a new SB2 candidate 02394731-0057248 not reported in Simbad. Left panel: GIRAFFE HR10 setup ($S/N \sim 10$). Right panel: GIRAFFE HR21 setup ($S/N \sim 140$).

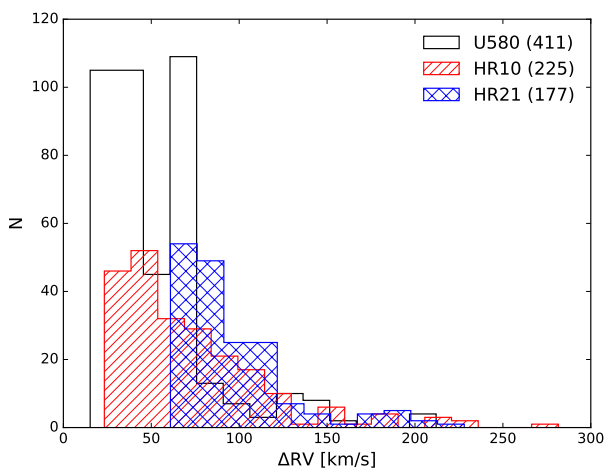


Fig. 18. Histograms of the radial velocity separation of SB2 candidates for GIRAFFE HR10, HR21 and for UVES U580 single exposures. The numbers in parenthesis are the numbers of single exposures where two peaks were identified.

because these velocities are not accurate (Fig. 19), since the two velocity components are blended. The orbital elements are listed in Table 4. The short period of 2.9637 ± 0.0002 d implies that neither of the components can be a giant which is consistent with the classification of the system as K0 IV (Walker 1956). The centre-of-mass velocity of the system (14.6 km s^{-1}) is close to the cluster velocity (17.7 km s^{-1}), as it should. The mass ratio is $M_B/M_A = 1.10$. Classified as FK Com in the GCVS (=V642 Mon), this source is chromospherically active with X-ray emission (ROSAT and XMM). This system thus adds to the two SB2 systems with available orbits (VSB 111 and VSB 126) already known in NGC 2264 (Karnath et al. 2013).

The second system 19013257-0027338 (magnitude $V \sim 17$) is a confirmed SB2 (2020 A) for which 18 spectra are available (8 GIRAFFE HR15N and 10 GIRAFFE HR9B). This source is

not listed in the Simbad database. The orbital elements are given in Table 4 and the orbit is displayed in Fig. 20. Strangely enough, a good SB2 solution for this system could only be obtained by adding an extra parameter to the orbital elements, namely an offset, between the systemic velocities derived from component A and from component B (see the ΔV_B term in Eq. (2) of Pourbaix & Boffin (2016)). In most cases, this offset is null but there could be situations where it is not, like in the presence of gravitational redshifts or convective blueshifts that are different for components A and B (Pourbaix & Boffin 2016). Alternatively, if the spectrum of one of the components forms in an expanding wind (as in a Wolf-Rayet star), it would lead as well to such an offset. However, what is puzzling in the considered case is the large value of the offset (24.8 ± 1.2) for which we could not find any convincing explanation. Indeed, no Wolf-Rayet stars are known in the Be 81 cluster according to the Simbad database. This very diffuse cluster of intermediate age lies towards the Galactic centre (Hayes & Friel 2014; Donati et al. 2014).

4.4. SB3 candidates

Tables 2 and 3 show that, in total, 11 SB3 candidates (7 probable: flag A, 1 possible: flag B, and 3 tentative: flag C) have been detected. Among those, five SB3 are found in the field (Fig. 21 and Table A.2) and six in clusters (Fig. 22 and within the Table C.1). A total of 266 targets were initially labeled as SB3 candidates by the DOE code while only 11 were kept after visual inspection, giving a success rate of about 4 % (compared to 30 % for SB2 detection). The SB3 candidates are essentially detected in UVES setups and in GIRAFFE setups HR9B and HR10. SB3 candidates in the stellar clusters have been examined on a case by case basis, and the results are reported below.

NGC 2451. The CCF of 07470917-3859003 exhibits three clear peaks (the CCF is classified as 2030A), at 25.0, 96.1, and 136.6 km s^{-1} . The first velocity is compatible with member-

Table 4. Orbital elements for 06404608+0949173 in NGC 2264, and 19013257-0027338 in Be 81.

CNAME	06404608+0949173	19013257-0027338
P (d)	2.9637 ± 0.0002	15.528 ± 0.002
e	0.092 ± 0.006	0.170 ± 0.006
ω ($^\circ$)	56.8 ± 3.9	265.7 ± 3.9
$T_0 - 2\,400\,000$ (d)	56072.4085 ± 0.0351	56470.531 ± 0.140
V_0 (km s $^{-1}$)	14.32 ± 0.55	34.51 ± 0.66
ΔV_B	0.00 (adopted)	24.8 ± 1.2
K_A (km s $^{-1}$)	106.3 ± 0.7	86.0 ± 0.9
K_B (km s $^{-1}$)	117.0 ± 0.6	97.0 ± 0.9
$\sigma_A(\text{O} - \text{C})$ (km s $^{-1}$)	20.2	6.1
$\sigma_B(\text{O} - \text{C})$ (km s $^{-1}$)	9.3	6.8
$a_A \sin i$ (Gm)	4.315 ± 0.030	18.1 ± 0.2
M_A/M_B	1.10	1.13
N	16	18

Notes. The orbital elements are the orbital period P , the eccentricity e , the argument of the periastron ω from the ascending node, the time of passage at periastron T_0 , the velocity of the centre-of-mass V_0 , the primary and secondary velocity amplitudes K_A and K_B , the projected primary semi-major axis on the plane of the sky $a_A \sin i$ and the primary to the secondary mass ratio M_A/M_B . $\sigma_A(\text{O} - \text{C})$ and $\sigma_B(\text{O} - \text{C})$ are the standard deviation of the residuals (observed – calculated) of components A and B. N is the number of available CCFs on which two velocity components are identified. For the meaning of ΔV_B see Eq. (2) of (Pourbaix & Boffin 2016).

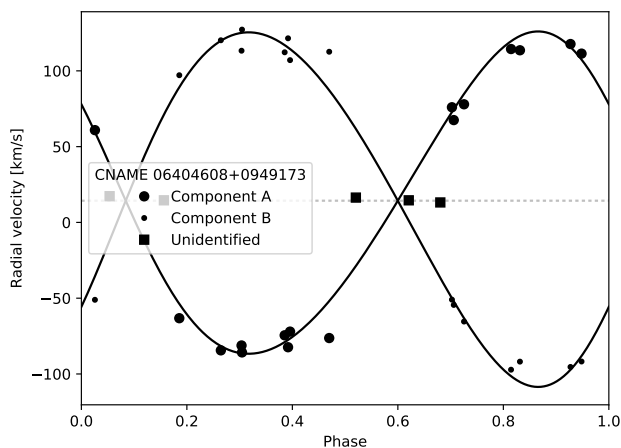


Fig. 19. The SB2 orbit of 06404608+0949173 in NGC 2264. Component A is represented by large circles and component B by small circles. Squares represent the single radial velocity obtained when only one peak is visible in the CCF; these are not used to calculate the orbital solution, due to their larger uncertainties. The error on radial velocities amounts to ± 0.25 km s $^{-1}$. Horizontal dotted line is V_0 .

ship in NGC 2451A. The DSS⁷ image reveals the presence of a slightly fainter star about 12'' south (a larger distance than the 1.2'' size of the fibre, so no contamination is possible). Given the fact that the two fainter peaks are not located symmetrically with respect to the cluster velocity, it is doubtful that the system could be an SB3 system in case of membership to NGC 2451.

NGC 2516. NGC 2516 45 (system 07575737-6044162) is a star classified as A2 V (Hartog 1976) with $V = 9.9$. The iDR4 recommended parameters ($T_{\text{eff}} = 8500$ K, $\log g = 4.1$ and solar metallicity) suggest that it could be a δ Scu star. Its CCF is most likely associated with a fast rotator with a superimposed

⁷ Digitized Sky Survey: https://archive.stsci.edu/cgi-bin/dss_form

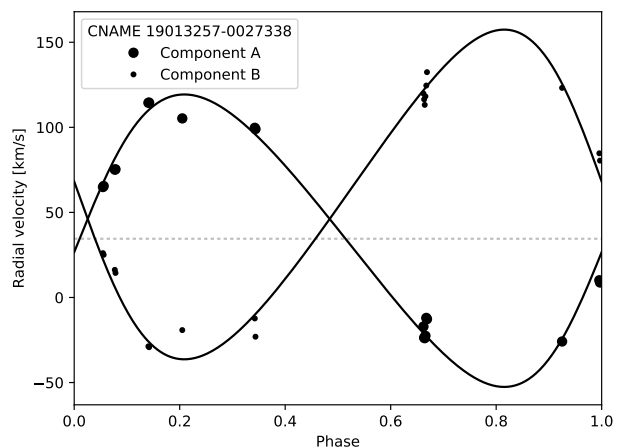


Fig. 20. The SB2 orbit of 19013257-0027338 in Berkeley 81. Component A is represented by large circles and component B by small circles. The error on radial velocities amounts to ± 0.25 km s $^{-1}$. Horizontal dotted line is V_0 .

sharper central peak. The SB3 nature of this candidate is therefore doubtful and a follow-up of this source should be performed before drawing any firm conclusion.

NGC 6705. In total, the DOE routine finds 52 SB3 candidates in NGC 6705, one of the largest number of SB3 among all the targeted clusters (Table 3). After a first-pass analysis we discarded all of them but one. NGC 6705 1147 (system 18510286-0615250). The velocities corresponding to the three peaks observed in the CCF are listed in Table 5. They exhibit clear temporal variations. The cluster velocity is 29.5 km s $^{-1}$ (Cantat-Gaudin et al. 2014). This velocity is close to that of the middle (C, *i.e.*, faintest) peak in the CCF. That central peak is not varying as much as the most extreme peaks, and moreover, the shape of the C peak is not as sharp as are the A and B peaks. Considering the fact that the cluster NGC 6705 is a dense one, we believe that this third peak is from background contamination. We therefore

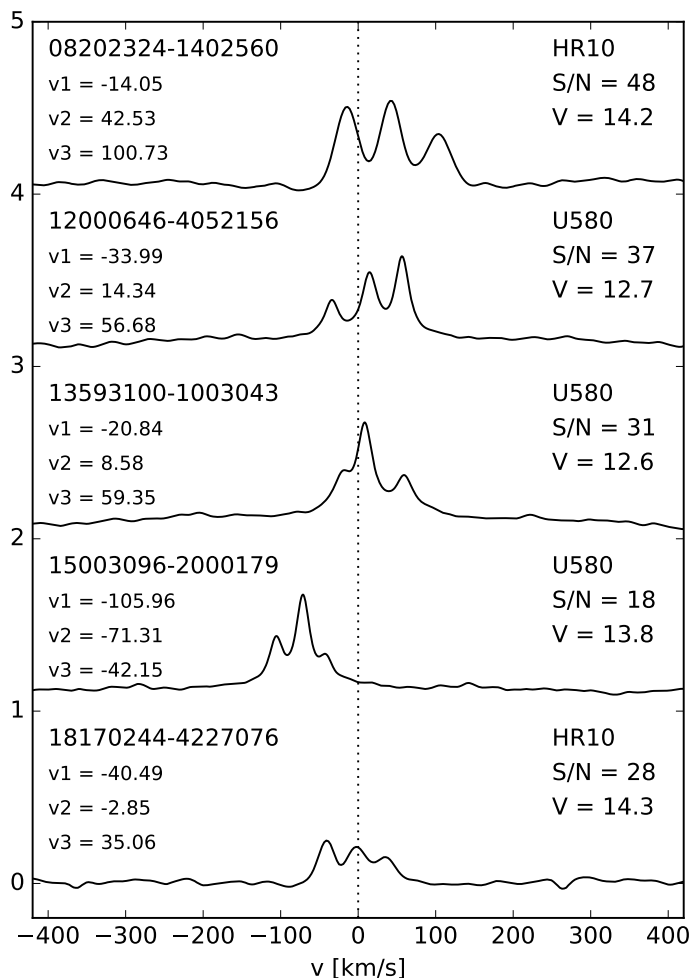


Fig. 21. The CCFs of the five SB3 candidates (flagged 2030 A) in the field. Velocities of the components are given in km s^{-1} .

conclude that the detection of NGC 6705 1147 as SB3 is spurious, and should be downgraded to SB2. The SB2 analysis is presented in Table 5 where we computed the mass ratio, adopting 34 km s^{-1} (Table 3) as the centre-of-mass (cluster) velocity. The observed velocity variations are consistent at all times with a mass ratio of the order of 1.32.

NGC 6005. The CCF of 15553867-5724434 (classified as 2030B) shows three peaks, at -81.6 , -14.4 and 32.7 km s^{-1} , to be compared with -25.2 km s^{-1} for the cluster velocity (Carlberg 2014). The spectra are at the minimum required S/N . These data are compatible with 15553867-5724434 being an SB3, member of NGC 6005.

NGC 6802. The CCF of 19302315+2013406 (classified as 2030C) shows three distinct peaks, at -22.4 , 22.0 and 65.5 km s^{-1} , to be compared with 12.4 km s^{-1} for the cluster velocity (Hayes & Friel 2014). These data are compatible with 19302315+2013406 being an SB3, member of NGC 6802.

Trumpler 20. The CCF of 12391904-6035311 (classified as 2030C) shows three distinct peaks, at -85.78 , -44.4 and 14.8 km s^{-1} , to be compared with -40.8 km s^{-1} for the cluster velocity (Kharchenko et al. 2005). These data are compatible with 12391904-6035311 being an SB3, member of Trumpler 20. An extended analysis of the GES data for this cluster may be found in Donati et al. (2014).

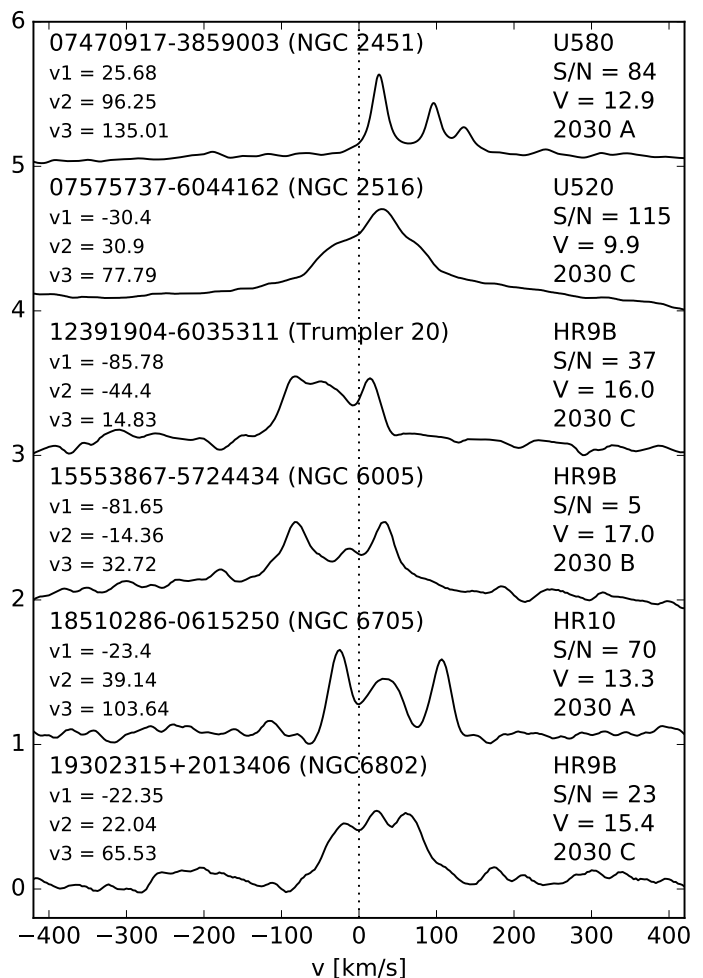


Fig. 22. The CCFs of the six SB3 candidates in the stellar clusters. Velocities of the components are given in km s^{-1} . The vertical scale of the CCFs has been magnified for clarity.

4.5. The unique SB4 candidate HD 74438

We have detected one SB4 candidate: the A2V star HD 74438 (CNAME 08414659-5303449, with $V = 7.58$) belonging to the open cluster IC 2391 (Platais et al. 2007).

The star has been observed 45 times within 2.5 h on February 18, 2014, with the U520 and U580 setups. Its peculiarity was already noticed by Platais et al. (2007), since it lies 0.9 mag above the main sequence in a color-magnitude diagram, and therefore was already suspected to be a triple system (since the maximum deviation for a binary system with two components of equal brightness would amount to $2.5 \times \log 2 = 0.75 \text{ mag}$). It is nevertheless considered a *bona fide* member of the cluster by Platais et al. (2007). Therefore, one may consider that the centre-of-mass velocity for the system is identical to the cluster velocity, namely $14.8 \pm 1 \text{ km s}^{-1}$ (Platais et al. 2007). A typical example of the CCF of HD 74438 is presented on Fig. 23, with its four distinct CCF peaks clearly apparent. The velocities of the peaks at different times over the night of February 18, 2014 are collected in Table 6. In this Table, we first notice that the velocities of components A and B (which correspond to the highest peaks) vary slowly and oppositely to each other. Their amplitude of variations is similar. If we compute the velocity variations with respect to the cluster velocity (which should correspond to the center-of-mass velocity of the AB pair, neglecting the gravitational influence of components C and D – columns $\Delta v_r(A)$ and

Table 5. Velocities of the three peaks (A, B, C) in the CCF of NGC 6705 1147. The columns labeled Δ list the differential velocity with respect to the centre-of-mass (*i.e.*, cluster) velocity, adopted as 34 km s^{-1} .

JD - 2 456 000	Setup	$v_r(A)$	$v_r(B)$	$v_r(C)$	$\Delta v_r(A)$	$\Delta v_r(B)$	M_A/M_B
77.409	HR3	79.62	-24.70	33.83	45.62	58.70	1.29
99.268	HR3	95.35	-47.33	29.87	61.35	81.33	1.33
99.280	HR5A	95.38	-45.73	23.68	61.38	79.73	1.30
99.295	HR6	93.65	-44.84	35.92	59.65	78.84	1.32
99.298	HR9B	94.83	-46.62	40.28	60.84	80.62	1.33
103.110	HR10	-26.78	106.91	39.14	60.78	72.91	1.20
442.394	HR10	75.38	-18.75	40.61	41.38	52.75	1.27
442.400	HR10	72.20	-20.23	26.72	38.20	54.23	1.42
442.406	HR10	75.41	-22.23	33.44	41.41	56.23	1.36

Table 6. Velocities of the four peaks (A, B, C, D) in the CCF of HD 74438 over the night of February 18, 2014 obtained with the U580 setup. The columns labeled Δ list the differential velocity with respect to the centre-of-mass (*i.e.*, cluster) velocity.

JD - 2 456 707	$v_r(A)$	$v_r(B)$	$v_r(C)$	$v_r(D)$	$\Delta v_r(A)$	$\Delta v_r(B)$	$\Delta v_r(C)$	$\Delta v_r(D)$	M_A/M_B	M_D/M_C
0.028	50.61	-21.40	-44.25	67.92	35.81	36.20	59.05	53.12	1.01	1.11
0.030	50.67	-21.14	-44.53	68.18	35.87	35.94	59.33	53.38	1.00	1.11
0.113	51.18	-22.18	-52.08	74.07	36.38	36.98	66.88	59.27	1.02	1.13
0.120	51.08	-22.40	-52.31	74.55	36.28	37.20	67.11	59.75	1.02	1.12

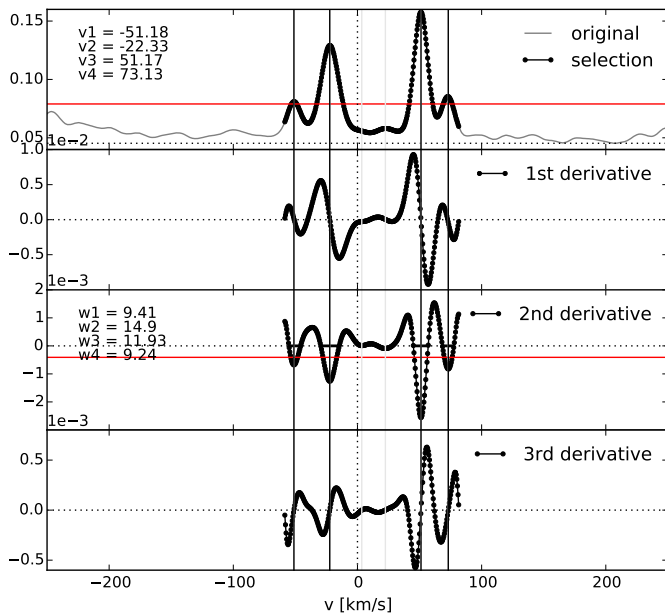


Fig. 23. The CCF of the A2V star HD 74438, obtained on JD 2456707.102 with the setup U580. The four peaks are clearly visible.

$\Delta v_r(B)$ in Table 6), we note that these variations obey a simple property: their ratio is almost constant. In a simple binary system, this property is expected since the ratio $\Delta v_r(B)/\Delta v_r(A)$ equals the mass ratio M_A/M_B . Here we find $M_A/M_B \sim 1.01$. Thus, the brightest components in the system, which correspond to the most prominent peaks A and B, are close to twins since their masses differ by 1% only. We observe that the pair CD obeys the same property: $\Delta v_r(C)/\Delta v_r(D)$ is almost constant, even though the amplitude of variations is larger than that of the AB pair. Again, assuming no perturbations from the AB pair, we get $M_D/M_C = \Delta v_r(C)/\Delta v_r(D) \sim 1.12$. It seems therefore that the observed variations do make sense and give credit for a physical nature of the ABCD system as a double pair AB/CD. We could nevertheless expect some perturbations of one pair on the other,

at least in the form of a trend of the center-of-mass velocities of each pair, if pair CD orbits around pair AB. The available observations do not span a time interval long enough to check that possibility.

Assuming that the ratio of the CCF amplitudes roughly scales with the luminosity ratio⁸, and adopting a ratio of 3 between the peak amplitudes of A and D (see Fig. 23), we get a magnitude difference between components A and D equal to $\Delta m = 2.5 \log 3 = 1.2 \text{ mag}$. Consequently, the observed visual magnitude $m_V = 7.58$ is mainly due to the pair AB. With the parallax of the system $\pi = 5.716 \pm 0.298 \text{ mas}$ provided by Gaia DR1 (Gaia Collaboration et al. 2016), the distance of this system is $175 \pm 9 \text{ pc}$. The absolute magnitude of AB pair is then $M_V(AB) = 1.36$. Assuming similar masses, we have $M_V(A) = M_V(B) = 2.12$. This corresponds to a spectral type A7 and to masses of $M_A = M_B = 1.8 M_\odot$ if on the main sequence (luminosity class V). The absolute magnitudes of the components C and D are consequently $M_V(C) = M_V(D) = 3.31$ corresponding to a spectral type F1 which correspond to a mass of about $1.5 M_\odot$. Inserting these values in the defining relation for the orbital velocity semi-amplitude (expressed in km s^{-1}):

$$K_i = 212.9 \left(\frac{M_i}{P(d)} \right)^{1/3} \frac{q}{(1+q)^{2/3}} \frac{\sin i}{(1-e^2)^{1/2}}, \quad (3)$$

it is possible to derive an upper limit to the orbital period. Indeed, for the AB pair, we adopt $e = 0$, $q = 1$, $M_A = 1.8 M_\odot$, and $K_A > 36 \text{ km s}^{-1}$ (Table 6), and obtain an upper limit on the orbital period of the AB pair, $P(d) < 93 \sin^3 i$. The same method applied on the CD pair (with $M_D = 1.5 M_\odot$, $e = 0$, $q = 1.1$, and $K_D > 60 \text{ km s}^{-1}$) yields $P(d) < 20 \sin^3 i$, in agreement with the fast variation observed in Table 6 for the C and D velocities.

An even more constraining limitation on the orbital period may be derived from the fast variations exhibited by the D component over the 2.2 h time span covered by the observations (Table 6). We first assume that 74.55 km s^{-1} corresponds to the maximum orbital velocity, from which we derive a semi-amplitude

⁸ If the spectral types of the components are very different, spectral mismatch may invalidate this hypothesis, but this is unlikely given the SB2 nature of the source which implies a luminosity ratio close to one and hence similar spectral types.

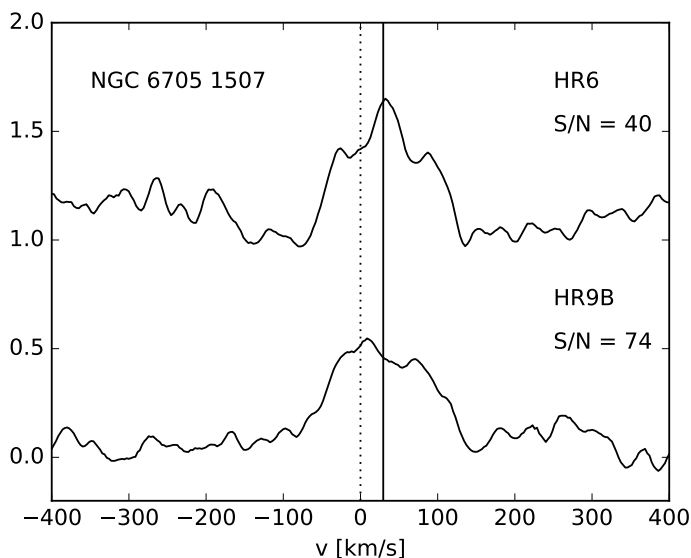


Fig. 24. The CCFs of star 1507 in the cluster NGC 6705, with its triple-peak CCF, most probably caused by pseudo-absorptions (caused by pulsation) superimposed on a rapid-rotator profile. The vertical plain line shows the cluster velocity.

$K_D = 59.75 \text{ km s}^{-1}$, corresponding to $\omega t_1 = \pi/2$. It is then possible to find $\omega = 2\pi/P$, and hence P , by assuming a sinusoidal velocity variation (in a circular orbit), reaching a velocity of 67.9 km s^{-1} at time $t_2 < t_1$, such that $\omega t_2 = \arcsin \frac{67.9-14.8}{K_D} = 1.093$. From this, we derive $\omega t_1 - \omega t_2 = \pi/2 - 1.093 = 0.477 = 2\pi/P \times (t_1 - t_2) = 2\pi/P \times 2.2 \text{ h}$, or $P = 29 \text{ h}$ as tentative period of the CD pair.

To conclude, we note that the above arguments allow us as well to estimate the deviation of HD 74438 in the color - magnitude diagram, for a system consisting of components with fluxes $F_A = F_B$, and $F_D = F_C = 1/3F_A$. The magnitude excess amounts to $2.5 \log(2 + 2/3) = 1.1 \text{ mag}$, not far from the 0.9 mag reported by Platais et al. (2007). The velocities of the components would definitely be worth monitoring over a few hundred days.

4.6. Multiplicity flagging by other GES working groups

It is worth mentioning that different nodes within the GES WGs have identified/detected spectroscopic systems for restricted subsamples of iDR4 data. Because we wanted to rely on a homogeneous detection process, we did not include the SBn detected by other WG in the present analysis. This detailed comparison will be performed for the next data release.

WG 12, focusing on pre-main sequence stars in clusters, detected 176 SB2 (A: 168, B:2, C: 6), one SB3 and two SB4. The intersection with our list amounts to 66. In particular, the two SB4 detected by WG12 are classified as SB2 in our final list; we re-checked that only two peaks are visible on the CCFs computed from single exposures. WG 12 developed a specific method to remove nebular contamination by masking the nebular lines in HR15N spectra for the clusters NGC 2264, NGC 6530 and Tr14. Indeed, these nebular lines can produce a double-peaked CCF that can be misclassified as an SB2 candidate; see Klutsch et al. (in prep.) for more details.

WG 13, dedicated to OBA-star spectrum analyses, identified about 30 SB2 in clusters (NGC 2547, NGC 3293, NGC 6705 and Tr 14). They detected one SB3 candidate (system 10344470-5805229 in NGC 3293) that we have rejected. Indeed, the three

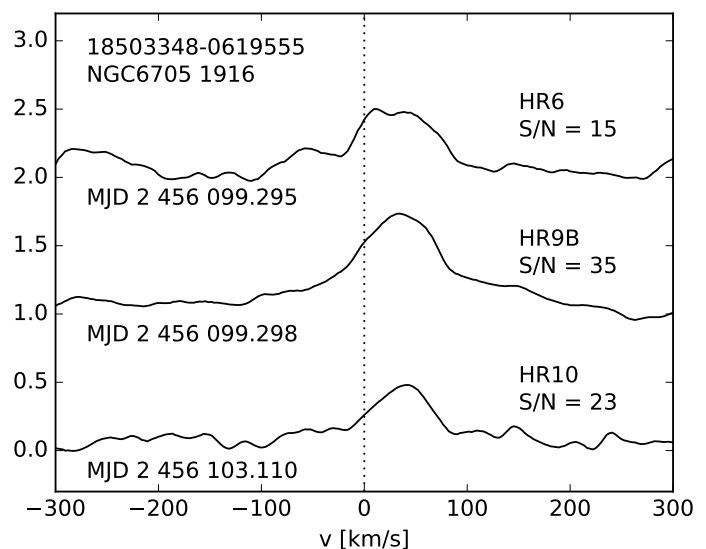


Fig. 25. Example of CCFs of a δ Scuti type star that can mimic an SB2 or even an SB3.

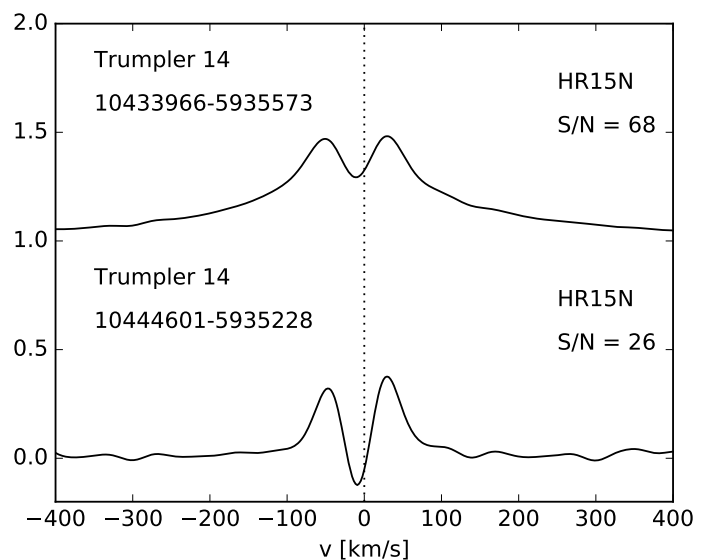


Fig. 26. Example of CCFs in HR15N that mimic SB2 but are due to emission in H α produced by nebular lines in the young cluster Trumpler 14.

peaks were detected by our method only in two CCFs and only in the HR5A setup, whereas 10 CCFs of the same object displayed only one or two peaks in various other setups (HR3, HR6, HR9B and HR14A). This SB3 detection was therefore considered as not reliable enough considering our rejection criteria (discussed at the beginning of Sect. 4). However, we did not even select this object as an SB2 because the velocity difference between the 2 peaks is too large ($> 290 \text{ km s}^{-1}$), indicating possible spurious peak(s).

In summary, the GES working groups, which are very focused, will inevitably reach higher detection rates for specific types of objects, but their methods do not apply to the whole GES survey. The method presented here, on the contrary, aims at providing homogeneous information for the whole survey, using all (GIRAFFE and UVES) individual spectra.

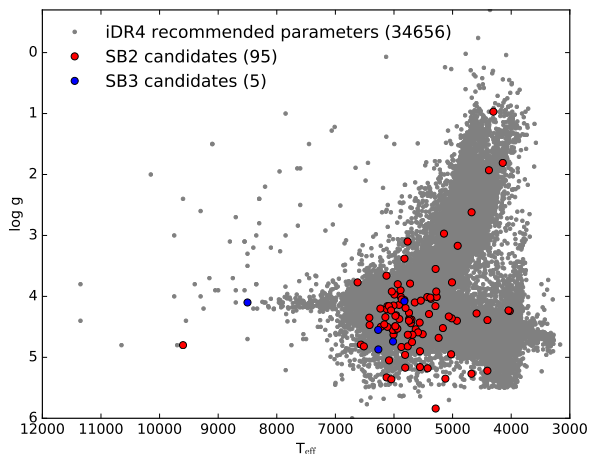


Fig. 27. $\log g - T_{\text{eff}}$ diagram of iDR4 stars with recommended atmospheric parameters. Among them the SB2 (red circles) and SB3 (blue circles) candidates are displayed.

4.7. Multiple peak CCFs unrelated to binarity

Double- and triple-component CCFs may sometimes be mimicked by physical processes unrelated to binarity. To clearly establish the binary nature of field stars, multiple observations covering a complete orbital cycle are mandatory in order to derive the orbital elements that fit best the radial velocities. In the case of stars belonging to associations and clusters containing hot and cold gas, the situation is worse: emission lines, which are not masked prior to the CCF computations, may produce troughs in the CCFs that could be interpreted as multiple peaks. Moreover, hot and pulsating stars like δ Sco stars, or young hot stars with discs, may also produce bumps in the CCFs. It is beyond the scope of the present paper to study the specific signatures of such processes on the CCFs, which also depend on the considered setup. However, we provide below some examples of multiple peak CCFs probably unrelated to binarity. Besides, in order to remove some spectral signatures degrading the CCFs (emission lines, very strong lines, etc.), we plan to recompute consistently all GIRAFFE and UVES CCFs in a forthcoming paper.

For instance, NGC 6705 1507 (system 18505296-0617402) is classified as A0 (Cantat-Gaudin et al. 2014) and shows three peaks in its CCF (originally classified as 2030C; Fig. 24) for the setting HR6, at -25.1 , 33.8 , and 86.9 km s^{-1} . The central, highest peak is close to the cluster velocity, and the other two are almost symmetrically located from the central peak, at ± 50 km s^{-1} . The very edge of the CCF has a steep slope which is reminiscent of a fast rotator. Indeed, the full base width of the CCF is about 180 km s^{-1} , a value typical for the rotation velocities of A stars. Moreover, a spectrum in the HR9B setting, taken on the same night, confirms the above analysis, which makes us conclude that the triple-peak CCF of star 1507 in the cluster NGC 6705 is most probably caused by pseudo-absorptions superimposed on a rapid-rotator profile. A similar situation is encountered for the 2 other SB3 candidates 18510403-0616023 and 18511155-0606094. These three objects have been discarded from the final list.

An example of a star automatically classified as an SB2 with flag C and very likely to be rather a δ Sco star, *i.e.* a hot rapid rotator with pulsation and no emission in $H\alpha$, is 18503348-0619555 (NGC 6705 1916, $V = 13.7$). This star has recommended parameters of $T_{\text{eff}} = 7821$ K and $\log g = 3.96$, compati-

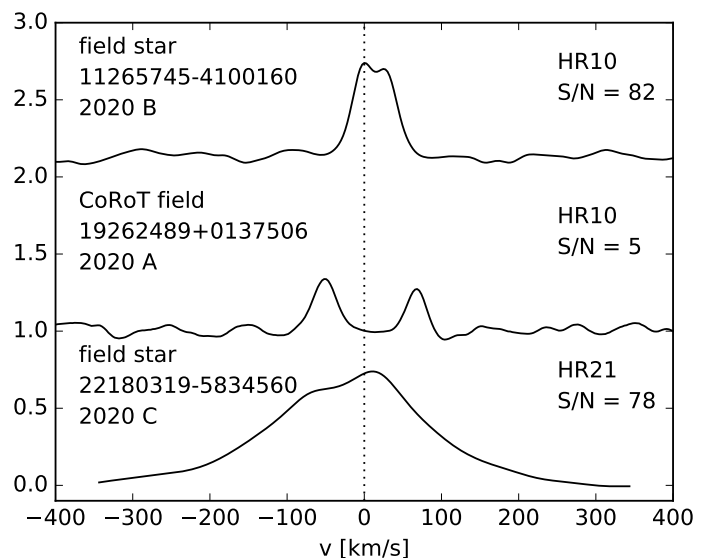


Fig. 28. Three giant SB2 candidates.

ble with a δ Sco-type star. The CCF in different setups at different epochs are shown on Fig. 25. The first CCF has 2 components (SB2), one broader than the other. The asymmetry of the second CCF could potentially lead the DOE code to identify 3 components (SB3). The last CCF is less ambiguous though it can be seen as an SB2 with close radial velocities. This SB2 candidate has been removed from the final list of SB n candidates.

In Trumpler 14, spectra are strongly contaminated by nebular lines around $H\alpha$. This may result from a reduction issue (inadequate sky subtraction in a nebular background). The nebular lines in emission, located at the cluster velocity, superimpose on the absorption lines of the star, also at the cluster velocity. Because the nebular lines in emission are narrower than the stellar ones in absorption, it results in a CCF with two clear peaks; sometimes the minimum between the two peaks gets even lower than the CCF continuum. Such false SB2 candidates could be unmasked (see Fig. 26 for the two examples 10433966-5935573 and 10444601-5935228) because in that cluster we found too many stars with radial velocities around -40 and 20 km s^{-1} , *i.e.* symmetrical with respect to the cluster velocity (~ -10 km s^{-1}). They can be explained by an emission at the cluster velocity obliterating the $H\alpha$ line resulting in a central absorption splitting the CCF (an emission line corresponds to absorption in the CCF.)

4.8. Distribution in the $(\log g, T_{\text{eff}})$ plane

The GES consortium provides recommended atmospheric parameters (T_{eff} , $\log g$ and $[\text{Fe}/\text{H}]$) for 63% of stars from the iDR4. They result from a delicate merging of atmospheric parameters obtained by different WGs using different methods, but all with the same model atmospheres and line lists. Among them, we identified a hundred of our confirmed SB n candidates, representing 30% of our detected SB n .

They are shown in the $\log g - T_{\text{eff}}$ plane (see Fig. 27). This figure reveals a sudden drop in the number of stars surveyed above 7000 K. This threshold corresponds to the transition between A and F stars, the latter being surveyed in a systematic way by the GES, the former being included only if they belong to specific clusters. For SB n , the atmospheric parameters provided by the GES pipeline are uncertain (or even wrong, as we show below) because (i) composite spectra cannot be fitted with

Table 7. List of the nine known SB2 systems confirmed by GES.

Name	GES field	CNAME	V	Catalogue	Reference
2MASS J06435849-0100515 CoRoT 102715243	CoRoT	06435847-0100516	13.05		Loeillet et al. (2008)
CD-52 2472, IC 2391 56	IC 2391	08385566-5257516	10.06	WEBDA	Mermilliod et al. (2009)
NGC 2682 117	M 67	08511868+1147026	12.59	SB9, WEBDA	Mathieu et al. (1990)
NGC 2682 119	M 67	08511901+1150056	12.53	SB9, WDS, WEBDA	Mathieu et al. (1990)
NGC 2682 ES 4004	M 67	08512291+1148493	12.69	SB9, WDS, WEBDA	Mathieu et al. (1990)
NGC 2682 165	M 67	08512940+1154139	12.83	WDS	Gavras et al. (2010)
PU Car	Cha I	11085326-7519374	12.17	WDS	Köhler et al. (2008)
2MASS J18505933-0622051	NGC 6705	18505933-0622051	17.06		Koo et al. (2007)
CoRoT 101129018	CoRoT	19263739+0152562	13.60		Cabrera et al. (2009)

Note:

SB9: Ninth catalogue of spectroscopic binary orbits (Pourbaix et al. 2004);

WDS: Washington visual Double Star catalogue (Mason et al. 2016);

WEBDA: A site Devoted to Stellar Clusters in the Galaxy and the Magellanic Clouds: <http://webda.physics.muni.cz>

single synthetic spectra, and (ii) spectra fitted by the automated pipelines are not the individual exposures but rather the stacked ones. Despite these shortcomings, the $\log g - T_{\text{eff}}$ diagram nevertheless allows us to identify systems of interest.

The two SB2 and SB3 systems on the warm end of the $\log g - T_{\text{eff}}$ diagram (with $T_{\text{eff}} > 8000$ K) are worth discussing. Their CNAMEs are 18280622+0642252 (NGC 6633 110, BD+06 3793, A3V), classified as 2020A, and 07575737-6044162 (NGC 2516 45, CD-60 1959, A2V), classified as 2030C.

The system 18280622+0642252 shows two peaks of equal heights at -70 km s^{-1} and 38 km s^{-1} . The former peak is particularly broad, and is probably associated with a rapidly rotating star. Since the cluster velocity (-25.4 km s^{-1}) lies in between the two peaks, and the double-peak CCF is very well-defined, we confirm the SB2 flag from the DOE routine.

The system 07575737-6044162 exhibits a broad CCF most likely associated with a fast rotator. It has a sharp central peak. It may perhaps be an SB2, but certainly not an SB3 (see Fig. 22).

The three giant SB2 candidates (19262489+0137506, 22180319-5834560 and 11265745-4100160) appearing in the $\log g - T_{\text{eff}}$ diagram (with $\log g < 2$) are surprising, since they should have a mass ratio very close to 1. Their CCFs are displayed on Fig. 28. To our knowledge, there are only few SB2 systems known so far involving two giant stars: (i) HD 172481 (more precisely an F2Ia post-AGB star and an M giant; (Reyniers & Van Winckel 2001; Jorissen et al. 2009); (ii) HD 187669 (a double-line eclipsing binary; Hełminiak et al. 2015a); (iii) TYC 6861-523-1 / ASAS J182510-2435.5 (Ratajczak et al. 2013); (iv) KIC 09246715 (a double-lined spectroscopic and eclipsing binary; Hełminiak et al. 2015b).

The system 19262489+0137506 (a CoRoT target with $T_{\text{eff}} = 4300$ K, $\log g = 1.0$), classified as 2020A, has indeed two peaks well separated by 117 km s^{-1} , of almost equal intensities, implying a rather short period for a pair of giants (Fig. 28, middle). Adopting $K = 117/2 \text{ km s}^{-1}$, $q = 1$, $\sin i = 1$, $e = 0$, and $M_1 = 1 M_{\odot}$, Eq. 3 predicts a period of the order of 7.5 d for the associated binary. This is rather short considering the giant nature of the two components. For instance, the minimum orbital period in the large sample of binaries with a K giant component in open clusters (Mermilliod et al. 2007) is just above 25 d. The situation is even worse for the sample of field M giants from Jorissen et al. (2009) where the shortest orbital period is above

200 d. This trend of course reflects the increase of the stellar radius along the giant branch. Independently, the spectral type of the system was estimated to be M2III from broad-band photometry (Exo-Dat, Deleuil et al. 2009). In any case, this system is worth a follow-up investigation, especially looking for signs of mass-transfer activity (like possible $H\alpha$ emission in its spectrum, but the 2 spectra available in HR15 are too noisy to see any such sign of activity).

The system 22180319-5834560, classified as 2020C (and $T_{\text{eff}} = 4100$ K, $\log g = 1.8$), exhibits a very broad CCF coming from the strong Ca II triplet in the HR21 setup, with two bumps responsible for the SB2 classification (Fig. 28, bottom). Observations in HR10 one day later does not show any sign of binarity. Inspection of the HR21 spectra reveals that the bumps observed in the CCF may be due to emission in the Ca II triplet line cores, making the SB nature doubtful.

The system 11265745-4100160 ($V = 13$), classified as 2020B (with $T_{\text{eff}} = 4400$ K, $\log g = 1.9$, top CCF of Figure 28), exhibits two close velocity components in HR10 (separated by about 32 km s^{-1}) but not visible in HR21. The validity of the atmospheric parameters may have been disturbed by the SB2 nature of the star.

4.9. Comparison with other catalogues

To estimate the proportion of new SB n candidates, we cross-checked our 352 distinct candidates with published on-line catalogues of stars. The intersection with the Simbad database (Wenger et al. 2000) provides 96 matches. Among them one is classified as double or multiple star (WDS J08513+1150, CNAME 08511901+1150056 belonging to M67), four as spectroscopic binary stars: 2MASS J06435849-0100515 (CNAME 06435847-0100516) in the Corot field, CD-52 2472 (CNAME 08385566-5257516) in the cluster IC2391, 2MASS J08512291+1148493 (CNAME 08512291+1148493) in M67 and NGC 2682 165 (CNAME 08512940+1154139) also in M67. Two are classified as eclipsing binary stars: 2MASS J18505933-0622051 (CNAME 18505933-0622051) in NGC 6705 and CoRoT 101129018 (CNAME 19263739+0152562). All these previously known binaries have been attributed by our DOE code a “A” confidence flag.

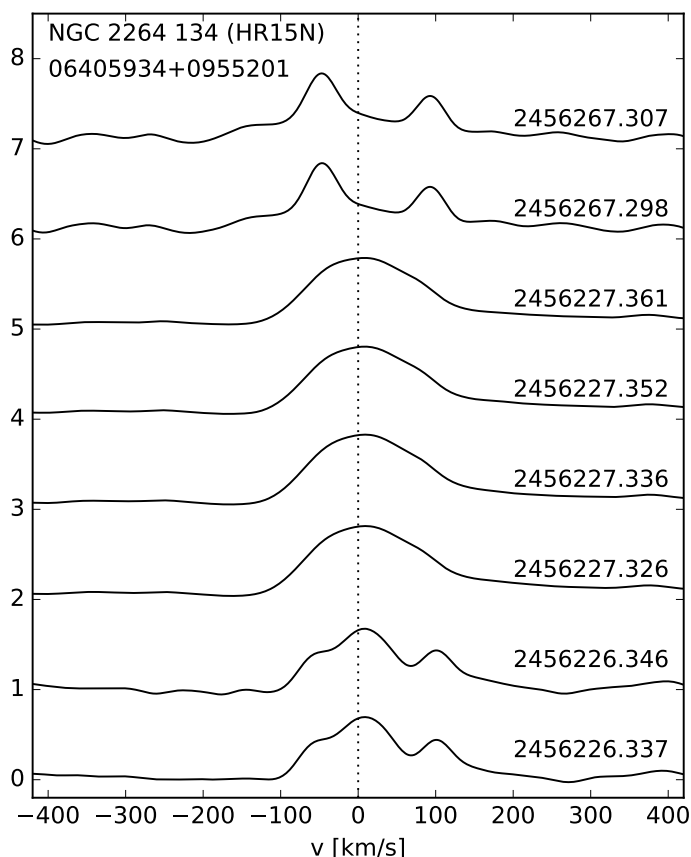


Fig. 29. iDR4 CCFs of the pre-main sequence star NGC 2264 134 (06405934+0955201). Known as SB2 in WEBDA, this star shows clear evidence to be an SB3 candidate.

We cross-matched our detections with various other catalogues, using the X-Match and the VizieR Search online tools from the CDS⁹ by uploading the J2000 coordinates built from the CNAME of our SB candidates. For each catalogue, we set the matching area within a radius of 3 arcsec.

The comparison with the *Ninth Catalogue of Spectroscopic Binary Orbits* (Pourbaix et al. 2004, SB9) leads to three systems in common, namely 08511868+1147026, 08511901+1150056, and 08512291+1148493, which are members of the M67 cluster (NGC 2682) with a visual magnitude of about 12.5.

The comparison with the *Washington visual Double Star catalogue* (WDS, Mason et al. 2016) leads to an intersection of two systems, namely WDS J08513+1150 in M 67 and WDS J11088-7519 in Cha I (CNAME 08511901+1150056 and 11085326-7519374 respectively).

Cross-matches with the Geneva-Copenhagen Survey of the solar neighborhood III (Holmberg et al. 2009), with the bibliographic catalogue of stellar radial velocities (Malaroda et al. 2006), with the RAVE catalogue of SB2 candidates (Matijević et al. 2010) and with the Multiple Star Catalogue (MSC) (Tokovinin 1997) resulted in empty intersections. We stress that the limiting magnitudes of all these catalogues are much brighter than that of the GES ($V \sim 19$), therefore we expected a small intersection.

As far as the WEBDA cluster database is concerned, four of our SB n candidates are known in WEBDA, with available orbital parameters (see Table 7). We also found that two SB2

⁹ <http://cdsxmatch.u-strasbg.fr/xmatch>,
<http://vizier.u-strasbg.fr>

known in WEBDA are observed in iDR4 but were discarded by the workflow. M67 111 has been observed (08511799+1145541) but the second peak is too low to be automatically detected. The same issue occurs with NGC 2264 134 (06405934+0955201), known to be an SB2 in WEBDA and known to be a pre-main sequence star. It has been observed eight times and seems to be an SB3 candidate because four CCFs have one peak, two CCFs have two peaks and two CCFs have three peaks (see Fig. 29).

For the sake of completeness, we also checked whether the DOE algorithm did retrieve the known SB n candidates from the Geneva-Copenhagen Survey and from SB9. It turns out that only one SB2 (08511799+1145541 in M67) present in SB9 was not found by DOE. The reason thereof is the following: 10 observations in U580 were performed but the second peak is only visible and detected in two of them. Because only stars with more than 75% of multiple peaks detection in a given setup were flagged as SB2 candidates, 08511799+1145541 was rejected. This shows that the 75% criterion, chosen to be conservative, might be too restrictive in some cases, although it prevents many false positive detections.

Previously known SB2 systems flagged as such by the GES are listed in Table 7. We stress the fact that the analysis of the GES data provides a substantial number of new SB2 and SB3 candidates because SB detection was performed on a huge data sample ($\sim 50\,000$ stars) characterized by a faint limiting magnitude with respect to previous surveys. The new SB2, SB3 and SB4 candidates clearly deserve more observations in order to derive their orbital elements.

5. Conclusion

We present a method aiming at identifying multiple-lined spectroscopic binaries (SB n , $n \geq 2$) based on the successive derivatives of the CCFs. A list of SB n among the GES iDR4, both in the Galactic field and in the stellar clusters, is presented. In addition, orbital solutions for binary systems belonging to the open clusters NGC 2264 and Be 81 have been calculated.

The detection method has been tested on all the setups of the GIRAFFE and UVES spectrographs available within the GES. It turns out that UVES U580 and GIRAFFE HR10 are the most appropriate setups to detect multiplicity with velocity differences as low as 15 km s^{-1} and 23 km s^{-1} , respectively. Simulations show that the DOE algorithm reliably derives radial velocities (with a formal error of the order of 0.20 km s^{-1} at a typical S/N of 10 for GIRAFFE and lower than 0.01 km s^{-1} at $S/N = 50$ for UVES setups; for multi-component CCFs, the formal error will be slightly increased and, in addition, the systematic error may reach a few km s^{-1} at the detection limit).

The detection method leads to a number of false positive detections in stellar clusters. Using physical properties of the clusters and combining information from the spectra and CCFs of different setups, we discussed and discarded a fraction of candidates. A confusing SB2-like signature could be imprinted to the CCF by pulsations in δ Scuti variable stars, by H α emission in circumstellar discs or interstellar absorption by cold clouds along the line of sight. In such cases, spurious peaks or bumps appear in the CCF.

We discovered 340 SB2, 11 SB3 and one SB4 out of 51 000 stars with more than 205 000 single exposures. The most confident binary candidates ('A' flag) most often show very clear composite spectra. Incidentally, we warn against the use of the GES recommended atmospheric parameters for these SB n candidates. Indeed, one third of SB n candidates do have GES recommended

parameters, but the the presence of multiple components in spectral lines can potentially lead to erroneous parameters.

The frequency of SB n ($n \geq 2$) found by our method in the GES iDR4 sample is 0.7 %. Most of the SB n candidates are new because they belong to a sample of stars much fainter than what was covered by previous catalogues. If we extrapolate this percentage of 0.7% SB n binaries to the final GES pool of 10^5 stars, we expect to reach about 1 000 new SB n systems in the upcoming data releases because the number of observed stars will increase by a factor of two and because we plan to further fine-tune our detection criteria. Indeed the aim of the present analysis was to detect binaries, minimizing the number of “false positive” detections (*i.e.* stars wrongly classified as SB n). The method presented in this paper can be readily applied to the ESA *Gaia* mission spectra.

Acknowledgements. T.M., M.V.d.S. and S.v.E. are supported by a grant from the Fondation ULB. This work has been partly funded by an *Action de recherche concertée* (ARC) from the *Direction générale de l’Enseignement non obligatoire et de la Recherche scientifique – Direction de la recherche scientifique – Communauté française de Belgique*. T.M. is supported by the FNRS-F.R.S. as temporary post-doctoral researcher under grant n° 2.4513.11. This work was supported by the Fonds de la Recherche Scientifique FNRS under Grant n° T.0198.13. C.A. acknowledges to the Spanish grant AYA2015-63588-P within the European Funds for Regional Development (FEDER). M.T.C. acknowledge the financial support from the Spanish Ministerio de Economía y Competitividad, through grant AYA2013-40611-P. R.S. acknowledges support from the Polish Ministry of Science and Higher Education. This work was partly supported by the European Union FP7 programme through ERC grant number 320360 and by the Leverhulme Trust through grant RPG-2012-541. We acknowledge the support from INAF and Ministero dell’ Istruzione, dell’ Università e della Ricerca (MIUR) in the form of the grant “Premiale VLT 2012”. The results presented here benefit from discussions held during the *Gaia*-ESO workshops and conferences supported by the ESF (European Science Foundation) through the GREAT Research Network Programme. This research has made use of the Washington Double Star Catalogue maintained at the U.S. Naval Observatory. This research has made use of the WEBDA database, operated at the Department of Theoretical Physics and Astrophysics of the Masaryk University. This research has made use of the SIMBAD database, operated at CDS, Strasbourg, France. This research has made use of Python, in particular the Python module `pyfits.py` which is a product of the Space Telescope Science Institute, which is operated by AURA for NASA. This research has made use of the Digitized Sky Surveys which were produced at the Space Telescope Science Institute under U.S. Government grant NAG W-2166. The images of these surveys are based on photographic data obtained using the Oschin Schmidt Telescope on Palomar Mountain and the UK Schmidt Telescope. The plates were processed into the present compressed digital form with the permission of these institutions. This work has made use of data from the European Space Agency (ESA) mission *Gaia* (<https://www.cosmos.esa.int/gaia>), processed by the *Gaia* Data Processing and Analysis Consortium (DPAC, <https://www.cosmos.esa.int/web/gaia/dpac/consortium>). Funding for the DPAC has been provided by national institutions, in particular the institutions participating in the *Gaia* Multi-lateral Agreement. The authors thank the referee for his comments which helped improving the manuscript.

References

Bellini, A., Bedin, L. R., Pichardo, B., et al. 2010, *A&A*, 513, A51
 Bragaglia, A. 2012, in *Science from the Next Generation Imaging and Spectroscopic Surveys*, P3
 Bragaglia, A. & Tosi, M. 2006, *AJ*, 131, 1544
 Cabrera, J., Fridlund, M., Ollivier, M., et al. 2009, *A&A*, 506, 501
 Cantat-Gaudin, T., Vallenari, A., Zaggia, S., et al. 2014, *A&A*, 569, A17
 Carlberg, J. K. 2014, *AJ*, 147, 138
 Carraro, G., Geisler, D., Villanova, S., Frinchaboy, P. M., & Majewski, S. R. 2007, *A&A*, 476, 217
 Casamiquela, L., Carrera, R., Jordi, C., et al. 2016, *MNRAS*, 458, 3150
 Castelli, F. & Kurucz, R. L. 2003, in *IAU Symposium*, Vol. 210, *Modelling of Stellar Atmospheres*, ed. N. Piskunov, W. W. Weiss, & D. F. Gray, A20
 Damiani, F., Bonito, R., Magrini, L., et al. 2016, *A&A*, 591, A74
 de Laverny, P., Recio-Blanco, A., Worley, C. C., & Plez, B. 2012, *A&A*, 544, A126
 Deleuil, M., Meunier, J. C., Moutou, C., et al. 2009, *AJ*, 138, 649
 Delgado, A. J., Alfaro, E. J., & Yun, J. L. 2007, *A&A*, 467, 1397

Dias, W. S., Alessi, B. S., Moitinho, A., & Lépine, J. R. D. 2002, *A&A*, 389, 871
 Donati, P., Cantat Gaudin, T., Bragaglia, A., et al. 2014, *A&A*, 561, A94
 Duchêne, G. & Kraus, A. 2013, *ARA&A*, 51, 269
 Fernandez, M. A., Covey, K. R., De Lee, N., et al. 2017, *ArXiv e-prints*
 Fűrész, G., Hartmann, L. W., Szentgyorgyi, A. H., et al. 2006, *ApJ*, 648, 1090
 Foster, D. 2013, in *Shape in Picture: Mathematical Description of Shape in Grey-Level Images*, ed. Y. L. O, A. Toet, D. Foster, H. Heijmans, & P. Meer (Springer)
 Frankowski, A., Jancart, S., & Jorissen, A. 2007, *A&A*, 464, 377
 Friel, E. D., Donati, P., Bragaglia, A., et al. 2014, *A&A*, 563, A117
 Gaia Collaboration, Brown, A. G. A., Vallenari, A., et al. 2016, *A&A*, 595, A2
 Gao, S., Liu, C., Zhang, X., et al. 2014, *ApJ*, 788, L37
 Gavras, P., Sinachopoulos, D., Le Campion, J. F., & Ducourant, C. 2010, *A&A*, 521, A4
 Gilmore, G., Randich, S., Asplund, M., et al. 2012, *The Messenger*, 147, 25
 Gustafsson, B., Edvardsson, B., Eriksson, K., et al. 2008, *A&A*, 486, 951
 Harris, W. E. 1996, *AJ*, 112, 1487
 Hartoog, M. R. 1976, *ApJ*, 205, 807
 Hayes, C. R. & Friel, E. D. 2014, *AJ*, 147, 69
 Heiter, U., Jofré, P., Gustafsson, B., et al. 2015a, *A&A*, 582, A49
 Heiter, U., Lind, K., Asplund, M., et al. 2015b, *Phys. Scr.*, 90, 054010
 Hełminiak, K. G., Graczyk, D., Konacki, M., et al. 2015a, *MNRAS*, 448, 1945
 Hełminiak, K. G., Ukita, N., Kambe, E., & Konacki, M. 2015b, *ApJ*, 813, L25
 Holmberg, J., Nordström, B., & Andersen, J. 2009, *A&A*, 501, 941
 Jackson, R. J., Jeffries, R. D., Lewis, J., et al. 2015, *A&A*, 580, A75
 Jacobson, H. R., Friel, E. D., Jílková, L., et al. 2016, *A&A*, 591, A37
 Jones, E., Oliphant, T., Peterson, P., et al. 2001, *SciPy: Open source scientific tools for Python*, [Online; accessed <today>]
 Jorissen, A., Frankowski, A., Famaey, B., & van Eck, S. 2009, *A&A*, 498, 489
 Karnath, N., Prato, L., Wasserman, L. H., et al. 2013, *AJ*, 146, 149
 Kharchenko, N. V., Piskunov, A. E., Röser, S., Schilbach, E., & Scholz, R.-D. 2005, *A&A*, 438, 1163
 Köhler, R., Ratzka, T., Herbst, T. M., & Kasper, M. 2008, *A&A*, 482, 929
 Koo, J.-R., Kim, S.-L., Rey, S.-C., et al. 2007, *PASP*, 119, 1233
 Kurucz, R. 1993, *SYNTHES Spectrum Synthesis Programs and Line Data*. Kurucz CD-ROM No. 18. Cambridge, Mass.: Smithsonian Astrophysical Observatory, 1993., 18
 Loeillet, B., Bouchy, F., Deleuil, M., et al. 2008, *A&A*, 479, 865
 Luo, A.-L., Zhao, Y.-H., Zhao, G., et al. 2015, *Research in Astronomy and Astrophysics*, 15, 1095
 Majewski, S. R., Schiavon, R. P., Frinchaboy, P. M., et al. 2015, *ArXiv e-prints*
 Malaroda, S., Levato, H., & Galliani, S. 2006, *VizieR Online Data Catalog*, 3249
 Mason, B. D., Wycoff, G. L., Hartkopf, W. I., Douglass, G. G., & Worley, C. E. 2016, *VizieR Online Data Catalog*, 1
 Mathieu, R. D., Latham, D. W., & Griffin, R. F. 1990, *AJ*, 100, 1859
 Matijević, G., Zwitter, T., Bienaymé, O., et al. 2011, *AJ*, 141, 200
 Matijević, G., Zwitter, T., Munari, U., et al. 2010, *AJ*, 140, 184
 Mermilliod, J.-C., Andersen, J., Latham, D. W., & Mayor, M. 2007, *A&A*, 473, 829
 Mermilliod, J.-C., Mayor, M., & Udry, S. 2009, *A&A*, 498, 949
 Moni Bidin, C., Moehler, S., Piotto, G., et al. 2006, *A&A*, 451, 499
 Munari, U., Sordo, R., Castelli, F., & Zwitter, T. 2005, *A&A*, 442, 1127
 Nordström, B., Mayor, M., Andersen, J., et al. 2004, *A&A*, 418, 989
 Overbeek, J. C., Friel, E. D., Donati, P., et al. 2016, *ArXiv e-prints*
 Pancino, E., Lardo, C., Altavilla, G., et al. 2017, *A&A*, 598, A5
 Platais, I., Melo, C., Mermilliod, J.-C., et al. 2007, *ã*, 461, 509
 Plez, B. 2012, *Turbospectrum: Code for spectral synthesis*, *Astrophysics Source Code Library*
 Pourbaix, D. 2000, *A&AS*, 145, 215
 Pourbaix, D. & Boffin, H. M. J. 2016, *A&A*, 586, A90
 Pourbaix, D., Tokovinin, A. A., Batten, A. H., et al. 2004, *A&A*, 424, 727
 Prisinzano, L., Damiani, F., Micela, G., et al. 2016, *A&A*, 589, A70
 Raghavan, D., McAlister, H. A., Henry, T. J., et al. 2010, *ApJS*, 190, 1
 Randich, S., Gilmore, G., & Gaia-ESO Consortium. 2013, *The Messenger*, 154, 47
 Ratajczak, M., Hełminiak, K. G., Konacki, M., & Jordán, A. 2013, *MNRAS*, 433, 2357
 Rebull, L. M., Makidon, R. B., Strom, S. E., et al. 2002, *AJ*, 123, 1528
 Reyniers, M. & Van Winckel, H. 2001, *A&A*, 365, 465
 Rigliaco, E., Wilking, B., Meyer, M. R., et al. 2016, *A&A*, 588, A123
 Sacco, G. G., Morbidelli, L., Franciosini, E., et al. 2014, *A&A*, 565, A113
 Sacco, G. G., Spina, L., Randich, S., et al. 2017, *A&A*, 601, A97
 Smiljanic, R., Romano, D., Bragaglia, A., et al. 2016, *A&A*, 589, A115
 Sousa, S. G., Santos, N. C., Israelian, G., Mayor, M., & Monteiro, M. J. P. F. G. 2007, *A&A*, 469, 783
 Stonkutė, E., Koposov, S. E., Howes, L. M., et al. 2016, *MNRAS*, 460, 1131
 Sung, H., Bessell, M. S., Lee, B.-W., & Lee, S.-G. 2002, *AJ*, 123, 290
 Tokovinin, A. A. 1997, *A&AS*, 124
 Troup, N. W., Nidever, D. L., De Lee, N., et al. 2016, *AJ*, 151, 85
 VandenBerg, D. A., Brogaard, K., Leaman, R., & Casagrande, L. 2013, *ApJ*, 775, 134
 Walker, M. F. 1956, *ApJS*, 2, 365
 Wenger, M., Ochsenbein, F., Egret, D., et al. 2000, *A&AS*, 143, 9
 Wilkinson, M. I., Vallenari, A., Turon, C., et al. 2005, *MNRAS*, 359, 1306

Appendix A: SB2 and SB3 candidates in the field

Table A.1. List of SB2 candidates in the field ordered by right ascension.

CNAME	flag	# exp.	# sp.	setup	MJD	$v_r(1)$	$v_r(2)$	V
00040663-0101512	2020B	6	6	HR21	56205.162	-65.45	66.95	16.10
00195847-5423227	2020A	4	4	HR10	56532.287	93.29	153.47	14.20
00202300-5436167	2020A	4	4	HR10	56532.308	285.74	330.48	15.30
00301156-5001500	2020A	2	4	U580	56266.085	17.67	47.52	13.90
00301724-0334401	2020C	4	4	HR21	56468.397	-48.62	24.97	15.40
00324599-4354509	2020B	4	8	U580	56198.130	-5.84	15.63	12.90
00503283-4955302	2020A	4	4	HR10	56268.134	-21.03	32.27	14.90
00591557-0105576	2020B	4	4	HR21	56204.172	18.82	130.23	14.80
01000070-0100143	2020C	4	4	HR21	56204.172	-97.34	-33.48	14.50
01012693-5420463	2020C	4	4	HR21	56530.337	-92.63	-23.25	15.30
01194076-0047374	2020C	4	4	HR21	56204.266	-22.60	68.63	15.20
01200304-5435209	2020B	4	4	HR21	56552.310	-10.28	80.61	15.60
01202092-0102102	2020C	4	4	HR21	56204.284	-56.79	16.26	15.80
01300825-5009146	2020A	4	4	HR10	56580.192	-16.04	74.55	13.50
01390790-5403014	2020A	4	4	HR10	56548.390	40.40	83.81	14.20
01393831-4648457	2020B	4	4	HR10	56197.248	24.46	60.55	13.50
01405323-5356575	2020B	4	4	HR10	56548.390	12.59	51.88	13.10
01585747-5401493	2020B	4	4	HR21	56580.217	-65.75	40.52	14.00
01592290-4658510	2020C	4	8	U580	56207.122	5.97	26.76	12.80
02000945-5352567	2020A	4	4	HR10	56579.297	-7.69	54.71	14.00
02002707-4655438	2020B	4	4	HR10	56207.144	36.62	73.89	14.10
02003583-0053539	2020C	4	4	HR21	56224.275	-62.19	111.35	13.50
02005449-0055403	2020A	4	4	HR10	56223.207	-23.45	24.67	15.00
02105686-5012361	2020C	4	4	HR21	56531.288	-20.25	86.83	16.00
02194365-0104381	2020C	5	5	HR21	56532.333	-23.84	42.38	15.00
02290765-0318506	2020B	4	4	HR21	56226.222	6.73	81.89	15.70
02290959-5004269	2020A	4	4	HR10	56578.216	13.53	94.34	14.50
02302503-4956149	2020A	4	4	HR10	56578.216	-11.88	72.23	14.30
02394731-0057248	2020A	4	4	HR10 HR21	56172.267	-58.70	21.36	13.80
02503269-5010152	2020C	4	4	HR21	56576.204	-58.59	15.40	15.70
03103980-5007403	2020B	6	6	HR10	56310.061	-15.11	41.25	15.90
03175192-0034528	2020B	4	4	HR10	56225.186	37.94	64.65	14.70
03175934-0024337	2020C	4	4	HR21	56226.132	-9.62	86.60	15.10
03181102-0034546	2020A	4	4	HR10	56225.186	-113.51	0.00	14.00
03200828-4656379	2020B	4	4	HR10	56197.296	-2.25	40.37	14.90
03201610-5601321	2020B	4	8	U580	56580.261	-7.88	21.61	13.50
03374095-2723284	2020A	4	4	HR10	56208.238	67.49	115.44	15.60
03381845-2722333	2020A	4	4	HR10 HR21	56208.238	-46.86	98.89	12.90
03394566-4710178	2020B	4	4	HR10	56207.312	288.73	337.53	16.30
03401027+0002559	2020A	4	8	U580	56195.354	-35.88	29.38	13.30
03592788-4650482	2020C	4	4	HR10	56194.274	39.19	75.96	15.10
03595053-4701073	2020A	4	4	HR10	56194.274	-90.52	27.62	14.50
04202910-0019338	2020A	4	8	U580	55998.026	-50.58	100.14	11.90
04301327-5001191	2020A	6	12	U580	56264.244	118.87	167.53	13.10
04404692-4609391	2020A	4	4	HR10 HR21	56577.238	59.05	141.04	15.30
04410121-5004008	2020A	4	4	HR10	56223.304	-16.92	51.75	14.10
04434718-0040232	2020B	4	4	HR10 HR21	56551.345	98.00	136.04	14.40
05291006-6028494	2020B	4	4	HR21	56709.111	-21.19	71.29	13.20
05294654-6025081	2020A	4	4	HR10	56709.019	32.19	75.21	15.10
05313822-6021421	2020A	4	4	HR10	56709.019	57.18	116.23	16.00
05402480-4726342	2020B	4	8	U580	56711.024	50.09	71.43	12.50
05403344-4738199	2020B	4	4	HR10	56711.113	75.79	118.51	15.80
05554481-6034418	2020C	4	4	HR21	56606.315	3.28	110.72	14.70
05562593-6029184	2020A	4	8	U580	56606.315	-12.42	34.22	13.10
07554475-0908077	2020A	4	4	HR10	56001.042	79.69	125.36	14.90
07555317-0848462	2020C	4	4	HR21	56000.076	47.50	119.55	15.10
07593692-0025252	2020A	8	8	HR10 HR21	55974.132	-12.32	51.48	14.40

Table A.1. Continued.

CNAME	flag	# exp.	# sp.	setup	MJD	$v_r(1)$	$v_r(2)$	V
08191969-1412025	2020B	4	4	HR10	56758.012	47.82	83.86	14.00
08194766-1411293	2020B	4	4	HR10	56758.012	15.96	48.53	16.00
08231542-0535165	2020B	4	8	U580	56314.137	-5.39	11.91	12.90
08231783-0523549	2020C	4	4	HR21	56341.085	-33.50	31.74	16.40
08233762-0536506	2020A	4	8	U580	56314.137	12.10	44.00	13.10
08395189-0756213	2020B	4	4	HR10	56378.103	-21.55	15.86	15.10
08395720-0756505	2020C	4	4	HR10	56378.103	73.20	104.50	13.50
08403017-1409445	2020A	4	4	HR10	56678.207	50.72	91.12	14.40
08582336-1403021	2020B	4	4	HR10	56679.175	68.05	98.08	16.60
09193694-1751496	2020B	4	4	HR10	56706.273	37.38	82.60	14.40
09382162-1758544	2020C	4	4	HR21	56708.237	64.53	133.81	14.70
09391804-1755456	2020B	4	4	HR21	56708.237	-26.58	93.47	16.60
09393263-0505599	2020B	5	5	HR10	56793.997	-33.37	20.06	14.90
09594300-4054056	2020B	4	4	HR10	55928.261	57.16	84.96	13.90
09594650-4059014	2020A	4	4	HR10 HR21	55928.261	-43.94	45.55	14.20
10004160-4053496	2020A	4	4	HR10	55928.282	-56.40	0.72	13.80
10075849-0753079	2020C	4	4	HR21	56346.187	-3.44	101.75	16.90
10090938-4121350	2020B	4	4	HR10	56343.190	9.68	47.54	17.13
10091241-4132476	2020A	4	4	HR10	56343.190	41.90	89.08	16.89
10092032-4138285	2020A	4	4	HR10 HR21	56343.190	-44.60	55.97	16.23
10092718-4128583	2020A	4	8	U580	56343.190	5.54	59.52	13.80
10224640-3541044	2020A	4	8	U580	56677.262	-14.88	28.50	13.60
10232266-3541019	2020A	4	8	U580	56679.316	22.99	55.67	13.70
10232300-3531571	2020C	4	4	HR21	56677.333	-33.71	41.65	14.40
10394014-4108011	2020A	4	4	HR10	56376.050	-32.14	16.59	15.70
10403618-4104492	2020A	4	4	HR10 HR21	56376.050	-56.89	58.35	16.00
11001645-4102232	2020C	5	5	HR10	55972.231	7.28	39.34	14.90
11010640-1322020	2020C	4	4	HR10	56343.284	1.09	33.20	18.60
11035508-1800428	2020B	4	4	HR10	56816.953	16.00	53.28	14.70
11230355-3455286	2020A	4	4	HR10	56798.975	-10.70	69.68	13.40
11265745-4100160	2020B	4	4	HR10	56376.096	-3.01	29.55	13.00
11315400-4359284	2020C	4	4	HR21	56378.058	-61.47	80.43	14.40
11593504-4050266	2020C	4	4	HR21	55998.260	-18.04	99.27	16.70
12000916-4101004	2020A	4	8	U580	55998.260	-47.51	18.99	12.30
12001709-3711459	2020A	4	4	HR10	56798.028	11.64	73.11	16.40
12005511-3711201	2020A	4	8	U580	56798.028	-0.76	41.61	13.80
12111883-4109109	2020A	4	4	HR10 HR21	56099.020	21.79	97.94	14.20
12113870-4103193	2020C	4	4	HR10	56099.020	-141.40	-3.08	14.30
12121230-4104498	2020C	4	4	HR10	56099.020	-6.21	33.32	16.80
12194390-3652280	2020A	4	4	HR10	56799.021	-17.48	37.19	16.50
12270079-4054566	2020C	4	4	HR21	56026.160	-11.18	70.95	14.80
12273877-4056402	2020C	4	8	U580	56026.160	-13.10	5.17	13.00
12431359-1304540	2020B	4	4	HR10	56075.090	80.54	117.97	16.50
12432209-4053149	2020A	4	4	HR10	56446.016	-43.16	3.42	14.70
12435905-0553086	2020A	4	4	HR10	56445.971	11.28	65.36	15.20
12562790-4516555	2020C	6	6	HR21	56468.068	-33.48	29.84	14.80
13201190-0859503	2020A	4	4	HR10 HR21	56444.062	-63.29	15.57	15.90
13203450-1302162	2020C	4	4	HR10	56444.108	18.37	50.90	14.30
13272650-4059266	2020A	4	4	HR10 HR21	56074.137	-52.36	45.90	14.40
13285153-4107423	2020A	4	4	HR10	56074.137	-122.48	-77.71	15.10
14001419-4054092	2020B	4	4	HR10	56002.306	-101.41	-61.30	15.70
14091400-3404548	2020A	4	4	HR10 HR21	56758.198	-12.18	98.40	15.70
14194570-1451154	2020C	4	4	HR21	56756.274	-55.20	28.19	16.50
14222902-4402086	2020A	4	8	U580	56469.067	-73.83	-39.67	13.00
14271982-0854407	2020B	4	4	HR10	56443.065	-54.04	-9.21	14.50
14402357-4009161	2020A	4	4	HR10 HR21	56471.007	-51.42	6.26	13.40
14591899-2001019	2020C	4	4	HR21	56754.372	-71.26	5.85	16.60
15001595-2001152	2020A	4	4	HR10	56754.264	-24.52	13.59	17.10
15003201-1456355	2020A	4	4	HR10 HR21	56755.236	-124.58	-53.53	15.60
15095102-1507425	2020A	4	4	HR10	56756.227	-91.84	-34.22	14.30

Table A.1. Continued.

CNAME	flag	# exp.	# sp.	setup	MJD	$v_r(1)$	$v_r(2)$	V
15095773-2000080	2020B	4	8	U580	56757.241	-26.65	3.27	13.40
15103048-1508193	2020A	4	4	HR10	56756.248	-6.32	40.67	14.50
15104140-1502572	2020A	4	4	HR10 HR21	56756.227	-110.74	-16.23	14.00
15104535-4054419	2020B	4	4	HR10	56445.093	-63.55	-12.87	14.70
15105813-4048090	2020A	4	4	HR10 HR21	56445.093	-55.76	58.10	13.70
15112349-4052387	2020A	4	4	HR10	56445.093	-131.32	-48.91	15.70
15122047-4054438	2020B	4	4	HR21	56446.197	-50.78	65.82	14.80
15161563-4125518	2020C	4	4	HR21	56444.196	2.50	67.81	15.00
15164593-4122457	2020C	4	4	HR21	56444.196	-81.86	-14.62	14.20
15291504-1953570	2020C	4	4	HR21	56817.237	20.76	83.47	16.80
15300257-4303505	2020C	4	4	HR21	56375.273	-59.09	12.07	12.70
15305329-1956301	2020C	4	4	HR21	56817.219	-82.63	24.67	14.20
15305481-4130573	2020B	2	2	HR21	56854.987	-96.73	92.52	13.30
15420717-4407146	2020A	4	4	HR10	56377.359	-17.37	78.24	14.80
15490519-1359089	2020A	4	4	HR10 HR21	56798.207	-39.28	67.37	15.30
15492053-0742483	2020A	4	4	HR10 HR21	56853.980	-16.69	66.03	14.40
15495562-0724391	2020C	4	4	HR21	56853.148	-172.12	-97.63	16.50
15502613-0740084	2020A	4	4	HR10	56854.001	-189.77	-132.55	15.40
15504227-1937508	2020C	4	4	HR21	56852.040	44.81	118.81	14.60
15545953-4106578	2020A	4	4	HR10	56024.218	-158.01	21.97	16.70
16035830-4547485	2020C	4	4	HR21	56377.316	-92.54	-6.58	14.50
17005619-0511542	2020C	4	4	HR21	56024.333	-63.21	7.58	14.70
17334015-4253407	2020A	7	7	HR10	56024.378	-11.27	72.68	15.40
17592273-4232176	2020C	4	4	HR21	56795.221	-21.63	55.54	17.40
18103653-4455176	2020B	4	8	U580	56798.409	12.57	34.07	13.10
18134362-4221083	2020C	6	6	HR21	56821.118	-102.95	-15.45	14.50
18135851-4226346	2020B	6	12	U580	56856.988	-33.65	-6.38	12.90
18162528-4239594	2020A	2	2	HR10	56821.258	-166.42	61.92	14.10
18180629-4457294	2020B	2	2	HR21	56853.175	-99.34	28.14	14.10
18201282-4708422	2020C	4	4	HR10	56446.173	-39.74	32.80	16.40
18203927-4655397	2020A	4	4	HR10 HR21	56446.151	-59.02	45.27	15.30
18402582-4709250	2020C	4	4	HR10	56498.087	-77.50	-54.20	17.00
18410111-4238337	2020A	4	4	HR10 HR21	56854.225	-132.94	96.51	14.20
18490733-3954253	2020A	4	4	HR10 HR21	56821.304	-52.98	11.59	14.10
18590483-4711187	2020C	2	2	HR21	56852.228	-3.62	78.82	16.50
18591414-4710472	2020C	2	2	HR21	56852.228	-126.16	-6.03	16.60
19000942-4231227	2020A	4	8	U580	56796.289	64.26	118.21	13.20
20183934-5400476	2020C	4	4	HR21	56795.348	-18.21	53.56	14.50
20192137-4706271	2020B	4	8	U580	56169.233	-40.37	-17.80	12.80
20194866-4651252	2020B	4	4	HR21	56173.176	-108.88	42.10	14.60
20593297-4655410	2020A	5	5	HR10 HR21	56819.391	-89.93	7.19	16.10
20594465-0044334	2020B	4	4	HR10	56855.317	-36.30	-3.47	15.00
21100126-0156012	2020A	2	2	HR10	56075.346	-15.57	57.46	15.90
21101784-0205349	2020A	4	8	U580	56075.346	-51.08	14.05	13.70
21201559-4807298	2020C	2	2	HR21	56170.281	-207.13	-126.88	17.10
21392385-5501257	2020A	4	4	HR10	56852.300	-113.35	-54.44	16.20
21402535-0055041	2020B	4	8	U580	56855.364	-35.24	-9.49	12.70
21523327-0321571	2020A	4	4	HR10 HR21	56101.381	-131.22	-18.06	12.70
21523611-0327136	2020A	4	4	HR10 HR21	56101.381	-54.42	27.90	16.10
21594936-4747133	2020A	7	7	HR10 HR21	56468.343	-80.96	24.33	14.80
21595211-4745562	2020C	7	7	HR21	56103.390	-58.88	9.37	15.70
22003339-4803527	2020A	7	7	HR10	56468.343	-40.29	80.29	12.90
22180319-5834560	2020C	4	4	HR21	56853.375	-71.53	15.23	14.60
22184292-5454411	2020C	4	4	HR21	56634.025	-66.04	18.99	15.10
22184686-5506505	2020A	4	4	HR10	56607.047	60.95	122.54	14.20
22291350-0507554	2020B	4	4	HR10	56502.314	-25.08	26.66	14.40
22293255-5016362	2020C	4	4	HR21	56635.034	-41.36	40.10	14.60
22494111-0506006	2020A	4	4	HR10	56548.228	-105.68	-26.75	15.80
22495134-5544411	2020B	4	4	HR10	56576.109	-11.74	32.94	14.10
22593725-0052333	2020A	4	8	U580	56501.304	-65.70	-26.62	13.90

Table A.1. Continued.

CNAME	flag	# exp.	# sp.	setup	MJD	$v_r(1)$	$v_r(2)$	V
23291894-5018404	2020A	4	4	HR10	56503.371	31.27	75.99	16.10
23303304-0504082	2020C	4	4	HR21	56225.047	-26.68	51.21	15.30
23354061-4305405	2020A	4	4	HR10	56857.312	69.50	112.65	15.30
23394097-0056031	2020C	4	4	HR21	56224.096	-32.62	28.29	15.90
23481930-5617480	2020B	4	4	HR10	56547.261	42.89	80.65	15.10
23501242-0503050	2020B	4	4	HR21	56267.025	-62.12	58.52	15.70
23501961-5012563	2020A	4	8	U580	56602.084	-70.46	70.20	12.20
23572607-4802051	2020C	4	4	HR21	56206.128	-27.59	46.31	15.30

Notes. The column ‘CNAME’ is the GES name (constructed from the J2000 coordinates), ‘flag’ is the final flag after eye inspection, ‘# exp.’ the number of exposures available for that star, ‘# sp.’ is the number of available spectra (larger than the number of exposures in the case of UVES data which provide two spectra per exposure), ‘setup’ is the spectrograph setup, ‘MJD’ is the modified Julian Date of the unique observation listed, $v_r(1)$ and $v_r(2)$ are the velocities of the two components in km s^{-1} . The last column gives the visual magnitude of the source.

Table A.2. List of SB3 candidates in the field ordered by right ascension.

CNAME	flag	# exp.	# sp.	setup	MJD	$v_r(1)$	$v_r(2)$	$v_r(3)$	V
08202324-1402560	2030A	4	4	HR10	56758.012	-14.05	42.53	100.73	14.20
12000646-4052156	2030A	4	8	U580	55998.324	-33.99	14.34	56.68	12.70
13593100-1003043	2030A	6	12	U580	55999.277	-16.50	11.43	52.05	12.60
15003096-2000179	2030A	4	8	U580	56754.264	-105.96	-71.31	-42.15	13.80
18170244-4227076	2030A	2	2	HR10	56821.258	-39.69	-1.83	32.40	14.30

Appendix B: SB2 candidates in selected fields**Table B.1.** List of SB2 candidates in selected fields^a ordered by right ascension.

CNAME	flag	# exp.	# sp.	setup	MJD	$v_r(1)$	$v_r(2)$	V
Bulge								
17542544-3750568	2020C	2	2	HR21	56819.206	-77.81	9.78	15.36
17571482-4147030	2020B	2	4	U580	56173.006	-11.07	30.13	11.57
17581333-3434348	2020B	3	3	HR21	56817.269	-32.77	54.95	15.46
18041571-3000506	2020A	2	2	HR21	55724.240	-51.90	145.50	16.31
18175005-3247501	2020C	2	2	HR21	56207.979	-17.67	75.84	15.10
18380149-2820437	2020B	2	2	HR21	56758.359	-128.80	-42.25	14.18
Cha I								
11085326-7519374	2020B	2	4	U580	56047.093	-33.15	51.72	12.17
11120384-7650542	2020B	2	2	HR15N	56025.156	11.90	60.79	14.16
CoRoT								
06435847-0100516	2020A	18	18	HR10 HR15N	55999.997	-40.34	54.97	13.05
19235724+0138241	2020A	6	6	HR10 HR15N HR21	56470.289	7.22	103.61	14.40
19243943+0048136	2020C	18	18	HR15N	56171.039	-52.08	65.68	15.11 ^b
19255064+0022240	2020C	6	6	HR15N	56756.414	-47.86	-1.75	12.69
19261871+0030211	2020A	6	6	HR10 HR21	56473.199	13.50	90.26	14.86
19262489+0137506	2020A	6	6	HR10	56816.215	-50.50	67.49	14.90
19263739+0152562	2020A	6	6	HR10	56473.166	-60.25	221.28	13.60
γ^2 Vel								
08072516-4712522	2020A	2	4	U580	55972.105	-25.30	20.17	11.43
08073722-4705053	2020C	2	4	U580	55929.251	54.85	83.85	11.83
08074628-4700347	2020B	2	2	HR15N	55929.251	-11.60	56.77	13.37
08082580-4716381	2020C	2	2	HR15N	55928.190	-0.20	61.00	16.21
08091392-4715498	2020C	2	2	HR15N	55928.146	15.65	107.03	16.93
08091937-4719385	2020C	2	2	HR15N	55972.080	-67.47	92.02	12.75
08093154-4724289	2020C	2	2	HR15N	55928.146	17.43	107.48	17.47
08093589-4718525	2020B	2	6	HR15N U580	55972.080	-4.47	40.48	12.79
08094221-4719527	2020C	2	6	HR15N	55972.080	-29.17	49.90	12.40
08094864-4702207	2020B	2	2	HR15N	55927.156	-4.09	52.59	16.52
08095076-4745311	2020C	2	2	HR15N	55972.155	-44.06	1.17	12.90
08095692-4717476	2020B	2	2	HR15N	55972.080	-33.39	48.57	13.35
08103996-4714428	2020B	2	8	HR15N U580	55972.056	-36.24	60.15	12.06
08111009-4718006	2020B	2	2	HR15N	55928.099	11.41	65.79	16.36
08115305-4654115	2020A	2	6	U580 HR15N	55927.111	0.52	53.30	12.93
08115892-4715140	2020B	2	2	HR15N	55928.099	-4.87	60.44	16.95
ρ Oph								
16244913-2447469	2020C	2	2	HR15N	56103.158	-10.40	47.36	15.68

Notes.

^(a) See text for references about target selection and membership assesment in those fields.

^(b) The visual magnitude of this star was wrongly assessed by CASU. The closest star resolved in Simbad is at a distance of 42.88 arcsec and corresponds to CoRoT 100791478.

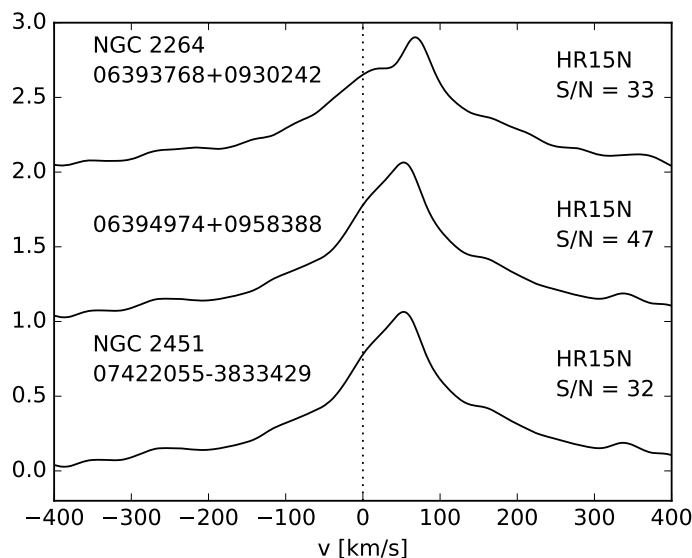


Fig. C.1. Two examples of stars in NGC 2264 and one in NGC 2451 flagged as SB2 by the DOE procedure but discarded from the final list.

Appendix C: SB2, SB3 and SB4 candidates in stellar clusters

IC 2391. This open cluster includes the unique SB4 candidate 08414659-5303449 in the current iDR4 GES data. At some epochs, the two weakest components are hardly visible, that is why we classified this source with both 2020A and 2040A flags (see Fig. 23). This SB4 candidate is analyzed in detail in Sect. 4.5.

IC 2602. All the three systems are consistent with cluster membership. System 10403116-6416249 seems to be a pair of rapidly rotating stars.

IC 4665. System 17452506+0540233 has a broad CCF with a secondary bump in its tail, but the velocities are not centred on the cluster velocity.

M67. All four SB2s are confirmed through visual inspection, having composite spectra and having membership confirmed.

NGC 2243. Only one clear SB2 candidate with a composite spectrum is retained. Two other candidates (06292559-3116070 and 06294409-3116276) are not retained, since the major peak of the CCF is at the cluster velocity, with a secondary bump offset by -60 km s^{-1} and -100 km s^{-1} , respectively.

NGC 2264. The DOE procedure has flagged a lot of stars as SB2 in this (and in all other) young clusters. Many of these stars have broad CCFs with a secondary bump, as illustrated in Fig. C.1. As the centre of this very broad CCF is close to the cluster velocity, these stars are thought to be both rapidly rotating and pulsating (δ Sco variables), and this combination is responsible for the peculiar and specific CCFs observed in young clusters, whose turn-off is located higher up on the main sequence to allow the presence of δ Sco stars. Not all of them are A stars though, and therefore we suggest the alternative hypothesis that this peculiar CCF profile is related to the disk still surrounding these young stars. In that case, the CCFs offer an interesting diagnostic to study/detect these disks (see Rebull et al. 2002). 06405650+0911389 (HD 261905) has its main peak at the cluster velocity, and a clearly defined, well-separated second peak at a velocity of 71.9 km s^{-1} . Although the field is not especially crowded, the DSS image¹⁰ reveals that the stellar image might be not perfectly round, and seems contaminated by a nearby source. 06421531+0942581 has a secondary peak close to the cluster velocity, but the main peak is totally offset (99 km s^{-1}). That peak might be due to a somewhat brighter star (NGC 2264 SBL 560) located about 4 arcsec west of the target (probably not a member, given its largely offset velocity).

NGC 2451. The situation for this cluster is quite special since there are in fact two different clusters, located at different distances, superimposed at the same location on the sky (Dias et al. 2002). These authors report a velocity of $+22.7 \text{ km s}^{-1}$ for the nearest NGC 2451A cluster and 14.0 km s^{-1} for the farthest NGC 2451B cluster. 07401559-3735416, a genuine SB2 system, cannot be a member of NGC 2451. On JD 2456634, the CCF exhibits peaks at 21 and 62 km s^{-1} , while at JD 2456638 and JD 2456677, the peaks are located around -2 and 85 km s^{-1} , implying a centre-of-mass velocity of the order of 40 km s^{-1} , significantly offset with respect to the velocities of NGC 2451A and NGC 2451B. 07422055-3833429 bears similarities with the cases discussed in relation with NGC 2264, namely a very broad CCF (base width of about 400 km s^{-1}), a main peak at 105 km s^{-1} , well offset with respect to the cluster velocity, and another bump at 20 km s^{-1} , close to the cluster velocity. The spectrum seems to show H α emission. This star has been discarded from the final list.

NGC 2516. 07593671-6021483 is probably a genuine SB2, with the peaks (22 and 50 km s^{-1}) centred on the cluster velocity (23.6 km s^{-1}). 07594121-6109251 has a broad (base width 100 km s^{-1}) CCF, with two bumps (-23 and -5 km s^{-1}) not centred on the cluster velocity and is maybe contaminated by nebular absorption lines.

NGC 2547. 08081564-4908244 is a genuine SB2, but probably not a member of NGC 2547, since the component velocities (52 and

¹⁰ <http://archive.stsci.edu/dss>

122 km s⁻¹) do not encompass the cluster velocity (15.7 km s⁻¹).

NGC 3293. 10361099-5814310 classified as 2020C is probably a δ Scu star (the recommended parameters are $T_{\text{eff}} = 8985$ K, $\log g = 4.01$) and shows emission in H α . Rather than SB2 systems, 10353288-5813498 and 10353397-5813178 are rapidly rotating (and probably pulsating) stars (because their CCFs are distorted). They are pre-main sequence star candidates (Delgado et al. 2007).

NGC 3532. The source 11085927-5849560 is identified for the first time as an SB2 candidate.

NGC 6005. Three SB2 candidates have only been observed with the HR9B setup (around the Mg I b triplet) where it is difficult to assess if the spectra are composite or not. 15555518-5725349 shows a broad CCF due to H α in HR15N with a main peak at -69 km s⁻¹, and a bump at -27 km s⁻¹, close to the cluster velocity.

NGC 6530. Numerous spurious detections of SB candidates are due to the presence of nebular lines in emission in HR15. Also, there are thin and deep absorption lines around 6678, 6715 and 6730 Å. Nebular lines are present around 6717 and 6730 Å in HR15 and have led to some reduction issues since negative fluxes are observed at these wavelengths in some stars (18044420-2415380, 18045889-2415261, 18043887-2427164). Their associated CCFs are then not reliable and have been discarded from the final list. There is strong and deep H α absorption in several stars. Surprisingly, many discarded SB2 components have velocities close to -60 km s⁻¹. This raises the question of the presence of another possible velocity component for that cluster.

NGC 6633. 18280622+0642252 (NGC 6633 110, $V = 10.1$, A3) is an interesting case of a fast rotator which could be a δ Scu-type star according to the iDR4 recommended parameters ($T_{\text{eff}} = 9600$ K, $\log g = 4.80$ and solar metallicity). Only the upper grating of U580 is available showing very thin and deep absorption lines superimposed on the less deep and rotationally broadened Na I D doublet probably caused by nebular line contamination.

NGC 6705. The composite spectra and the associated CCFs of one of the five SB2 A candidates are presented in Fig. 16. This is an illustration of a very favorable case because 18503230-0617112 (NGC 6705 1936) has been observed in eight setups and shows a two-component CCF in all of them. 18511434-0617090 has four observations with the HR15N (H α) setup. In all cases, the main peak is around 33 km s⁻¹, close thus to the cluster velocity, whereas the CCF exhibits a secondary bump around -50 km s⁻¹. But the contrast of that bump is variable, suggesting that its origin may be related to stellar variability (but $B - V \sim 1$, suggesting that the star is a red giant, and H α variability is not expected; Cantat-Gaudin et al. 2014). On the contrary, if the system were an SB2, its kinematics is not compatible with membership in the cluster.

NGC 6752. 19105940-5957059 is the star A13 in Moni Bidin et al. (2006) which has not been detected as binary. The CCFs show clearly the presence of two peaks (flagged 2020 B). 23 observations covering more than 1500 days are available, but we unsuccessfully tried to fit an orbit. Indeed the radial velocities of the components stay constant within few km s⁻¹. Moreover the star is located in a very dense region of this globular cluster and we conclude that this is an “optical” SB2.

NGC 6802. Two SB2 and one SB3 candidates have been found in this cluster.

Trumpler 14. A large number of false SB2 detections were identified due to the presence of very strong nebular lines and reduction issues in HR15N where spectra have H α with negative flux and core emission (see Sect. 4.7 and figures within for discussion). Nebular emission in Trumpler 14 and more generally in the Carina nebula is investigated in details by Damiani et al. (2016).

Trumpler 20. 12384378-6037077 has one component located at the cluster velocity. The unique CCF of 12393764-6038190 could either be indicative of a rapidly rotating star, with some asymmetries in the line profile or of a cluster member (-36 km s⁻¹) blended with a non-member (-77 km s⁻¹). The same remark holds true for 12393362-6041446. The secondary peak of 12391767-6036083 is probably from a non-member. The main peak in the CCF of 12391992-6029552 at -3.4 km s⁻¹ is probably from a non-member.

Trumpler 23. The radial velocity of this cluster has just been assessed to -61.3 ± 1.9 km s⁻¹ within the GES consortium (Overbeek et al., submitted). Therefore the SB2 candidate 16004521-5332044 may be considered as a member of this cluster.

Table C.1. SB2, SB3 and SB4 candidates in clusters ordered by increasing identifier. The column ‘CNAME’ is the GES name (constructed from the J2000 coordinates), ‘flag’ is the final flag after eye inspection, ‘# exp.’ the number of exposures available for that star, ‘# sp.’ is the number of available spectra (larger than the number of exposures in the case of UVES data which provide two spectra per exposure), ‘setup’ is the spectrograph setup, ‘MJD’ is the modified Julian Date of the unique observation listed, v_r is the cluster velocity, $v_r(1)$ and $v_r(2)$ are the velocities of the two components. The ‘Member’ column states whether the SB candidate belongs to the cluster or not (see Sect. 4.2). The last column ‘Remark’ contains additional information after detailed inspection of their spectra and CCFs: CS: composite spectrum, 1RRC/2RRC: one or two rapidly-rotating component(s), PULS: pulsating star, δ Scu: probable δ Scu type star, H α e: H α with emission, NaDe: Na I D with emission, NLC: nebular line contamination, ILC: interstellar line contamination, XR: X-ray source, ORB: orbit calculated, ST: see text for additional information. The “?” character is indicative of some uncertainty in the preceding characterisation.

Cluster CNAME	log age flag	# exp.	# sp.	setup	MJD	v_r (km s ⁻¹)		SB2/3/4	Member	Remark
						$v_r(1)$ (km s ⁻¹)	$v_r(2)$ (km s ⁻¹)			
IC 2391	7.74					14.49 ± 0.14				
08385566-5257516	2020B	4	8	U580	56705.032	-14.84	44.91	SB2	y	CS
08393881-5310071	2020A	6	12	U580	56705.032	-23.25	39.12	SB2	y	CS, 1RRC
08414659-5303449	2020A	45	90	U520	56707.028	-21.64	50.75	SB2	y	CS
08414659-5303449	2040A	45	90	U520 U580	56707.028	-21.64	50.75	SB4	y	CS, ST
IC 2602	7.48					18.12 ± 0.30				
10403116-6416249	2020C	1	1	HR15N	53827.129	-67.55	98.63	SB2	y	CS
10450829-6422416	2020A	1	1	HR15N	53839.031	-69.80	66.01	SB2	y	CS
10460575-6420184	2020B	2	4	U580	56711.229	-18.14	22.87	SB2	y	CS, 1RRC
IC 4665	7.60					-15.95 ± 1.13				
17450496+0541287	2020A	6	6	HR15N	56469.201	-109.77	46.17	SB2	y	CS, H α e
17452506+0540233	2020C	2	2	HR15N	56471.099	7.72	87.39	SB2	n	CS?
17453692+0542424	2020A	2	4	U580	56471.099	-49.75	18.17	SB2	y	CS
17455717+0601224	2020B	2	2	HR15N	56471.233	-43.74	53.34	SB2	y	CS
17472992+0607069	2020B	2	2	HR15N	56473.072	-64.42	8.52	SB2	y	CS
M 67	9.60					33.8 ± 0.5				
08511868+1147026	2020A	3	6	U580I	54866.304	-12.47	88.80	SB2	y	CS, XR
08511901+1150056	2020A	4	8	U580I	54866.221	-28.00	97.99	SB2	y	CS
08512291+1148493	2020A	4	8	U580I	54866.221	15.78	53.47	SB2	y	CS
08512940+1154139	2020A	5	10	U580I	54853.182	15.99	49.90	SB2	y	CS
NGC 2243	9.60					59.5 ± 0.8				
06290412-3114343	2020B	4	4	HR15N	56603.226	19.78	118.51	SB2	y	CS
NGC 2264	6.48					24.69 ± 0.98				
06404608+0949173	2020A	22	24	HR15N U580	55915.177	-88.21	102.35	SB2	y	CS, 2RRC, ORB, XR, ST
06413150+0954548	2020B	22	24	HR15N U580	55915.177	-24.07	58.82	SB2	y	CS, NLC?
06413207+1001049	2020B	4	6	U580	56267.205	77.74	133.75	SB2	n	CS, 1RRC
06414775+0952023	2020A	8	10	HR15N U580	56268.205	-52.95	84.71	SB2	y	CS, NaDe
NGC 2451	7.8 (A) 8.9 (B)					22.70 (A) 14.00 (B)				
07371334-3831467	2020B	4	4	HR15N	56634.212	-16.05	46.59	SB2	y	CS
07382664-3839208	2020B	4	4	HR15N	56634.212	0.71	57.57	SB2	y	
07384076-3743189	2020C	4	4	HR15N	56677.217	-6.51	61.72	SB2?	y	
07401559-3735416	2020A	6	12	U580	56634.259	21.18	61.77	SB2	n	CS, ST
07405697-3721458	2020A	2	4	U580I	56677.309	101.60	146.85	SB2	n	CS
07413421-3719442	2020C	2	2	HR15N	56635.182	49.04	118.40	SB2?	n	
07431451-3810155	2020B	2	2	HR15N	56635.226	-11.94	47.02	SB2	y	
07454636-3809168	2020C	2	2	HR15N	56679.221	-34.99	46.81	SB2	y	
07455390-3812406	2020B	4	8	U580	56637.222	-2.21	31.73	SB2	y	CS
07455995-3854469	2020B	2	2	HR15N	56679.290	-23.86	68.51	SB2	y	CS
07463487-3905202	2020A	2	2	HR15N	56679.290	-10.76	75.22	SB2	y	CS
07470917-3859003	2030A	2	4	U580	56637.287	25.04	96.07, 136.62	SB3	y	CS

Table C.1. Continued.

Cluster CNAME	log age flag	# exp.	# sp.	set-up	MJD	v_r (km s ⁻¹)		SB2/3/4	Member	Remark
						$v_r(1)$ (km s ⁻¹)	$v_r(2)$ (km s ⁻¹)			
NGC 2516	8.20					23.6 ± 1.0				
07540665-6043081	2020A	2	2	HR15N	56342.032	-40.52	63.01	SB2	y	CS, Hae
07551150-6028375	2020C	2	2	HR15N	56374.017	-4.99	54.22	SB2	y	CS
07563381-6046027	2020B	2	2	HR15N	56375.037	-3.54	50.50	SB2	y	CS
07575737-6044162	2030C	2	4	U520	56375.037	-30.40	30.90, 77.79	SB3	y	ST
07593411-6042583	2020B	4	4	HR15N	56375.037	-39.31	61.19	SB2	y	CS
07593671-6021483	2020B	2	4	U580	56376.004	21.84	49.71	SB2	y	CS
07594121-6109251	2020C	3	4	U580	56374.128	-23.26	-5.11	SB2	n	CS?, NLC?
07594744-6049228	2020B	4	4	HR15N	56375.011	-1.23	48.64	SB2	y	CS
07595659-6049283	2020C	2	2	HR15N	56375.078	-9.56	49.97	SB2	y	CS
NGC 2547	7.54					15.65 ± 1.26				
08081564-4908244	2020A	4	6	U580 HR15N	56310.201	51.01	119.87	SB2	n	CS, ST
NGC 3293	7.00					-12.00 ± 4.00				
10343408-5814431	2020A	12	12	HR3 HR5A HR9B HR14A	55972.322	-9.65	51.10	SB2	n	CS?, Hae
10345341-5812222	2020C	12	12	HR9B	56024.110	-21.54	39.34	SB2	y	Hae?
10350728-5810574	2020B	9	9	HR6	56024.034	-18.58	151.33	SB2	y	2RRC?
10361099-5814310	2020C	9	9	HR6 HR14A	56000.121	-78.31	41.59	SB2?	y	δ Scu? Hae ST
10361385-5819052	2020B	12	12	HR5A HR14A	55972.322	-70.47	34.69	SB2	y	CS?, 1RRC
10361494-5814170	2020B	7	7	HR6 HR14A	55999.147	-54.32	20.01	SB2	y	Hae
10361791-5814296	2020C	12	12	HR14A	55972.322	-46.06	57.26	SB2	y	
10362294-5825333	2020B	7	7	HR3	55998.113	-40.41	39.06	SB2	y	CS?
10362842-5805112	2020B	7	7	HR3 HR5A HR6	55998.218	-40.13	29.55	SB2	y	CS
NGC 3532	8.48					-4.8 ± 1.4				
11085927-5849560	2020B	9	18	U580	56440.953	-11.12	28.73	SB2	y	CS
NGC 4815	8.75					-29.4 ± 4				
12573865-6454061	2020B	12	12	HR9B	56025.203	-103.71	37.33	SB2	y	noisy
12572682-6456300	2020C	10	10	HR15N	56028.203	-89.49	-2.06	SB2	y	Hae?
NGC 6005	9.08					-24.1 ± 1.3				
15553867-5724434	2030B	4	4	HR9B	56795.265	-81.6	-14.4, 32.7	SB3?	y?	noisy, ST
15554550-5728087	2020B	4	4	HR9B	56795.265	-63.56	3.69	SB2	y	CS?
15554669-5725386	2020A	2	2	HR9B	56794.295	-50.27	0.40	SB2	y	CS?
15555518-5725349	2020C	6	6	HR15N	56816.147	-68.85	-26.73	SB2?	n?	noisy, ST
15561896-5725399	2020A	2	2	HR9B	56794.295	-104.43	-28.40	SB2	n	CS?
NGC 6530	6.30					-4.21 ± 6.35				
18040734-2422217	2020C	1	1	HR15	52787.320	-40.09	5.40	SB2	y	
18040988-2425323	2020A	1	1	HR15	52787.390	-62.76	50.74	SB2	y	CS, NLC
18045495-2423096	2020C	3	3	HR15	52787.390	-61.28	0.50	SB2?	y?	
18045528-2412512	2020A	2	2	HR15N	56173.078	-105.52	6.67	SB2	y	CS
18052912-2428104	2020C	2	2	HR15N	56502.262	-14.13	56.55	SB2	n	Hae
NGC6633	8.78					-28.8 ± 1.5				
18263193+0637329	2020B	2	2	HR15N	56444.288	-72.17	78.21	SB2	y	Hae
18263896+0630410	2020B	2	2	HR15N	56445.184	-74.59	-1.45	SB2	y	NLC?
18264081+0632435	2020B	2	2	HR15N	56445.184	4.85	58.63	SB2	n	CS
18265864+0640458	2020B	2	2	HR15N	56444.288	-89.10	-0.78	SB2	y	CS
18270724+0638394	2020A	2	2	HR15N	56445.184	-49.28	42.61	SB2	y	CS
18271075+0627061	2020C	4	4	HR15N	56442.297	2.20	58.00	SB2	n	
18272122+0637268	2020A	5	5	HR9B HR15N	56444.273	-45.42	59.67	SB2	y	CS
18272783+0644321	2020C	2	2	HR15N	56444.309	-34.67	37.55	SB2	y	CS
18274341+0641115	2020C	5	5	HR9B	54279.258	-80.28	-31.25	SB2	n	
18280622+0642252	2020A	2	4	U520u	56444.342	-55.62	39.20	SB2	y	1RRC, PULS, ILC
18280970+0638061	2020B	3	3	HR15N	56444.333	-66.95	28.70	SB2	y	CS
18281038+0647407	2020B	2	4	U580	56854.131	-38.61	-13.44	SB2	y	CS
18282150+0645278	2020C	2	2	HR15N	56446.241	-8.46	103.81	SB2	n	Hae?
18282354+0646402	2020B	3	3	HR15N	56444.333	-104.96	30.15	SB2	y	CS
18283303+0645562	2020C	4	6	U520	56444.333	-7.29	10.97	SB2	n	CS, ILC

Table C.1. Continued.

Cluster CNAME	log age flag	# exp.	# sp.	set-up	MJD	v_r (km s ⁻¹)		SB2/3/4	Member	Remark
						$v_r(1)$ (km s ⁻¹)	$v_r(2)$ (km s ⁻¹)			
NGC 6705	8.47					34.9 ± 1.6				
18503230-0617112	2020A	12	12	HR6 HR9B HR10 HR21	56103.110	-38.24	117.09	SB2	y	CS
18503690-0621100	2020C	2	2	HR15N	56102.120	-29.51	83.84	SB2	y	CS
18503840-0617048	2020C	7	7	HR10 HR15N HR21	56443.382	-18.97	85.47	SB2	y	CS
18504649-0611443	2020C	2	2	HR15N	56101.333	-42.77	37.24	SB2	y?	CS
18505726-0609408	2020C	2	2	HR15N	56102.120	-14.52	104.31	SB2	y	
18505561-0614552	2020B	2	2	HR15N	56101.243	-10.39	80.95	SB2	y	CS
18505933-0622051	2020C	4	4	HR15N	56077.363	-2.32	144.85	SB2	y	H α e?
18510072-0609118	2020C	2	2	HR15N	56101.333	-12.01	60.80	SB2	y	CS
18510223-0614547	2020A	10	10	HR3 HR6 HR9B HR10 HR14A	56099.365	-8.13	69.14	SB2	y	CS, 1RRC
18510286-0615250	2020A	12	12	HR3 HR6 HR9B HR10 HR21	56442.400	-19.65	71.55	SB2	y	CS
18510286-0615250	2030A	12	12	HR3 HR6 HR9B HR10 HR21	56099.311	-44.37	40.28, 93.39	SB3	y	CS, ST
18510401-0615387	2020C	2	2	HR15N	56075.275	-7.77	62.68	SB2	y	noisy
18510405-0617156	2020C	2	2	HR15N	56075.255	-59.09	42.95	SB2	y	H α e?
18510456-0617121	2020A	12	12	HR3 HR6 HR9B HR10 HR14A HR15N HR21	56103.110	-7.76	81.62	SB2	y	CS
18510462-0616124	2020B	10	10	HR3 HR6 HR9B HR14A	56099.365	-3.64	91.28	SB2	y	
18511134-0616106	2020A	12	12	HR3 HR6 HR9B HR10 HR14A HR21	56103.110	2.11	71.07	SB2	y	CS
18511220-0617467	2020B	2	2	HR15N	56101.288	-3.56	78.60	SB2	y	CS
18511434-0617090	2020C	4	4	HR15N	56075.300	-51.22	33.12	?	y	H α e?, ST
18512166-0624074	2020C	4	4	HR15N	56075.300	7.39	53.69	SB2	y	
18513193-0612518	2020C	2	2	HR15N	56077.363	-2.33	96.69	SB2	y	H α e?
NGC 6752	10.13					-24.5 ± 1.9				
19105940-5957059	2020B	54	108	U580	54624.335	-39.76	-18.25	SB2	y	
NGC 6802	8.95					11.9 ± 0.9				
19302315+2013406	2030C	4	4	HR9B	56794.388	-22.35	22.04, 65.53	SB3	y	
19303540+2016178	2020A	4	4	HR9B	56794.388	-10.52	34.61	SB2	y	CS
19304355+2016530	2020A	6	6	HR9B	56797.303	-60.71	86.93	SB2	y	
Trumpler 14	6.67					-15.0				
10434299-5953132	2020B	15	15	HR6	56445.026	-118.89	113.84	SB2	y	
10442462-5930359	2020A	19	19	HR5A HR6 HR14A	56442.090	-139.47	94.25	SB2	y	CS, 1RRC, H α e
10443037-5937267	2020A	19	19	HR6 HR14A	56442.094	-126.45	161.46	SB2	y	CS, 2RRC, H α e
Trumpler 20	9.20					-40.2 ± 1.3				
12382369-6041067	2020C	1	1	HR9B	54962.018	-58.36	-8.07	SB2	y	noisy
12382945-6036007	2020A	1	1	HR9B	54960.122	-72.68	13.06	SB2	y	
12383365-6031092	2020B	1	1	HR9B	54929.059	-53.14	36.44	SB2	y	CS?
12384378-6037077	2020B	1	1	HR9B	54959.979	-40.24	24.74	SB2	n	CS
12384744-6036400	2020B	1	1	HR9B	54960.028	-43.73	9.52	SB2	n	
12385726-6038597	2020C	1	1	HR9B	54960.075	-63.54	-4.50	SB2?	y	
12390677-6042208	2020B	1	1	HR9B	54959.979	-21.45	19.41	SB2	n	
12390898-6037473	2020B	7	7	HR9B HR15N	56002.184	-124.91	41.80	SB2	y	CS?
12391247-6037429	2020C	1	1	HR9B	54962.068	-67.29	-3.30	SB2	y	
12391904-6035311	2020B	1	1	HR9B	54960.075	-85.78	14.83	SB2	y	
12391904-6035311	2030C	1	1	HR9B	54960.075	-85.78	-44.40, 14.83	SB3	y	
12393449-6039575	2020B	1	1	HR9B	54962.068	-60.30	-7.33	SB2	y	
12393764-6038190	2020C	1	1	HR9B	54960.075	-77.26	-36.00	SB2	y	1RRC?, ST
12391767-6036083	2020C	1	1	HR9B	54962.068	-42.12	-4.61	SB2	y	ST
12391992-6029552	2020C	1	1	HR9B	54962.068	-49.20	-3.38	SB2	y	ST
12394909-6040513	2020A	7	7	HR9B HR15N	56002.184	-69.73	-12.26	SB2	y	
12401228-6034325	2020C	12	12	HR15N	56377.231	-65.37	-2.61	SB2	y	
12402686-6036013	2020C	1	1	HR9B	54962.018	-67.57	-11.38	SB2	y	
12403561-6044331	2020C	1	1	HR9B	54962.018	-60.11	-26.56	SB2	y	noisy
12404299-6046290	2020A	1	1	HR9B	54929.107	-119.68	17.91	SB2	y	CS?

Table C.1. Continued.

Cluster CNAME	log age flag	# exp.	# sp.	set-up	MJD	v_r (km s ⁻¹)		SB2/3/4	Member	Remark
						$v_r(1)$ (km s ⁻¹)	$v_r(2)$ (km s ⁻¹)			
Trumpler 23	8.90					-61.3 ± 1.9				
16004521-5332044	2020A	4	4	HR9B	56551.985	-137.87	26.29	SB2	y	2RRC
Berkeley 25	9.70					134.3 ± 0.2				
06413639-1628236	2020B	20	20	HR9B	56576.317	-6.62	27.00	SB2	n	noisy
06414138-1624323	2020B	20	20	HR9B	56576.297	-10.52	28.45	SB2	n	noisy
Berkeley 81	8.93					48.3 ± 0.6				
19013140-0028066	2020C	8	8	HR15N	56170.005	-11.28	76.17	SB2?	y	
19013257-0027338	2020A	24	24	HR9B HR15N	56170.005	-18.49	118.26	SB2	y	ORB